

https://dspace.org/

Search and analysis techniques for extended sources in deep radio surveys

Thwala, Siphiwe Anthony

2018

https://hdl.handle.net/10539/27304

Thwala, Siphiwe Anthony (2018) Search and analysis techniques for extended sources in deep radio surveys, University of the Witwatersrand, Johannesburg, https://hdl.handle.net/10539/27304

Downloaded from a DSpace repository. https://dspace.org/

Search and analysis techniques for extended sources in deep radio surveys

by

Siphiwe Anthony Thwala

A dissertation submitted in fulfilment of the requirements
for the degree of Master of Science

in the

School of Physics
Faculty of Science
University of the Witwatersrand

August 2018

Declaration

I declare that this dissertation is my own, unaided work. It is being submitted for the Degree of Master of Science at the University of the Witwatersrand, Johannesburg. It has not been submitted before for any degree or examination at any other University.

Signed : 

Date : 06 August 2018

"If you want to go fast, go alone. If you want to go far, go together."

—African Proverb

Abstract

We produced a search for extended radio sources in the LOFAR Two Meter Survey HETDEX Spring Field, and we were able to identify 17 low-brightness sources in a region of $9.5^\circ \times 8.7^\circ$, an area of the sky between RA: $10^{\rm h}37^{\rm m}00^{\rm s}$ to $11^{\rm h}48^{\rm m}00^{\rm s}$ and DEC: $44^\circ19'00''$ to $52^\circ55'00''$. We focus in this study on the poorly studied radio galaxy PGC2285791 presenting a detailed analysis of its core, of the two extended radio lobes, a spectral index map between 141 and 1400 MHz and its multi-frequency association with an IR and optical counterparts. Our results led to the identification of this source with a $z = 0.14$ extended (~ 6 arcmin in the S-N direction) radio galaxy with bubble-like radio lobe structures and a morphological similarity in the extended radio structure of PGC2285791 with the remnant radio galaxy B20924+30, except PGC2285791 has a prominent radio core. Future X-ray and millimeter observations will greatly help in understanding the energetics of the radio lobes by measuring the associated inverse Compton scattering on CMB photon emission.

Acknowledgements

First and foremost, I would like to express my sincere gratitude to my supervisor Professor Sergio Colafrancesco. Thank you for your patience and mentorship. You have been the necessary scientific and logical framework that has provided reasoning to the chaotic meandering exploration I am constantly immersed in.

I would like to extended my deepest gratitude to Doctor Nebiha Shafi for the numerous discussions (which sounded like fights at times) that often led to critical breakthroughs. I greatly appreciate the effort you have put into this project and the paper.

I would also like to acknowledge my peers (widely known as ninjas) in the Astrophysics group at Wits, you all make the madness look normal and cool. A particular shout out to Charles and Nthabiseng for always being dodge in this journey. I would also like to extend my appreciation to Professor John Carter for his ever ready advice and guidance.

To the two giants I will forever be indebted, Busisiwe and Nomgqibelo Thwala, you are my pillars and I will always be thankful for the life lessons you have consistently shared with me. Niyohlala niyinjabulo engapheli nothando engiyohlale ngilizwa njalo.

I acknowledge the funding support of the South African Square Kilometre Array Initiative through their post-graduate bursary programme. The conclusions reached here do not necessarily represent the positions of the SKA SA.

Finally I would also like to expand my deepest gratitude to all of my friends, family and supporters.

"A family is like a forest, when you are outside it is dense, when you are inside you see that each tree has its place."

— African Proverb

Contents

Declaration i

Abstract iii

Acknowledgements iv

List of Figures vii

List of Tables xv

Abbreviations xvi

1 Introduction 1
- 1.1 Radio galaxies . . . 3
- 1.2 Spectral line emission . . . 4
- 1.3 Continuum emission . . . 5
  - 1.3.1 Thermal emission processes . . . 6
  - 1.3.2 Non-thermal emission processes . . . 7
- 1.4 Motivation for this work . . . 9

2 Description of data 11
- 2.1 LOFAR Two-metre Sky Survey . . . 12
- 2.2 NRAO VLA Sky Survey . . . 13
- 2.3 TIFR GMRT Sky Survey . . . 13
- 2.4 Very Large Array Low-frequency Sky Survey . . . 14

3 Data analysis techniques 15
- 3.1 Preparation and pre-analysis of Data . . . 16
- 3.2 Data exploration procedure . . . 22
- 3.3 Data analysis . . . 26

4 Extended sources 37
- 4.1 Source PGC2285791 . . . 37
  - 4.1.1 Morphology . . . 38
  - 4.1.2 Integrated spectra . . . 39

4.1.3 Multi-ν analysis 41
4.1.4 Spectral index map 44
4.1.5 Discussion 45
4.2 Other sources 46

5 Conclusions **65**

Bibliography **66**

List of Figures

1.1 An illustration of the large variance in frequency and wavelengths found in the electromagnetic spectrum, along with intuitive scales of the different wavelengths, the temperature in these bands and the possibility of observing these signal from Earth's surface [33]. 1
1.2 An illustration of the different telescopes used as probes in astrophysics and the "windows" (wavelength regions of the electromagnetic spectrum) we can probe from the surface of Earth [37]. 2
1.3 A side by side view of the two radio morphology classes devised by Fanaroff & Riley based on the large-scale radio emission of extragalactic radio sources. 4
1.4 An example of observed recombination-line spectra from the 91α and 92α transitions of hydrogen, helium, and carbon observed in an H_{II} region [60]. 5
1.5 A plot of the flux against wavelength of a blackbody emitter, showing that such an object will emit a spectrum of radiation which peaks at a wavelength (or frequency) dependent only on the objects temperature. As the source temperature increases the peak wavelength decreases. This is why hot stars appear blue and cool stars appear red [71]. 6
1.6 A simple illustration of a relativistic electron being accelerated by a magnetic field and the synchrotron radiation that is emitted as the charged particle gets boosted by the magnetic field [11]. This is the source of the diffuse emission we wish to study from the extended radio sources we looked at in this study. 7
1.7 A log-log scale plot of a composite spectrum for a typical galaxy observed over a wide range of frequencies, from radio to visible [71]. 8
1.8 The radio and far-infrared spectrum of the nearby starburst galaxy M82 [18]. The contribution of free-free emission is indicated by the nearly horizontal dashed line. Synchrotron radiation (dot-dash line) and thermal dust emission (dots) dominate at low and high frequencies, respectively. Free-free absorption from H_{II} regions distributed throughout the galaxy absorbs some of the synchrotron radiation and flattens the overall spectrum at the lowest frequencies [59]. 9

3.1 Source profile plots showing two possible source profiles. We display the red line to highlight the possible downside of using thresholds on sources with non-Gaussian profiles. The pixel masking and conversion procedure provides estimates to excluded sources since it simply cuts off pixel intensities and does not perform flux integration over the area above the threshold. This requires some human intervention to double check the excluded sources making it a less rigorous approach than using the dynamic flux per beam area procedure. 17

3.2 The LoTSS 141 MHz continuum image of PGC2285791 overlaid with black LoTSS contours starting at 3σ (σ = 0.58 mJy/beam) with 2σ increments. The purple regions highlight the different regions used in calculating the integrated spectra, for the northern and southern lobes and the two hotspots in the northern lobe. The beam size of the LoTSS is shown in the lower left corner. 21
3.3 First row: the LoTSS 141 MHz continuum image of IC 711, shown without contours on the left and overlaid with black LoTSS contours on the right, starting at at 3σ (σ = 1.31 mJy/beam) with 2σ increments and ending at 14.41 mJy/beam. Second row: same images as the First row, with a mask applied to IC 711 at the 160 mJy/pixel intensity threshold to remove "bright" radio point sources and highlight the obscured diffuse emission we analyse in this study. Third row: same images as the First row, with a mask applied to IC 711 at the 80 mJy/pixel intensity threshold for the same purpose mentioned in the Second row. 24
3.4 First row: The LoTSS 141 MHz continuum image of source 13, shown without contours on the left and overlaid with black LoTSS contours on the right, starting at 3σ (σ = 0.81 mJy/beam) with 2σ increments and ending at 15.39 mJy/beam. Second row: same images as the First row, with a mask applied to source 13 at the 160 mJy/pixel intensity threshold to remove "bright" radio point sources and highlight the obscured diffuse emission we analyse in this study. Third row: same images as the First row, with a mask applied to source 13 at the 80 mJy/pixel intensity threshold for the same purpose mentioned in the Second row. 25
3.5 (Left) The LoTSS continuum image of PGC2285791 showing how the value we specified for the LoTSS beam (purple circle) in CASA matches with the default LoTSS beam (white circle). (Right) The same image with the LoTSS beam now placed over the area we integrated the flux density over (purple beam now centred at RA: 11h 04m 33.126s, DEC: $46°42'24.793''$). 26
3.6 The spectrum of the core of the radio galaxy PGC2285791 is shown for different frequencies, with the frequency-flux (MHz, mJy) pairs of: (73.79, 19.76), (141.45, 7.34), (147.50, 7.47) and (1400.00, 1.04), integrated over the LoTSS beam size. 34
3.7 The spectrum of the core of the radio galaxy PGC2285791 is shown for different frequencies, with the frequency-flux (MHz, mJy) pairs of: (73.79, 59.72), (141.45, 17.35), (147.50, 22.59) and (1400.00, 2.90), integrated over the NVSS beam size. 34
3.8 The spectrum of the core of the radio galaxy PGC2285791 is shown for different frequencies, with the frequency-flux (MHz, mJy) pairs of: (73.79, 166.15), (141.45, 36.63), (147.50, 62.84) and (1400.00, 6.54), integrated over the VLSSr beam size. 34
3.9 The SED of the core of the radio galaxy PGC2285791 with previously known optical (blue), infrared (green) and radio (red) data points plotted with the addition of the VLSSr (magenta), LoTSS (black), TGSS (grey overlaps with black) and NVSS (navy) data points, integrated over the LoTSS beam size. 35

3.10 The SED of the core of the radio galaxy PGC2285791 with previously known optical (blue), infrared (green) and radio (red) data points plotted with the addition of the VLSSr (magenta), LoTSS (black), TGSS (grey) and NVSS (navy) data points, integrated over the TGSS beam size. . . . 35
3.11 The SED of the core of the radio galaxy PGC2285791 with previously known optical (blue), infrared (green) and radio (red) data points plotted with the addition of the VLSSr (magenta), LoTSS (black), TGSS (grey) and NVSS (navy) data points, integrated over the VLSSr beam size. . . 35

4.1 The LoTSS 141 MHz continuum image of PGC2285791 overlaid with black LoTSS contours starting at 3σ ($\sigma = 0.58$ mJy/beam) with 2σ increments. The purple regions highlight the different regions used in calculating the integrated spectra, for the northern and southern lobes and the two hotspots in the northern lobe. The beam size of the LoTSS is shown in the lower left corner. 38
4.2 The NVSS continuum image of PGC2285791 overlaid with black NVSS contours starting at 3σ ($\sigma = 0.57$ mJy/beam) with 2σ increments. The purple regions highlight the different regions used in calculating the integrated spectra, for the northern and southern lobes and the two hotspots in the northern lobe. The beam size of the NVSS is shown in the lower left corner. 39
4.3 The spectrum of the core of the radio galaxy PGC2285791 is shown for different frequencies, with the frequency-flux (MHz, mJy) pairs of: (73.79, 19.76), (141.45, 7.34), (147.50, 7.47) and (1400.00, 1.04), integrated over the LoTSS beam size. 40
4.4 The integrated spectra of the northern and southern lobes at the LoTSS and NVSS frequencies for the radio galaxy PGC2285791: the red frequency-flux (MHz, mJy) pairs for the northern lobe are (141.45, 178.64) and (1400.00, 28.15); the blue frequency-flux pairs for the southern lobe are (141.45, 111.62) and (1400.00, 19.13). 41
4.5 Top: background ESO-DSS-2-Red image of PGC2285791 overlaid with gray LoTSS contours at [1.74, 3.48, 5.22, 6.96, 8.7, 10.44, 12.18, 13.92, 15.66] mJy/beam. Bottom: background WISE image (rgb image from bands W1, W2 and W3) of PGC2285791 overlaid with gray LoTSS contours having the same contour properties as the top image. The red and blue overlaid squares are sources from the Gaia-DR1 pulled from the cross-correlation tool Aladin [8, 26]. The yellow square indicates the position of the hotspot and its possible optical counterpart. 42
4.6 The SED of the core of the radio galaxy PGC2285791 with previously known optical (blue), infrared (green) and radio (red) data points plotted with the addition of the VLSSr (magenta), LoTSS (black), TGSS (grey overlaps with black) and NVSS (navy) data points. 43
4.7 Spectral index maps of PGC2285791 computed from the LoTSS and NVSS maps at 141 MHz and 1.4 GHz, respectively. In the creation of the spectral index maps we clipped signals that were less than 3 times the respective rms noise. (a): spectral index map derived from the LoTSS beam smoothed to match the resolution of the NVSS beam and the NVSS beam overlaid with LoTSS contours (black) and NVSS contours (red) to show the source steepening. (b): The same spectral index map as (a). (c): spectral index error map of (a). 45

4.8 First row: the LoTSS 141.45 MHz continuum map of Source 01 overlaid with black LoTSS contours starting at 3σ (σ = 0.91 mJy/beam) with 2σ increments. Second row: continuum maps from the NVSS, TGSS and VLSSr surveys of Source 01 overlaid with black contours from each survey starting at 3σ ($\sigma_{\rm NVSS}$ = 0.40 mJy/beam, $\sigma_{\rm TGSS}$ = 1.64 mJy/beam, $\sigma_{\rm VLSSr}$ = 63.62 mJy/beam) with 2σ increments. Third row: the two-frequency radio spectral index maps computed from the LoTSS map at 141.45 MHz in conjunction with the NVSS map at 1.4 GHz (left), TGSS map at 141.45 MHz (middle) and VLSSr map at 73.79 MHz (right). Last row: the two-frequency radio spectral index error maps computed from the LoTSS map at 141.45 MHz in conjunction with the NVSS map at 1.4 GHz (left), TGSS map at 141.45 MHz (middle) and VLSSr map at 73.79 MHz (right). . . . 48

4.9 First row: the LoTSS 141.45 MHz continuum map of Source 02 overlaid with black LoTSS contours starting at 3σ (σ = 0.68 mJy/beam) with 2σ increments. Second row: continuum maps from the NVSS, TGSS and VLSSr surveys of Source 02 overlaid with black contours from each survey starting at 3σ ($\sigma_{\rm NVSS}$ = 0.99 mJy/beam, $\sigma_{\rm TGSS}$ = 2.85 mJy/beam, $\sigma_{\rm VLSSr}$ = 85.14 mJy/beam) with 2σ increments. Third row: the two-frequency radio spectral index maps computed from the LoTSS map at 141.45 MHz in conjunction with the NVSS map at 1.4 GHz (left), TGSS map at 141.45 MHz (middle) and VLSSr map at 73.79 MHz (right). Last row: the two-frequency radio spectral index error maps computed from the LoTSS map at 141.45 MHz in conjunction with the NVSS map at 1.4 GHz (left), TGSS map at 141.45 MHz (middle) and VLSSr map at 73.79 MHz (right). . . . 49

4.10 First row: the LoTSS 141.45 MHz continuum map of Source 03 overlaid with black LoTSS contours starting at 3σ (σ = 0.62 mJy/beam) with 2σ increments. Second row: continuum maps from the NVSS, TGSS and VLSSr surveys of Source 03 overlaid with black contours from each survey starting at 3σ ($\sigma_{\rm NVSS}$ = 0.50 mJy/beam, $\sigma_{\rm TGSS}$ = 4.59 mJy/beam, $\sigma_{\rm VLSSr}$ = 99.84 mJy/beam) with 2σ increments. Third row: the two-frequency radio spectral index maps computed from the LoTSS map at 141.45 MHz in conjunction with the NVSS map at 1.4 GHz (left), TGSS map at 141.45 MHz (middle) and VLSSr map at 73.79 MHz (right). Last row: the two-frequency radio spectral index error maps computed from the LoTSS map at 141.45 MHz in conjunction with the NVSS map at 1.4 GHz (left), TGSS map at 141.45 MHz (middle) and VLSSr map at 73.79 MHz (right). . . . 50

4.11 First row: the LoTSS 141.45 MHz continuum map of PGC2285791 overlaid with black LoTSS contours starting at 3σ (σ = 0.58 mJy/beam) with 2σ increments. Second row: continuum maps from the NVSS, TGSS and VLSSr surveys of PGC2285791 overlaid with black contours from each survey starting at 3σ ($\sigma_{\rm NVSS}$ = 0.57 mJy/beam, $\sigma_{\rm TGSS}$ = 2.99 mJy/beam, $\sigma_{\rm VLSSr}$ = 76.02 mJy/beam) with 2σ increments. Third row: the two-frequency radio spectral index maps computed from the LoTSS map at 141.45 MHz in conjunction with the NVSS map at 1.4 GHz (left), TGSS map at 141.45 MHz (middle) and VLSSr map at 73.79 MHz (right). Last row: the two-frequency radio spectral index error maps computed from the LoTSS map at 141.45 MHz in conjunction with the NVSS map at 1.4 GHz (left), TGSS map at 141.45 MHz (middle) and VLSSr map at 73.79 MHz (right). . . . 51

4.12 First row: the LoTSS 141.45 MHz continuum map of Source 05 overlaid with black LoTSS contours starting at 3σ (σ = 1.29 mJy/beam) with 2σ increments. Second row: continuum maps from the NVSS, TGSS and VLSSr surveys of Source 05 overlaid with black contours from each survey starting at 3σ ($\sigma_{\rm NVSS}$ = 0.46 mJy/beam, $\sigma_{\rm TGSS}$ = 1.90 mJy/beam, $\sigma_{\rm VLSSr}$ = 72.07 mJy/beam) with 2σ increments. Third row: the two-frequency radio spectral index maps computed from the LoTSS map at 141.45 MHz in conjunction with the NVSS map at 1.4 GHz (left), TGSS map at 141.45 MHz (middle) and VLSSr map at 73.79 MHz (right). Last row: the two-frequency radio spectral index error maps computed from the LoTSS map at 141.45 MHz in conjunction with the NVSS map at 1.4 GHz (left), TGSS map at 141.45 MHz (middle) and VLSSr map at 73.79 MHz (right). . . . 52

4.13 First row: the LoTSS 141.45 MHz continuum map of Source 06 overlaid with black LoTSS contours starting at 3σ (σ = 1.20 mJy/beam) with 2σ increments. Second row: continuum maps from the NVSS, TGSS and VLSSr surveys of Source 06 overlaid with black contours from each survey starting at 3σ ($\sigma_{\rm NVSS}$ = 0.46 mJy/beam, $\sigma_{\rm TGSS}$ = 1.85 mJy/beam, $\sigma_{\rm VLSSr}$ = 76.68 mJy/beam) with 2σ increments. Third row: the two-frequency radio spectral index maps computed from the LoTSS map at 141.45 MHz in conjunction with the NVSS map at 1.4 GHz (left), TGSS map at 141.45 MHz (middle) and VLSSr map at 73.79 MHz (right). Last row: the two-frequency radio spectral index error maps computed from the LoTSS map at 141.45 MHz in conjunction with the NVSS map at 1.4 GHz (left), TGSS map at 141.45 MHz (middle) and VLSSr map at 73.79 MHz (right). . . . 53

4.14 First row: the LoTSS 141.45 MHz continuum map of Source 07 overlaid with black LoTSS contours starting at 3σ (σ = 1.17 mJy/beam) with 2σ increments. Second row: continuum maps from the NVSS, TGSS and VLSSr surveys of Source 07 overlaid with black contours from each survey starting at 3σ ($\sigma_{\rm NVSS}$ = 0.51 mJy/beam, $\sigma_{\rm TGSS}$ = 3.74 mJy/beam, $\sigma_{\rm VLSSr}$ = 74.61 mJy/beam) with 2σ increments. Third row: the two-frequency radio spectral index maps computed from the LoTSS map at 141.45 MHz in conjunction with the NVSS map at 1.4 GHz (left), TGSS map at 141.45 MHz (middle) and VLSSr map at 73.79 MHz (right). Last row: the two-frequency radio spectral index error maps computed from the LoTSS map at 141.45 MHz in conjunction with the NVSS map at 1.4 GHz (left), TGSS map at 141.45 MHz (middle) and VLSSr map at 73.79 MHz (right). . . . 54

4.15 First row: the LoTSS 141.45 MHz continuum map of PGC2396883 overlaid with black LoTSS contours starting at 3σ (σ = 1.52 mJy/beam) with 2σ increments. Second row: continuum maps from the NVSS, TGSS and VLSSr surveys of PGC2396883 overlaid with black contours from each survey starting at 3σ ($\sigma_{\rm NVSS}$ = 0.50 mJy/beam, $\sigma_{\rm TGSS}$ = 4.59 mJy/beam, $\sigma_{\rm VLSSr}$ = 79.30 mJy/beam) with 2σ increments. Third row: the two-frequency radio spectral index maps computed from the LoTSS map at 141.45 MHz in conjunction with the NVSS map at 1.4 GHz (left), TGSS map at 141.45 MHz (middle) and VLSSr map at 73.79 MHz (right). Last row: the two-frequency radio spectral index error maps computed from the LoTSS map at 141.45 MHz in conjunction with the NVSS map at 1.4 GHz (left), TGSS map at 141.45 MHz (middle) and VLSSr map at 73.79 MHz (right). . . . 55

4.16 First row: the LoTSS 141.45 MHz continuum map of Source 09 overlaid with black LoTSS contours starting at 3σ (σ = 0.86 mJy/beam) with 2σ increments. Second row: continuum maps from the NVSS, TGSS and VLSSr surveys of Source 09 overlaid with black contours from each survey starting at 3σ ($\sigma_{\rm NVSS}$ = 0.59 mJy/beam, $\sigma_{\rm TGSS}$ = 3.63 mJy/beam, $\sigma_{\rm VLSSr}$ = 70.16 mJy/beam) with 2σ increments. Third row: the two-frequency radio spectral index maps computed from the LoTSS map at 141.45 MHz in conjunction with the NVSS map at 1.4 GHz (left), TGSS map at 141.45 MHz (middle) and VLSSr map at 73.79 MHz (right). Last row: the two-frequency radio spectral index error maps computed from the LoTSS map at 141.45 MHz in conjunction with the NVSS map at 1.4 GHz (left), TGSS map at 141.45 MHz (middle) and VLSSr map at 73.79 MHz (right). . . . 56

4.17 First row: the LoTSS 141.45 MHz continuum map of Source 10 overlaid with black LoTSS contours starting at 3σ (σ = 1.02 mJy/beam) with 2σ increments. Second row: continuum maps from the NVSS, TGSS and VLSSr surveys of Source 10 overlaid with black contours from each survey starting at 3σ ($\sigma_{\rm NVSS}$ = 0.50 mJy/beam, $\sigma_{\rm TGSS}$ = 2.02 mJy/beam, $\sigma_{\rm VLSSr}$ = 86.59 mJy/beam) with 2σ increments. Third row: the two-frequency radio spectral index maps computed from the LoTSS map at 141.45 MHz in conjunction with the NVSS map at 1.4 GHz (left), TGSS map at 141.45 MHz (middle) and VLSSr map at 73.79 MHz (right). Last row: the two-frequency radio spectral index error maps computed from the LoTSS map at 141.45 MHz in conjunction with the NVSS map at 1.4 GHz (left), TGSS map at 141.45 MHz (middle) and VLSSr map at 73.79 MHz (right). . . . 57

4.18 First row: the LoTSS 141.45 MHz continuum map of Source 11 overlaid with black LoTSS contours starting at 3σ (σ = 1.05 mJy/beam) with 2σ increments. Second row: continuum maps from the NVSS, TGSS and VLSSr surveys of Source 11 overlaid with black contours from each survey starting at 3σ ($\sigma_{\rm NVSS}$ = 0.51 mJy/beam, $\sigma_{\rm TGSS}$ = 2.08 mJy/beam, $\sigma_{\rm VLSSr}$ = 87.18 mJy/beam) with 2σ increments. Third row: the two-frequency radio spectral index maps computed from the LoTSS map at 141.45 MHz in conjunction with the NVSS map at 1.4 GHz (left), TGSS map at 141.45 MHz (middle) and VLSSr map at 73.79 MHz (right). Last row: the two-frequency radio spectral index error maps computed from the LoTSS map at 141.45 MHz in conjunction with the NVSS map at 1.4 GHz (left), TGSS map at 141.45 MHz (middle) and VLSSr map at 73.79 MHz (right). . . . 58

4.19 First row: the LoTSS 141.45 MHz continuum map of Source 12 overlaid with black LoTSS contours starting at 3σ (σ = 1.09 mJy/beam) with 2σ increments. Second row: continuum maps from the NVSS, TGSS and VLSSr surveys of Source 12 overlaid with black contours from each survey starting at 3σ ($\sigma_{\rm NVSS}$ = 0.50 mJy/beam, $\sigma_{\rm TGSS}$ = 1.80 mJy/beam, $\sigma_{\rm VLSSr}$ = 75.89 mJy/beam) with 2σ increments. Third row: the two-frequency radio spectral index maps computed from the LoTSS map at 141.45 MHz in conjunction with the NVSS map at 1.4 GHz (left), TGSS map at 141.45 MHz (middle) and VLSSr map at 73.79 MHz (right). Last row: the two-frequency radio spectral index error maps computed from the LoTSS map at 141.45 MHz in conjunction with the NVSS map at 1.4 GHz (left), TGSS map at 141.45 MHz (middle) and VLSSr map at 73.79 MHz (right). . . . 59

4.20 First row: the LoTSS 141.45 MHz continuum map of Source 13 overlaid with black LoTSS contours starting at 3σ (σ = 0.67 mJy/beam) with 2σ increments. Second row: continuum maps from the NVSS, TGSS and VLSSr surveys of Source 13 overlaid with black contours from each survey starting at 3σ ($\sigma_{\rm NVSS}$ = 0.46 mJy/beam, $\sigma_{\rm TGSS}$ = 2.95 mJy/beam, $\sigma_{\rm VLSSr}$ = 82.32 mJy/beam) with 2σ increments. Third row: the two-frequency radio spectral index maps computed from the LoTSS map at 141.45 MHz in conjunction with the NVSS map at 1.4 GHz (left), TGSS map at 141.45 MHz (middle) and VLSSr map at 73.79 MHz (right). Last row: the two-frequency radio spectral index error maps computed from the LoTSS map at 141.45 MHz in conjunction with the NVSS map at 1.4 GHz (left), TGSS map at 141.45 MHz (middle) and VLSSr map at 73.79 MHz (right). . . . 60

4.21 First row: the LoTSS 141.45 MHz continuum map of B31059+460 overlaid with black LoTSS contours starting at 3σ (σ = 0.79 mJy/beam) with 2σ increments. Second row: continuum maps from the NVSS, TGSS and VLSSr surveys of B31059+460 overlaid with black contours from each survey starting at 3σ ($\sigma_{\rm NVSS}$ = 0.49 mJy/beam, $\sigma_{\rm TGSS}$ = 2.76 mJy/beam, $\sigma_{\rm VLSSr}$ = 112.18 mJy/beam) with 2σ increments. Third row: the two-frequency radio spectral index maps computed from the LoTSS map at 141.45 MHz in conjunction with the NVSS map at 1.4 GHz (left), TGSS map at 141.45 MHz (middle) and VLSSr map at 73.79 MHz (right). Last row: the two-frequency radio spectral index error maps computed from the LoTSS map at 141.45 MHz in conjunction with the NVSS map at 1.4 GHz (left), TGSS map at 141.45 MHz (middle) and VLSSr map at 73.79 MHz (right). 61

4.22 First row: the LoTSS 141.45 MHz continuum map of ABELL 1550 overlaid with black LoTSS contours starting at 3σ (σ = 0.46 mJy/beam) with 2σ increments. Second row: continuum maps from the NVSS, TGSS and VLSSr surveys of ABELL 1550 overlaid with black contours from each survey starting at 3σ ($\sigma_{\rm NVSS}$ = 0.46 mJy/beam, $\sigma_{\rm TGSS}$ = 3.47 mJy/beam, $\sigma_{\rm VLSSr}$ = 87.97 mJy/beam) with 2σ increments. Third row: the two-frequency radio spectral index maps computed from the LoTSS map at 141.45 MHz in conjunction with the NVSS map at 1.4 GHz (left), TGSS map at 141.45 MHz (middle) and VLSSr map at 73.79 MHz (right). Last row: the two-frequency radio spectral index error maps computed from the LoTSS map at 141.45 MHz in conjunction with the NVSS map at 1.4 GHz (left), TGSS map at 141.45 MHz (middle) and VLSSr map at 73.79 MHz (right). 62

4.23 First row: the LoTSS 141.45 MHz continuum map of ABELL 1682 overlaid with black LoTSS contours starting at 3σ ($\sigma = 2.08$ mJy/beam) with 2σ increments. Second row: continuum maps from the NVSS, TGSS and VLSSr surveys of ABELL 1682 overlaid with black contours from each survey starting at 3σ ($\sigma_{\rm NVSS} = 0.53$ mJy/beam, $\sigma_{\rm TGSS} = 4.70$ mJy/beam, $\sigma_{\rm VLSSr} = 87.97$ mJy/beam) with 2σ increments. Third row: the two-frequency radio spectral index maps computed from the LoTSS map at 141.45 MHz in conjunction with the NVSS map at 1.4 GHz (left), TGSS map at 141.45 MHz (middle) and VLSSr map at 73.79 MHz (right). Last row: the two-frequency radio spectral index error maps computed from the LoTSS map at 141.45 MHz in conjunction with the NVSS map at 1.4 GHz (left), TGSS map at 141.45 MHz (middle) and VLSSr map at 73.79 MHz (right). 63

4.24 First row: the LoTSS 141.45 MHz continuum map of IC 711 overlaid with black LoTSS contours starting at 3σ ($\sigma = 2.13$ mJy/beam) with 2σ increments. Second row: continuum maps from the NVSS, TGSS and VLSSr surveys of IC 711 overlaid with black contours from each survey starting at 3σ ($\sigma_{\rm NVSS} = 0.62$ mJy/beam, $\sigma_{\rm TGSS} = 5.55$ mJy/beam, $\sigma_{\rm VLSSr} = 104.4$ mJy/beam) with 2σ increments. Third row: the two-frequency radio spectral index maps computed from the LoTSS map at 141.45 MHz in conjunction with the NVSS map at 1.4 GHz (left), TGSS map at 141.45 MHz (middle) and VLSSr map at 73.79 MHz (right). Last row: the two-frequency radio spectral index error maps computed from the LoTSS map at 141.45 MHz in conjunction with the NVSS map at 1.4 GHz (left), TGSS map at 141.45 MHz (middle) and VLSSr map at 73.79 MHz (right). . . . 64

List of Tables

3.1 Data on the studied extended sources detected by *LoTSS*. Column (1): Radio source names; Column (2)-(3): Right Ascension (J2000) and Declination (J2000); Column (4)-(7): Integrated flux density at the position of the core (as seen by LoTSS) for the different surveys, integrated over an area equal to the size of the LoTSS beam; Column (8)-(9): Two-frequency radio spectral indices derived from the frequency of the survey bands given in Column (4)-(7). 31

3.2 Data on the studied extended sources detected by *LoTSS*. Column (1): Radio source names; Column (2)-(3): Right Ascension (J2000) and Declination (J2000); Column (4)-(7): Integrated flux density at the position of the core (as seen by LoTSS) for the different surveys, integrated over an area equal to the size of the NVSS beam; Column (8)-(9): Two-frequency radio spectral indices derived from the frequency of the survey bands given in Column (4)-(7). 32

3.3 Data on the studied extended sources detected by *LoTSS*. Column (1): Radio source names; Column (2)-(3): Right Ascension (J2000) and Declination (J2000); Column (4)-(7): Integrated flux density at the position of the core (as seen by LoTSS) for the different surveys, integrated over an area equal to the size of the VLSSr beam; Column (8)-(9): Two-frequency radio spectral indices derived from the frequency of the survey bands given in Column (4)-(7). 33

Abbreviations

AGN	Active Galactic Nuclei
DSS	ESO-Digitized Sky Surveys-2-Red
ESO	European Southern Observatory
FSRQ	Flat-spectrum radio quasar
GMRT	Giant Metrewave Radio Telescope
IR	Infrared
Jy	Jansky
LOFAR	Low Frequency Array
LoTSS	LOFAR Two-metre Sky Survey
NRAO	National Radio Astronomy Observatory
NVSS	NRAO VLA Sky Survey
RG	Radio galaxy
SDSS	Sloan Digital Sky Survey
SED	Spectral energy distribution
SKA	Square Kilometre Array
SSDC	Space Science Data Center
TGSS	TIFR GMRT Sky Survey
TIFR	Tata Institute of Fundamental Research
VLA	Very Large Array
VLSS	VLA Low-Frequency Sky Survey
VLSSr	VLSS Redux
WISE	Wide-field Infrared Survey Explorer

I dedicate this work to
Busisiwe, Nomgqibelo and the memory of Bonginkosi Thwala

Thwala, Mnyamande, KaSiwela
Mkhonto oduma njengezulu
Unomlithi, Unomadinana
Zonke izizwe zithi mlethe
Thwala omkhulu!!!

Chapter 1

Introduction

From elementary physics we know that the electromagnetic spectrum varies vastly originating from high-energy charged particles (gamma and X-ray wavelengths) to low-energy charged particles (radio wavelengths). The wide variation in particle energies between these observable wavelength limits allows us to observe different types of electromagnetic radiation (produced by a charged particle emitting radiation at the observed frequency) which can be grouped into different wavelength/frequency bands (see Fig. 1.1).

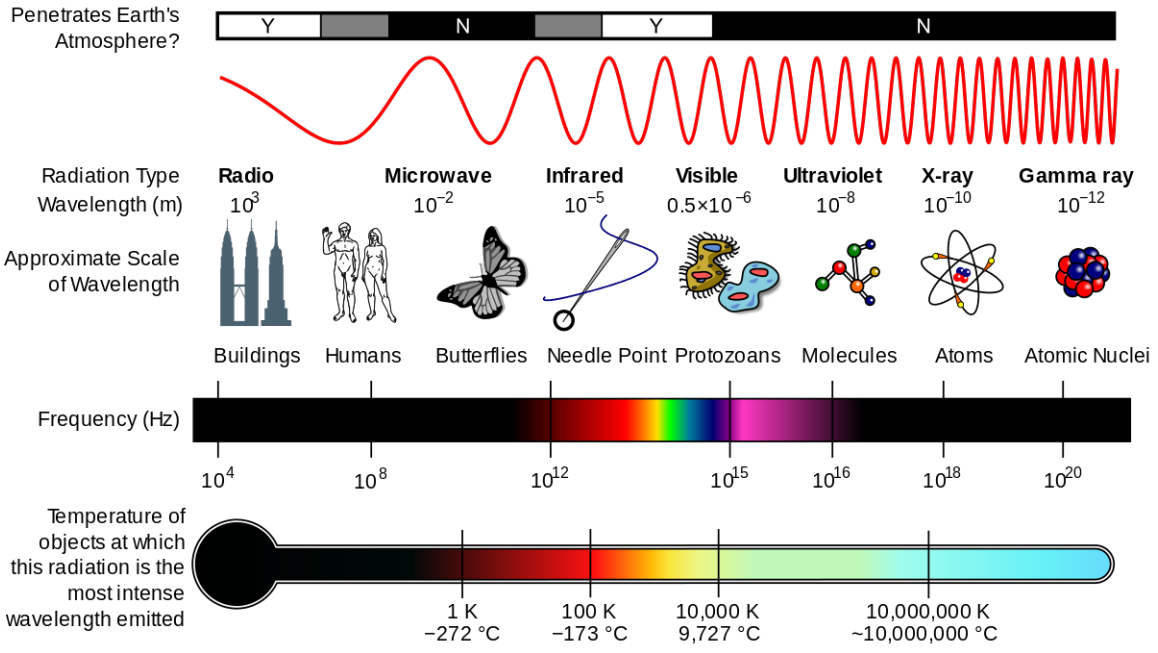


FIGURE 1.1: An illustration of the large variance in frequency and wavelengths found in the electromagnetic spectrum, along with intuitive scales of the different wavelengths, the temperature in these bands and the possibility of observing these signal from Earth's surface [33].

In each wavelength band there are different emission mechanisms at play, giving rise to unique phenomena in that wavelength band. This then necessitates specialised probes to study the physics and physical dynamics driving these mechanisms. A possible avenue we can take to create a coherent and comprehensive picture of the physics behind the electromagnetic spectrum, is to study astronomical bodies.

This is one of the main motivations behind multi-wavelength astrophysics, where a collection of telescopes (located in space and on the surface of Earth, shown in Fig. 1.2) are used to probe distinct astronomical bodies across the observable wavelengths.

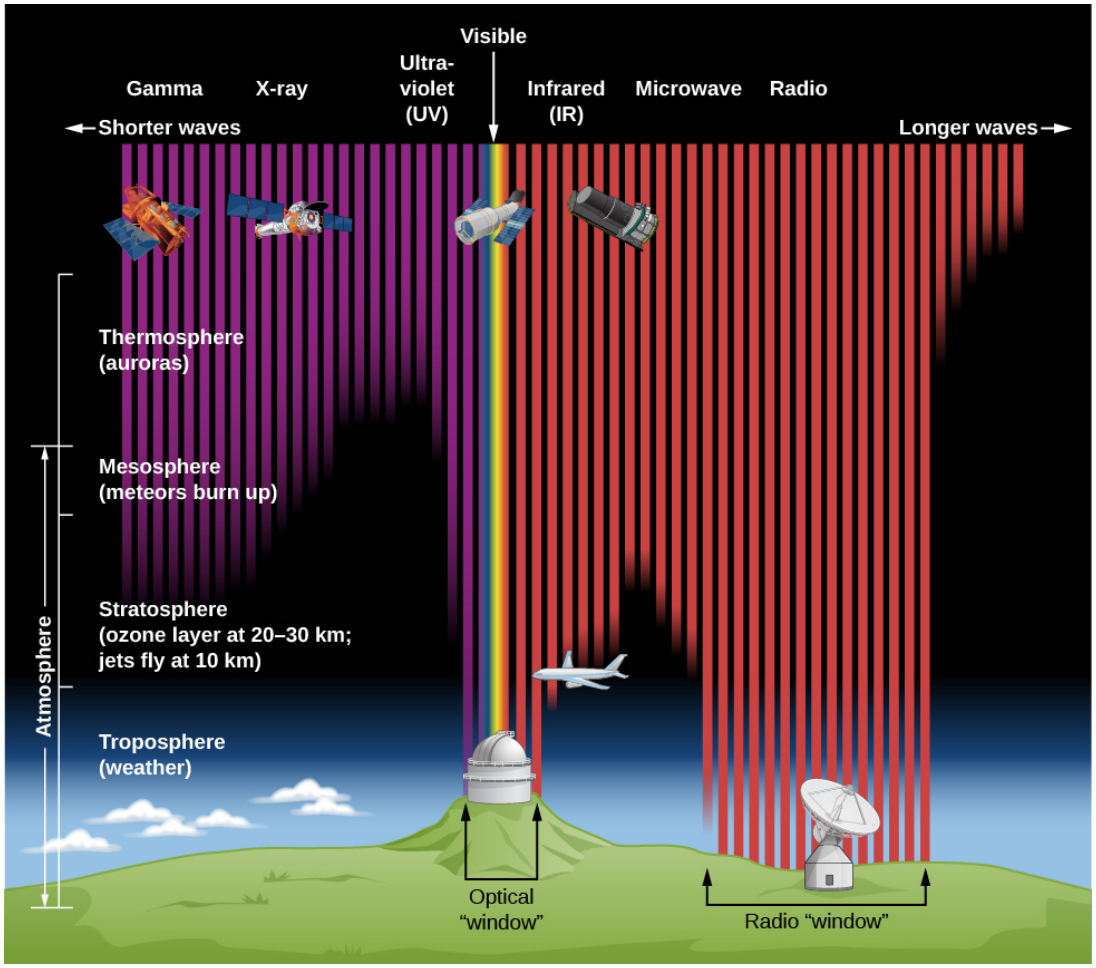


FIGURE 1.2: An illustration of the different telescopes used as probes in astrophysics and the "windows" (wavelength regions of the electromagnetic spectrum) we can probe from the surface of Earth [37].

The work presented in this study is centred around radio astronomy as the main probe. We used data from other wavelengths to complement the characterisation of the extended radio sources we present in this study (the description of the data used is detailed in Chapter 2). The observables that we probe are produced when the energy from a radio source is turned into radiation (radio telescopes measure the intensity of this radiation),

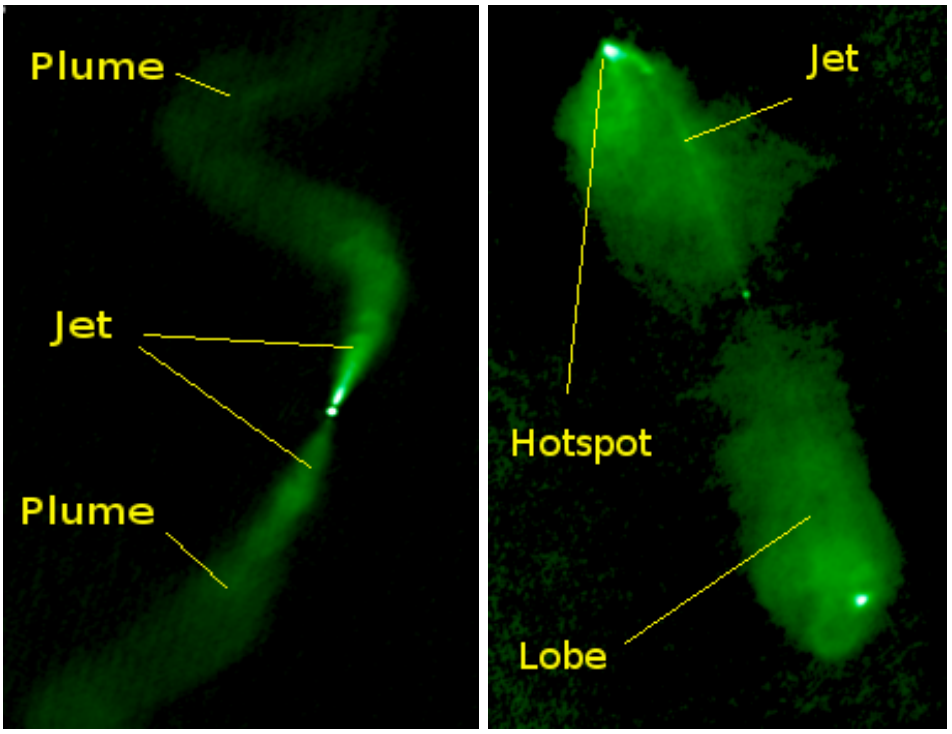
and the three main emission mechanisms we can observe in radio astronomy are; spectral line emission, thermal and non-thermal emission processes. We will now look at radio galaxies, their morphology and a few key features characterising the different emission mechanisms seen in these sources.

1.1 Radio galaxies

Galaxies are systems of stars, dust and gas that are gravitationally bound and dynamically interacting with each other through the exchange of matter and energy. These dynamic interactions produce structures that determine the energetics of photons that we observe from these systems. Radio galaxies are essentially active galaxies which radiate their photons in the radio wavelength band of the electromagnetic spectrum.

The morphology of radio sources can be broken down into different constituents: namely, the core, normally the source of the observed emission and powered by a black hole; jets, collimated regions where lighter charged relativistic particles, electrons and positrons, are accelerated by the presence of a magnetic field; lobes, extended "elliptical" structures dominated by low surface brightness diffuse emission; plumes, similar to lobes except the approximated shape is not elliptical and they normally show no signs of hotspots; and hotspots, termination points for jets and a possible site for shock waves resulting from interactions between the jet and the intracluster medium.

In 1974 Fanaroff & Riley [23] devised a classification scheme for the morphology of extragalactic radio sources based on the relative position of the high and low brightness regions which were found to be correlated with the luminosity of the sources . In their presented note They suggested a division of extragalactic radio sources based on the luminosity of the sources and noticed that sources with radio luminosities below and above $\approx 10^{25}$ W Hz^{-1} at a frequency of 178 MHz, have distinct morphologies. They then proposed grouping extragalactic radio sources into two classes based on the morphology of the large-scale radio emission. Sources which lie below $\approx 10^{25}$ W Hz^{-1} are observed to have no hotspots, are less energetic and have wide differences in morphology of the extended emission (see plumes in Fig. 1.3(a)). These sources were classified as Class I and are now commonly know as FR-I type galaxies. Sources which lie above $\approx 10^{25}$ W Hz^{-1} are observed to have hotspots, are more energetic and characterised by having a double lobed morphology with their extended emission terminated by hotspots (see Fig. 1.3(b)). These sources were classified as Class II and are now commonly know as FR-II type galaxies.



(a) Radio galaxy 3C31 (FR-I type galaxy) [44] (b) Radio galaxy 3C98 (FR-II type galaxy) [45]

FIGURE 1.3: A side by side view of the two radio morphology classes devised by Fanaroff & Riley based on the large-scale radio emission of extragalactic radio sources.

This gives us a macroscopic view of extended radio sources. We need to understand the underlying microscopic mechanisms that shape these morphologies in order to better understand how the observed large-scale radio emission emerges. We now shift our attention to the key features characterising the different emission mechanisms we observe in radio sources.

1.2 Spectral line emission

Spectral lines are defined to be narrow ($\delta\nu \ll \nu$) emission or absorption features in the spectra of gaseous and ionized sources [60]. The background to these spectral features is produced by the recombination of electrons with atomic nuclei to form atoms that are usually in an excited state. As atoms cascade down to the ground state, they emit a photon with an energy equal to the difference between the initial and final atomic state, and such spectral lines are called recombination lines.

The emitted photon then travels through different clouds of gas. Because of the difference in the energetics, the gas clouds imprint different absorption and emission features along

the line of sight of the photon. This information can then be used to probe gas clouds that lie along the line of sight of the observed spectra.

Examples of radio spectral lines, which are intrinsically quantum phenomena, include recombination lines of ionized hydrogen (Fig. 1.4) and heavier atoms, astrophysical masers, 21 cm hyperfine line of interstellar H_I, and rotational lines of polar molecules such as carbon monoxide (CO) [60]. In our characterisation we used the SDSS spectra to obtain information about the galaxy type and redshift of the extended radio sources, provided the SDSS catalogue has spectra on that particular source.

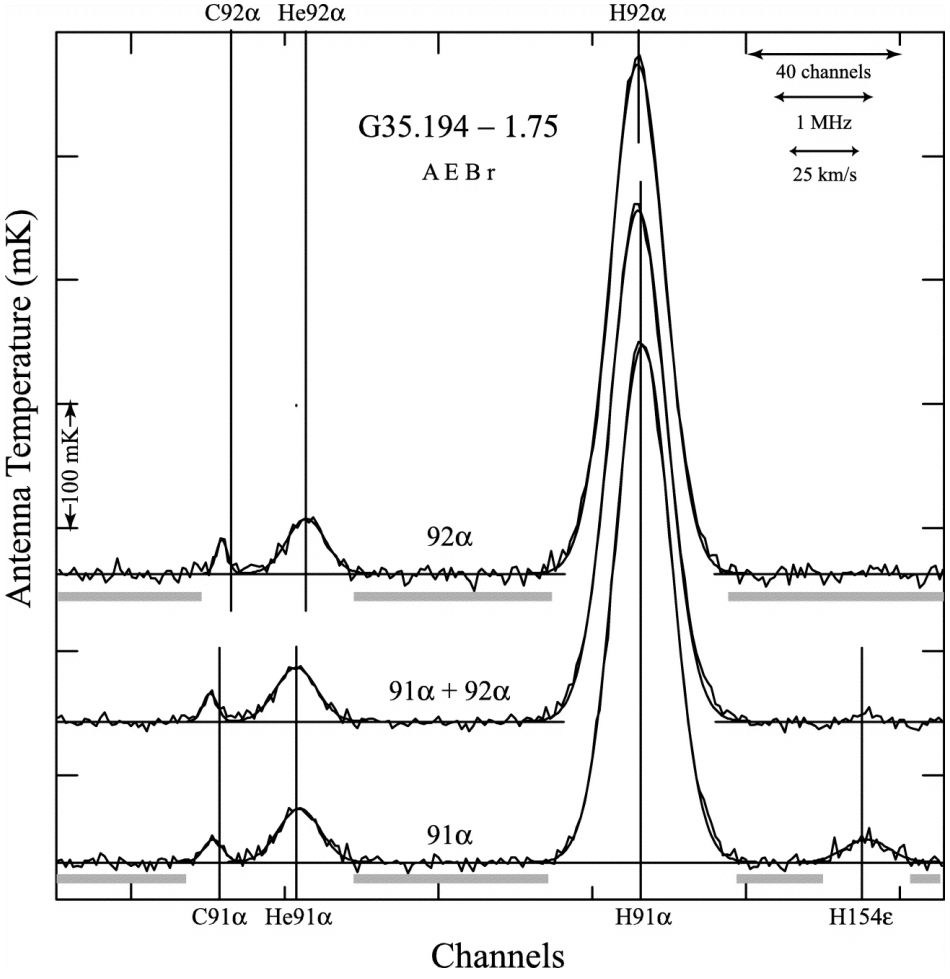


FIGURE 1.4: An example of observed recombination-line spectra from the 91α and 92α transitions of hydrogen, helium, and carbon observed in an H_{II} region [60].

1.3 Continuum emission

From the above discussion, we have seen that spectral line emissions are a result of atomic processes that only have very specific quantised energies caused by differences in the initial and final atomic states of the cascading atom. Continuum emission on the

other hand, results from the acceleration of charged particles. Since continuum emission results from processes where the energy exchange is not quantised, the emitted photons may have a continuous energy distribution [71]. We now give a brief introduction to the two processes that result in continuum emission: thermal and non-thermal emission processes.

1.3.1 Thermal emission processes

An object is said to be in local thermodynamic equilibrium (LTE), if the emitting/absorbing object is in thermal equilibrium at a well-defined temperature T [57].

In thermodynamics a blackbody is defined as a perfect absorber at all frequencies, with the most fundamental feature of blackbody radiation being equilibrium radiation [57]. Thermal emission is produced by a source whose emitting particles are in LTE; otherwise nonthermal emission is produced [58]. Because of this property thermal emission processes are dependent only on the temperature of the emitting object.

The key characteristics of blackbodies are that they emit energy across the entire electromagnetic spectrum, with objects at higher temperatures emitting more radiation and peaking at shorter wavelengths, as shown in Fig. 1.5. In this study, we do not look in depth at thermal emission processes because we are interested in studying low-frequency radio continuum observations of extended (radio) galaxies. This is motivated by the dominance of synchrotron emission (a nonthermal emission process detailed in the following section) as the dominant emission mechanism observed at low frequencies.

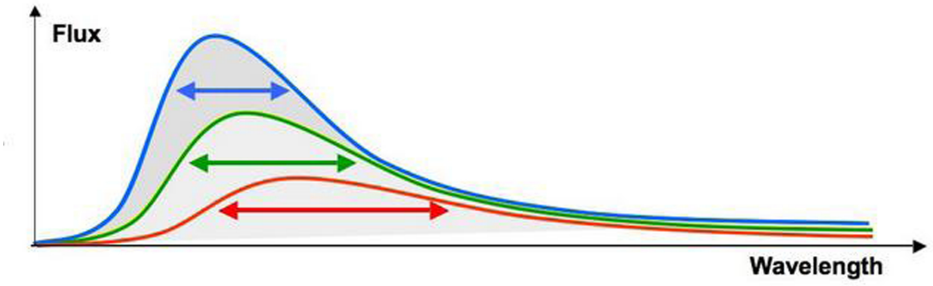


FIGURE 1.5: A plot of the flux against wavelength of a blackbody emitter, showing that such an object will emit a spectrum of radiation which peaks at a wavelength (or frequency) dependent only on the objects temperature. As the source temperature increases the peak wavelength decreases. This is why hot stars appear blue and cool stars appear red [71].

1.3.2 Non-thermal emission processes

An ensemble of radiating electrons with a decreasing power-law energy spectrum is common in astrophysical systems (e.g., the cosmic ray flux) [10]. Such an ensemble in the presence of a magnetic field will emit nonthermal emission (in the form of synchrotron emission) with a descending power law [10].

This then leads us to the distinction that thermal emission processes are largely driven by the acceleration of charged particles in an electric field and are dependent on sources with particles emitting their radiation in LTE. Whilst most non-thermal emission processes occur in ionized plasmas with free electrons being driven by an accompanying magnetic field.

Two processes that give rise to nonthermal emission include synchrotron radiation and inverse Compton scattering. The extended radio sources we looked at in this study produce synchrotron emission (with an illustration in Fig. 1.6), and therefore we mainly focused on this nonthermal emission process. Synchrotron emission is the acceleration of lighter charged ultrarelativistic particles (electrons and positrons) in the presence of a magnetic field. The relativistic electrons in nearly all synchrotron sources have power-law energy distributions, so they are not in LTE [59]. However, a synchrotron source with a relativistic Maxwellian electron-energy distribution would be a thermal source, so "synchrotron" and "nonthermal" are not completely synonymous [59].

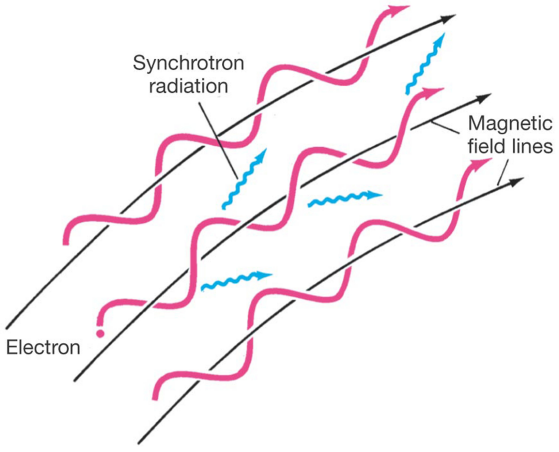


FIGURE 1.6: A simple illustration of a relativistic electron being accelerated by a magnetic field and the synchrotron radiation that is emitted as the charged particle gets boosted by the magnetic field [11]. This is the source of the diffuse emission we wish to study from the extended radio sources we looked at in this study.

As mentioned later on, the lack of high frequency data in the soft and hard X-ray ranges do not allow us to test the inverse Compton (on synchrotron) branch of the core emission

from the extended radio sources. X-ray data could also be used to identify possible inverse Compton scattering X-ray emission from the different radio galaxy lobes.

We can now use Fig. 1.7 to sum up the typical features we are likely to observe from spectral line emission, thermal and non-thermal emission processes. The observed spectral line emission is shown in black, with the absorption and emission features appearing as deviations from the the overall spectrum. The expected descending power law distribution from synchrotron radiation is shown in red, highlighting the fact that at low-frequencies we have a higher contribution from low-energy photons compared to high-energy photons. As the frequency increases we expect thermal emission processes from free-free absorption and thermal dust to become dominant. The case of a nearby starburst galaxy M82 is also presented in Fig. 1.8 as an example.

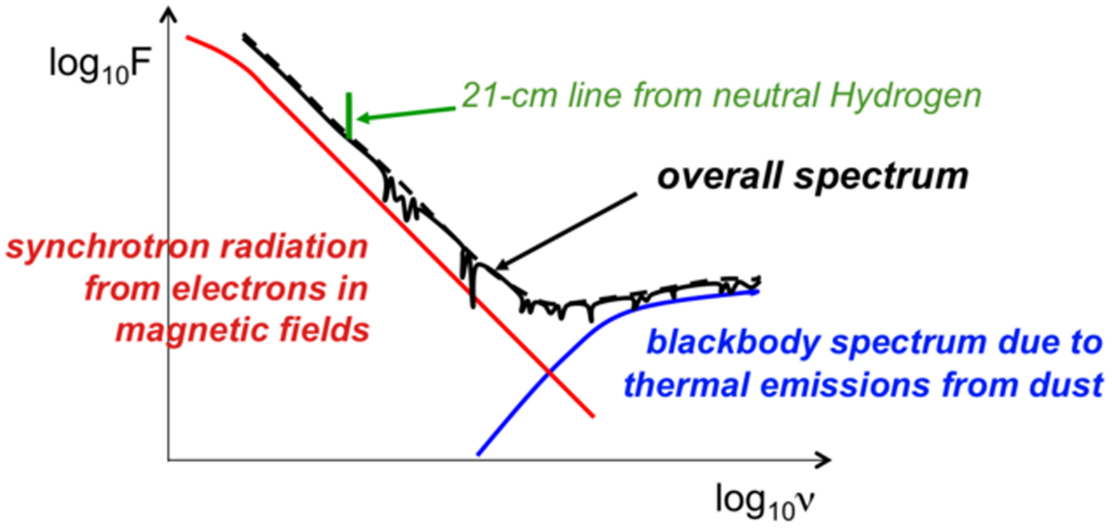


FIGURE 1.7: A log-log scale plot of a composite spectrum for a typical galaxy observed over a wide range of frequencies, from radio to visible [71].

Now that we have covered some of the basic concepts that are necessary to characterise extended radio sources, we proceed to provide motivation as to why it is necessary to study and characterise the core, the extended structure and the environment of such sources.

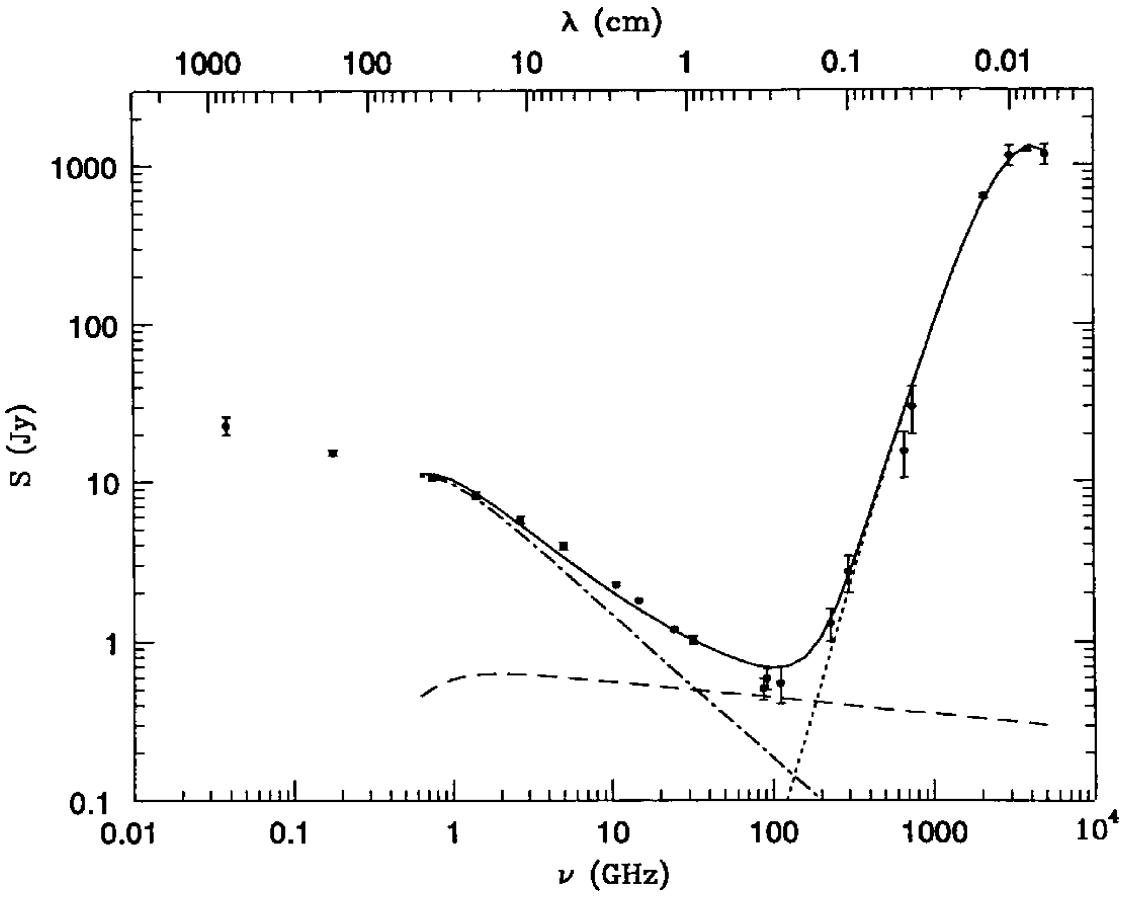


FIGURE 1.8: The radio and far-infrared spectrum of the nearby starburst galaxy M82 [18]. The contribution of free-free emission is indicated by the nearly horizontal dashed line. Synchrotron radiation (dot-dash line) and thermal dust emission (dots) dominate at low and high frequencies, respectively. Free-free absorption from H_{II} regions distributed throughout the galaxy absorbs some of the synchrotron radiation and flattens the overall spectrum at the lowest frequencies [59].

1.4 Motivation for this work

Low-frequency radio continuum observations of radio galaxies are very important because the associated synchrotron emission probes the aged and low-energy electrons which are less affected by energy losses and, therefore, can propagate further away from their site of origin (assuming that the diffusion coefficient does not vary with particle energy) [48]. Depending on the magnetic field strength and spatial extension, one would expect to see a large radio synchrotron emission in extended sources [48] (see the case of the $\sim$ 700 kpc remnant radio galaxy J1828+49 studied with LOFAR [12]). This is in fact the case of radio galaxies with jets or outflows: AGN-powered radio galaxies have relativistic jets extended and collimated for tens to hundreds of kpc; outflows are observed to be populated by lower energy electrons [23] which produce irregularly shaped radio lobes which typically extend for smaller distances from the galaxy core.

In order to discover and study new extended emissions at low frequency around radio galaxies we used the LOFAR Two-metre Sky Survey (LoTSS) extended radio sources in the still poorly explored low-frequency region of the electromagnetic spectrum. Exploring the HETDEX Spring Field (see Chapter 2 for details), we were able to identify 17 extended sources for our study in a region of 9.5×8.7 deg^2, an area of the sky between RA: 10h 37m 00s to 11h 48m 00s and DEC: $44°19'00''$ to $52°55'00''$.

In this study we analyse the diffuse emission from these sources at low-frequency, and focus on the properties and the nature of the specific radio galaxy PGC2285791 which shows a bubble-like symmetric radio lobe structure with a prominent radio core. Our study will use the improved sensitivity of the available radio surveys (in particular the LoTSS) and the ability to better resolve radio galaxies for studies of magnetic fields, cosmic ray diffusion and particle acceleration mechanisms in their jets/lobes.

The structure of this dissertation is as follows: the background theory behind the different emission mechanisms that produce the phenomena observed by different surveys was presented in this Chapter. In Chapter 2 the different data sets we use in our analysis are detailed and in Chapter 3 we describe the data analysis techniques. In Chapter 4 we discuss the identification of the extended radio sources extracted from the LoTSS and we study in particular the nature of the extended radio galaxy PGC2285791. We also present a summary of our preliminary results for all extended sources in Chapter 4.2 and draw our conclusion in Chapter 5.

We adopt a flat, vacuum-dominated cosmology with $H_0 = 73.00$ km/sec/Mpc, $\Omega_{\rm matter} = 0.27$ and $\Omega_{\rm vacuum} = 0.73$.

Chapter 2

Description of data

To perform our study of extended radio sources, we searched for extended sources in the LoTSS survey in order to characterise the morphology, integrated spectra and spectral index maps of poorly known or unidentified extended radio sources. We then looked at different imaging surveys available and used the open data across multiple frequencies in order to identify and characterise these sources. In our analysis we used publicly available data from the LoTSS, NVSS, TGSS, VLSSr, WISE, DSS-DR2 and SDSS, surveys. This has added some restrictions on the different analyses carried out, whilst also introducing some uncertainties about the obtained results.

The differences in resolutions and sensitivities across these surveys necessitated careful selection criteria for deciding which surveys to use in this study. For instance, the resolution of the TIFR GMRT Sky Survey (TGSS) is an ideal match to the LoTSS survey. However, the integration time per pointing for TGSS is 15 minutes whilst LoTSS has 8 hours. For compact sources the difference is not of major concern, given that the core of the sources usually have higher intensities compared to the surrounding environment. For extended sources, the difference is a factor since diffuse emission requires a prolonged integration time to better resolve the extended emission from the surrounding environment. These differences make it difficult to correctly characterise the morphology of the extended radio sources and hinder the creation of reliable spectral index maps, since some of the structures present in the LoTSS are not detected to a similar extent in the TGSS.

The difference in sensitivities also had to be factored in since most of the sources have intensities below 0.1 Jy, which is the typical noise level for the Very Large Array (VLA) Low-frequency Sky Survey Redux (VLSSr). This sensitivity to sources with higher intensities leads to the much higher observed intensities in comparison to the other surveys. With these restrictions in mind, we opted to use the LoTSS survey in conjunction with

the NVSS survey to characterise the morphology of the extended sources and create spectral index maps, since both surveys can resolve extended sources very well. However, the resolutions of the two surveys do not match, with the NVSS survey having a lower angular resolution at 45″ when compared to the higher angular resolution of 25″ for the LoTSS survey. This difference in resolutions then introduces some uncertainties pertaining to the alignment of the overlapping regions which is discussed in Chap. 4.1.4. To perform the integrated spectra analysis we used all of the surveys since they all are sensitive to compact structures.

In the following section we will briefly describe each one of the data sets used in our analysis referring to the available literature on the subject.

2.1 LOFAR Two-metre Sky Survey

The LOFAR Two-metre Sky Survey (LoTSS) carried out in the frequency range 120-168 MHz is a deep imaging survey that has been obtained using a compact core and long baselines of the LOFAR radio telescope network [68]. The compact core is made up of 24 core stations constructed in Exloo (a Village in the Netherlands) [3]. The long baselines consist of 14 remote stations spread around the Netherlands and 13 international stations distributed over Europe [3]. This design provides excellent sensitivity to both highly extended and compact emissions, producing images that are significantly more sensitive than those produced by any existing large-area low-frequency survey [68].

The survey covers an area over 350 square degrees, in the region of the HETDEX Spring Field (RA: $10^{\mathrm{h}}45^{\mathrm{m}}00^{\mathrm{s}}$ to $15^{\mathrm{h}}30^{\mathrm{m}}00^{\mathrm{s}}$ and DEC: $45°00'00''$ to $57°00'00''$) [68]. Within this area, our search was focused on the P7-Mosaic, an area of the sky between RA: $10^{\mathrm{h}}37^{\mathrm{m}}00^{\mathrm{s}}$ to $11^{\mathrm{h}}48^{\mathrm{m}}00^{\mathrm{s}}$ and DEC: $44°19'00''$ to $52°55'00''$. The P7-Mosaic was partitioned into smaller regions that covered 3 square degrees, to make it easier to survey the region for interesting extended radio sources. We had a particular interest in the region limited by RA: $10^{\mathrm{h}}50^{\mathrm{m}}00^{\mathrm{s}}$ to $11^{\mathrm{h}}35^{\mathrm{m}}00^{\mathrm{s}}$ and DEC: $45°00'00''$ to $52°00'00''$, where all the unidentified or poorly studied sources lie, since we noted initially the existence of the extended radio source PGC2285791 which was previously unknown.

The selection strategy used was semi-systematic and largely driven by heuristics. Specifically, we searched for low surface brightness $S_{\mathrm{SB}_{141\mathrm{MHz}}} < 160$ mJy/beam extended radio sources. To reduce the emission from bright compact sources, we sequentially clipped sources with radio brightness above 160, 120 and 80 mJy/pixel, then surveyed (by visual examination) the respective clipped mosaics and compared the results. Without most

of the compact bright sources in the field obscuring the views, we were able to identify the LoTSS extended radio sources listed in Tab. 3.1.

The products we used from the survey are the preliminary released images. These products were created using a fully-automated but direction-independent calibration strategy, observed at 141 MHz with a resolution of 25″ and typical noise levels of less than 0.5 mJy/beam [68]. Most of the following investigations were largely guided by observations from this survey, and all the other data were used as follow ups/complements to this imaging survey.

2.2 NRAO VLA Sky Survey

The NRAO Very Large Array (VLA) Sky Survey (NVSS) is a 1.4 GHz continuum survey with a compact core configuration, that was used to make 1.4 GHz continuum total-intensity and linear-polarization images [17]. The compact core consists of 27 radio telescopes arranged in D and DnC configurations of the VLA [17]. This compact core configuration is best suited for studying extended emission at 1.4 GHz. The products used from the survey have a resolution of 45″ and typical noise levels of less than 0.5 mJy/beam [17].

We used products from this survey to: study the extent of the diffuse emission, perform integrated spectra analysis, characterise the morphology and create spectral index maps of the extended radio sources in our sample.

2.3 TIFR GMRT Sky Survey

The TIFR GMRT Sky Survey (TGSS) is an imaging survey of the 150 MHz radio sky aimed at producing a reliable compact source survey [34]. Thirty radio telescopes are used, with fourteen telescopes arranged in a compact configuration and the outer telescopes in a "Y-shaped" configuration [34]. The products used from the survey have a resolution of 25″ and typical noise levels of less than 5 mJy/beam [34].

The products from this survey were used to perform integrated spectra analysis. We note that for most of the extended sources in our sample, the short integration is sufficient to produce images that exhibit extended features. However, in this study we are interested in the extended radio galaxy PGC2285791 and the short integration time could not map out the diffuse emission sufficiently.

We furthermore note that though the TGSS survey is the ideal match to the LoTSS survey (in terms of resolution), the data products from the image cutout service have fixed dimensions. Therefore, we could not alter the image dimensions for the purposes of our analysis. We also took into consideration that the two surveys are observed in a similar frequency range. With these challenges in mind, we opted for the use of the NVSS data products in order to create the spectral index maps that are discussed later on in this study.

2.4 Very Large Array Low-frequency Sky Survey

The Very Large Array (VLA) Low-frequency Sky Survey Redux (VLSSr) is an imaging survey which used the VLSS catalog as a sky model to correct for the ionospheric distortions in the data and then create a new set of sky maps and a corresponding catalog at 73.8 MHz [36]. The products used from the survey have a resolution of $75''$ and typical noise levels of less than 0.1 Jy/beam [36].

The products from this survey were used in performing the integrated spectra analysis for the extended radio sources.

Chapter 3

Data analysis techniques

In this chapter we will detail the procedure followed in studying and characterising the core, the extended structure and the environment of the selected radio sources.

The first section focuses on the difference between the field-of-view of a radio telescope (given in terms of [synthesized] beam sizes [1]) and that of the radio data analysis software (given in terms of pixel size) we used in our analysis.

This differentiation is crucial because in literature the surface brightness is normally stated in intensity/beam [2] (with the beam size being a fixed area under the synthesized beam), whereas radio data analysis software are constrained by the pixel size of an image, which is much smaller than the beam size.

To elaborate the subtle problems that may arise if this point is not taken into account, we will use a statement that will be mentioned in the sections that follow. We explain it in detail in this section so that the reader becomes cognisant of the caveats that lie within the statement when using the flux per pixel area conversion procedure we followed. The statement is quoted as follows "we initially excluded extended radio sources that were above x mJy per beam area". An experienced radio astronomer would understand this statement to mean that sources which had flux densities above x mJy when integrated over a specified beam area were initially excluded for a specified purpose. The problem then arises when one tries to say "we initially excluded extended radio sources that were

[1] The terms "field-of-view" and "beam" are equivalent for single dish antennas. However, for interferometric images the situation is quite different: the synthesized beam is in fact much smaller than the field-of-view (primary beam of the single antenna in the array). To avoid confusion, we use the term synthesized beam instead of field-of-view and reserve the field-of-view term to describe the size of the continuum images used from the different imaging surveys (see section 3.3).

[2] We use the term "surface brightness" to refer to the measured intensity (expressed in units of Jy/beam or Jy/pixel) while the term "flux density" is used to refer to the integral of the surface brightness over a given solid angle (expressed in units of Jy (W/Hz/m^2), which we refer to as "Jy per beam area" or "Jy per pixel area" or "Jy per extracted area" to draw a distinction between the expressed units).

above x mJy per pixel area". In this case the statement is looking at individual pixels which are much smaller than a specified beam area. This then necessitates a clear path to move from the mJy/pixel (synthesized beam of a radio data analysis software) to mJy/beam (synthesized beam of a radio telescope) analysis.

The second and third section then describe how we can carry out the data exploration procedure and the data analysis using the synthesized beam of a radio data analysis package.

3.1 Preparation and pre-analysis of Data

In the following explanation of our analysis, we use mJy/pixel in place of the expected mJy/beam as a unit of measurement. This is motivated by the tools used in this analysis and the fact that from an image perspective, pixels are what we can directly perform operations on and not beam sizes. We are then tasked with moving from pixel intensities (mJy/pixel) to the synthesized beam intensity (mJy/beam) and, finally, presenting the integrated flux density (mJy) by integrating over an area that is covered by a particular synthesized beam size.

This differentiation is necessary because when we apply thresholds, what we are effectively doing is masking out specified pixel intensities, which is not the same as masking out fixed areas that are covered by an expected beam size (see Fig. 3.1). And even though we can carry out the latter procedure in our data exploration context, the implementation is highly non-trivial and would require an extra amount of time that is deferred to a later study.

We, therefore, note that ideally we want to work in intensity/beam (not intensity/pixel) because this is the synthesized beam of a radio telescope and radio telescopes integrate the total flux of a source by integrating the intensity over the total solid angle that is subtended by the source. This then leads to two cases, where we integrate over an

- unresolved (point) source: If the antenna is pointing at a source with a very small size, the flux density that it measures is the brightness integrated over the entire source, i.e. the total flux density of the source. In this case, the integral is to be taken over the source.
- extended source: If the antenna is pointing at an extended source, part of which falls outside of the synthesized beam, it will measure only the flux from the source within the beam. In this case, the integral is to be taken over the beam size.

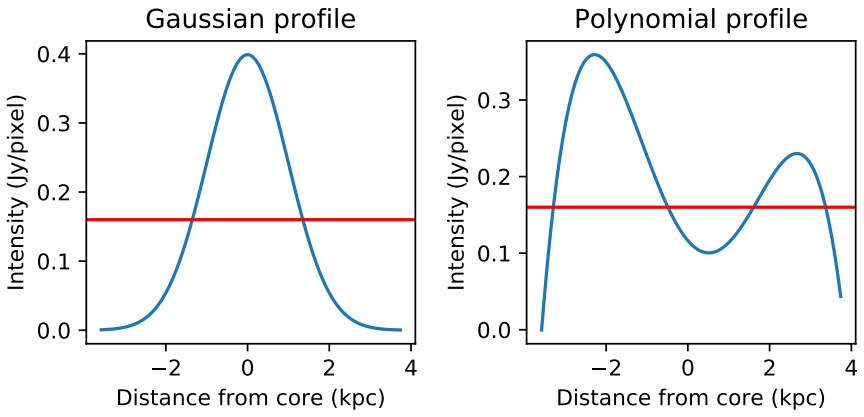


FIGURE 3.1: Source profile plots showing two possible source profiles. We display the red line to highlight the possible downside of using thresholds on sources with non-Gaussian profiles. The pixel masking and conversion procedure provides estimates to excluded sources since it simply cuts off pixel intensities and does not perform flux integration over the area above the threshold. This requires some human intervention to double check the excluded sources making it a less rigorous approach than using the dynamic flux per beam area procedure.

The necessary pseudo algorithm to do a flux per beam area procedure would be something along the lines:

- create arrays that match the different synthesized beam sizes of interests (i.e. 25, 45 and 75 arcseconds for the different surveys),
- dynamically scan through the different mosaics with these beam sizes and place each integrated value in an appropriate bin range for each beam size,
- once the above process is completed, colour the different bin ranges with designated colours,
- inspect data and fine tune to reach the appropriate sigma levels with careful treatment for noise and sources that are much smaller than the smallest beam size and
- exclude sources that are above a certain flux per beam area threshold.

The pseudo algorithm is deceptively hard to implement because: it does not take into account the memory management that is required when working with such large files, the optimisation needed to complete the analysis in reasonable time and the intensive computing requirements. So in the interest of time and feasibility, we opted to mask out pixel intensities and followed a flux per pixel area conversion procedure since it is trivial to implement whilst providing possible work arounds that bring us closer to achieving a flux per beam area analysis with the tools at our disposal. The downside of this chosen

path of analysis is: since we followed a flux per pixel area conversion procedure for our analysis rather than the expected flux per beam area procedure, we lose the ability to concretely say "we initially excluded extended radio sources that were above x mJy per beam area". To work around this we need to move from flux per pixel area to flux per beam area.

For us to carry out this conversion we first need to convert from the continuum FITS file unit, which is in intensity/beam, to flux per pixel area. We can achieve this by using the relation

$$S_\nu = S_{\mathrm{SB}} \times \Omega \ ,$$

where S_ν is the integrated radio flux density measured at the frequency ν, S_{SB} is the observed surface brightness at the frequency ν and Ω is the total solid angle that is subtended by the source, given by

$$\Omega = \frac{\pi\theta^2}{4\ln 2} \ ,$$

with θ being the angular extent of the region contained by the source in arcseconds, thus θ^2 gives us the total area covered by the source in arcseconds^2 [3]. The $4\ln 2$ factor assumes a Gaussian brightness profile. This then gives us that

$$\begin{aligned} \Omega_{\mathrm{pixel}} &= \frac{\pi\theta^2_{\mathrm{pixel}}}{4\ln 2} \\ \Omega_{\mathrm{beam}} &= \frac{\pi\theta^2_{\mathrm{beam}}}{4\ln 2} \quad . \end{aligned}$$

Therefore, if we have a FITS file from a radio telescope, measuring a single pixel value to be x mJy/beam, we can convert from intensity/beam to flux per pixel area as follows

$$\begin{aligned} S_\nu &= S_{\mathrm{SB}} \times \Omega_{\mathrm{pixel}} \\ &= x \ \frac{\mathrm{mJy}}{\mathrm{beam}} \times \Omega_{\mathrm{pixel}} \\ &= x \ \mathrm{mJy} \times \frac{\Omega_{\mathrm{pixel}}}{\Omega_{\mathrm{beam}}} \\ &= x \ \mathrm{mJy} \times \frac{\theta^2_{\mathrm{pixel}}}{\theta^2_{\mathrm{beam}}} \ . \end{aligned}$$

This then gives us the integrated flux density, S_ν, integrated over a single pixel area (flux per pixel area). We can then move on to finding the integrated flux density, integrated

[3] We use arcseconds as the unit of measurement for solid angles (instead of steradians) because the angular resolution, of the different surveys, is given in arcseconds and only the ratio between solid angles is considered in the following analysis.

over the synthesized beam area (flux per beam area) by the expression

$$x \times \frac{\text{mJy}}{\text{pixel}} \times \frac{\text{pixel}}{\text{beam}} ,$$

where pixel/beam is the number of pixels contained within the considered beam size, a value that can be obtained from radio data analysis software such as CASA, MIRIAD, etc.

We, therefore, can provide estimates (in terms of our analysis) to the troublesome statement "we initially excluded extended radio sources that were above x mJy per beam area". In our analysis this can only be done by assuming that the pixels contained within the beam size have the same pixel intensity. Apart from the area we are integrating over, this is the major difference between the flux per pixel area and flux per beam area analysis. In the flux per pixel area analysis, our calculated value provides a lower limit to the sources we would have excluded by applying the chosen threshold. Whereas with the dynamic flux per beam area analysis the calculated value would be more rigorous, because the value would take into account instances where the pixel intensities are not constant.

A concrete example would be the conversion used in applying the different thresholds. Using continuum images obtained from the LoTSS telescope operating at a frequency of 141.45 MHz with $\theta_{\text{beam}} = 25''$, an observed surface brightness of 160 mJy/beam over a single pixel would correspond to

$$\begin{aligned} S_{141\text{MHz}} &= S_{\text{SB}} \times \Omega_{\text{pixel}} \\ &= 160 \ \frac{\text{mJy}}{\text{beam}} \times \Omega_{\text{pixel}} \\ &= 160 \ \text{mJy} \times \frac{\Omega_{\text{pixel}}}{\Omega_{\text{beam}}} \\ &= 160 \ \text{mJy} \times \frac{\theta^2_{\text{pixel}}}{\theta^2_{\text{beam}}} \ . \end{aligned}$$

Using ds9, the area covered by a single pixel is calculated to be $\theta^2_{\text{pixel}} = 11.8336$ arcsec^2. We, therefore, have that the integrated flux density, $S_{141\text{MHz}}$, integrated over a single pixel area is calculated to be

$$\begin{aligned} S_\nu &= 160 \ \text{mJy} \times \frac{\theta^2_{\text{pixel}}}{\theta^2_{\text{beam}}} \\ &= 160 \times \frac{11.8336}{625} \times \text{mJy} \\ &= 3.03 \ \text{mJy} \ . \end{aligned}$$

Using CASA we have the number of pixels contained within the LoTSS beam size, which is 46 pixels. Hence, our estimated statement (driven by the above analysis) would read: "we initially excluded extended radio sources that were above 139.38 mJy per beam area". We note that this value is lower than the expected value of 160.00 mJy per beam area. A possible explanation we might offer for this lower value is: since we are using a circle (LoTSS beam size) to approximate the pixel intensities (which are squares), some of the pixels that only cut the outskirts of the integrating circle are approximated to be points that lie outside of the circle, leading to a lower number of pixels than the expected value.

The final caution we would add on this statement is: since the statement is based on an analysis we initially did not follow, it is bound to break (as mentioned before) due to the masking out of specific pixel intensities and not masking out fixed areas that are covered by an expected synthesized beam size. An implication that follows from this is that, when we unmask selected sources and integrate over each source's core, the unmasked core might have a greater integrated flux density. We can then use this information to make an informed guess in predicting whether a source will have an integrated flux density that will be above or below 139.38 mJy per beam area. We can infer this information by looking at the extent to which the sources core has masked out pixels. If the core we are integrating over has no masked out pixels, then it is safe to predict that the integrated flux density will be below 139.38 mJy per beam area. If the core we are integrating over has a large number of masked out pixels, then we can speculate that the integrated flux density might fall above 139.38 the mJy per beam area value.

In cases where we are integrating over a region that is larger than the beam and want to calculate the average flux density over that extracted region, we can divide the integrated flux density of the extracted region by the area that is covered by that region. For example, if we look at the northern lobe of the extended radio source PGC2285791 (see Fig. 3.2), which has an integrated flux density $S_{141\mathrm{MHz}} = 178.64$ mJy integrated over a rectangle with an area of 237.007×185.751 arcsec^2, then the average flux density over that extracted region is $S_{141\mathrm{MHz}}/A = 4.06$ μJy. For the southern lobe, $S_{141\mathrm{MHz}} = 111.62$ mJy integrated over a rectangle with an area of 257.248×184.749 arcsec^2, giving us an average flux density over that extracted region $S_{141\mathrm{MHz}}/A = 2.35$ μJy.

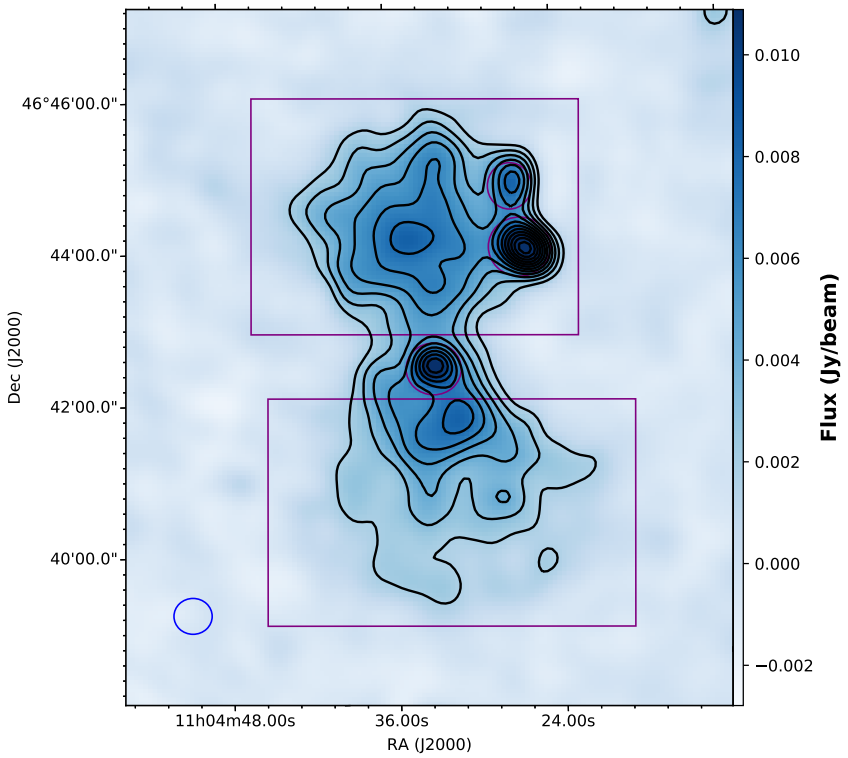


FIGURE 3.2: The LoTSS 141 MHz continuum image of PGC2285791 overlaid with black LoTSS contours starting at 3σ ($\sigma = 0.58$ mJy/beam) with 2σ increments. The purple regions highlight the different regions used in calculating the integrated spectra, for the northern and southern lobes and the two hotspots in the northern lobe. The beam size of the LoTSS is shown in the lower left corner.

We can repeat this analysis using the flux per pixel area conversion procedure. We can also check if our calculated value is feasible by integrating over the number of pixels contained within the rectangular area and seeing if it comes close to the calculated integrated flux density. CASA gives a mean of 2.78 mJy/pixel (value in terms of surface brightness/pixel). Converting this to the integrated flux density, $S_{141\mathrm{MHz}}$, integrated over a single pixel area we get a mean of 52.64 μJy (value in terms of flux per pixel area, using $\theta^2_{\mathrm{pixel}}$ as defined before). To check if this is a reasonable mean, we can calculate an approximate expected integrated flux density, integrated over the extracted area using the expression

$$52.64 \times \frac{\mu\mathrm{Jy}}{\mathrm{pixel}} \times \frac{\mathrm{pixel}}{\mathrm{area}}$$

with pixel/area = 3850. This gives us an expected integrated flux density, integrated over the extracted area of 202.51 mJy which is $\sim 12\%$ more than the actual value of 178.64 mJy. For the southern region we have 1.63 mJy/pixel, which translates to a mean of 30.82 μJy. With pixel/area = 4104, we expected an integrated flux density,

integrated over the extracted area of 126.49 mJy which is $\sim 12\%$ more than the actual value of 111.62 mJy.

3.2 Data exploration procedure

In mining radio astronomy images for extended radio sources, one of the major challenges we face are bright radio point sources. The challenge they introduce was made apparent when we initially surveyed (by visual inspection) the mosaics from the LoTSS catalogue (this holds for other catalogues from the different radio surveys); we noted that:

- most of the bright point sources emit well above 200 mJy/pixel,
- the diffuse emission we are interested in studying is typically radiated below 80 mJy/pixel and
- most images (from the different radio surveys) have noise levels that are typically at 5 mJy/pixel and even lower for modern telescopes, reaching levels of 0.5 mJy/pixel.

There is then a large difference between the maximum and minimum measurable light intensities. This high difference between maximum and minimum measurable light intensities makes it less obvious to see the "dim" diffuse emission we are interested in. Thus, one would typically expect to see images that are dominated by bright dots (corresponding to point radio sources) with a "uniformly" fluctuating background (corresponding to noise), and on rare occasions there are hints of shadows (corresponding to the extended radio sources we are interested in).

To reduce the large difference between the maximum and minimum measurable light intensities, we applied a mask to bright sources [4] (see Figs. 3.3 and 3.4, smaller cut outs from a larger mosaic). Once the mask was applied we then began to notice an increased amount of sources that are extended radio sources. Furthermore, these sources are now among the brightest sources, making it easier to detect sources with large diffuse emission.

We then found that even at the 160 mJy/pixel intensity threshold, there were still a sizeable number of point radio sources, so we further applied masking at different intervals until we got to the 80 mJy/pixel intensity threshold. At the 80 mJy/pixel intensity threshold most of the images were dominated by diffuse emission from the extended radio sources. We then looked for interesting sources in different mosaics and

[4] In this instance we are loosely categorising bright sources as sources that lie above the 160 mJy/pixel intensity threshold.

found that the P7-Mosaic (from LoTSS) was populated by a large variety of different and interesting extended radio sources. We then identified 15 extended radio sources from this mosaic for analysis, with the addition of PSZ2 G133.60+69.04[5] and A1304+4649A (which were taken from the P27-Mosaic, imaged at a frequency of 125.31 MHz).

We note that both the 139.38 and 160.00 mJy per beam area values (stated in the previous section) form a reasonable upper limit for the integrated flux densities of the extended radio sources, which are integrated over an area equal to the size of the LoTSS synthesized beam. The only exception to this quoted value is source A1304+4649A[6], with an integrated flux density of 446.02 mJy per beam area.

This source does not follow this limit because it was added on at a latter stage of the analysis carried out, and hence the generalisation should not apply to it. Furthermore, to clarify which sources were considered as original sources, we state that source 01 to 10 and IC 711 were the first sources considered for this analysis. Whilst carrying out some preliminary analysis on these initial sources, the remaining sources were found and added on to the list. Initially, source 10 was grouped with source 11 and 12 as a cluster. This grouping was separated based on the observed differences in the spectral index analysis and spatial separation of the sources. Source 13 and B31059+460-00 were added after the second iteration of the data exploration process as missed sources. The final two sources PSZ2 G133.60+69.04 and A1304+4649A are from the well known clusters A1550 and A1682, respectively.

[5]Extended radio source in the galaxy cluster A1550.
[6]Extended radio source in the galaxy cluster A1682.

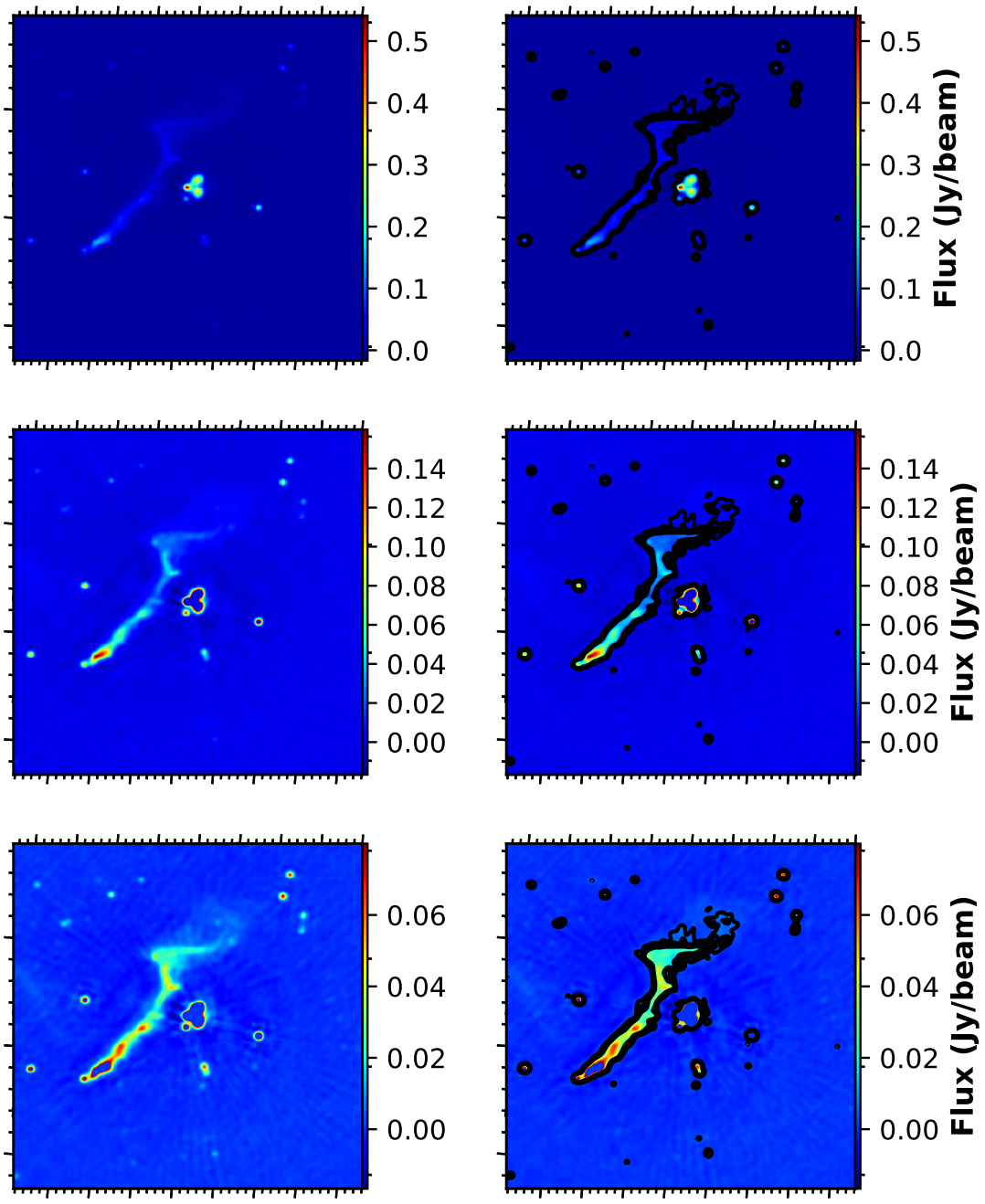


FIGURE 3.3: First row: the LoTSS 141 MHz continuum image of IC 711, shown without contours on the left and overlaid with black LoTSS contours on the right, starting at at 3σ ($\sigma = 1.31$ mJy/beam) with 2σ increments and ending at 14.41 mJy/beam. Second row: same images as the First row, with a mask applied to IC 711 at the 160 mJy/pixel intensity threshold to remove "bright" radio point sources and highlight the obscured diffuse emission we analyse in this study. Third row: same images as the First row, with a mask applied to IC 711 at the 80 mJy/pixel intensity threshold for the same purpose mentioned in the Second row.

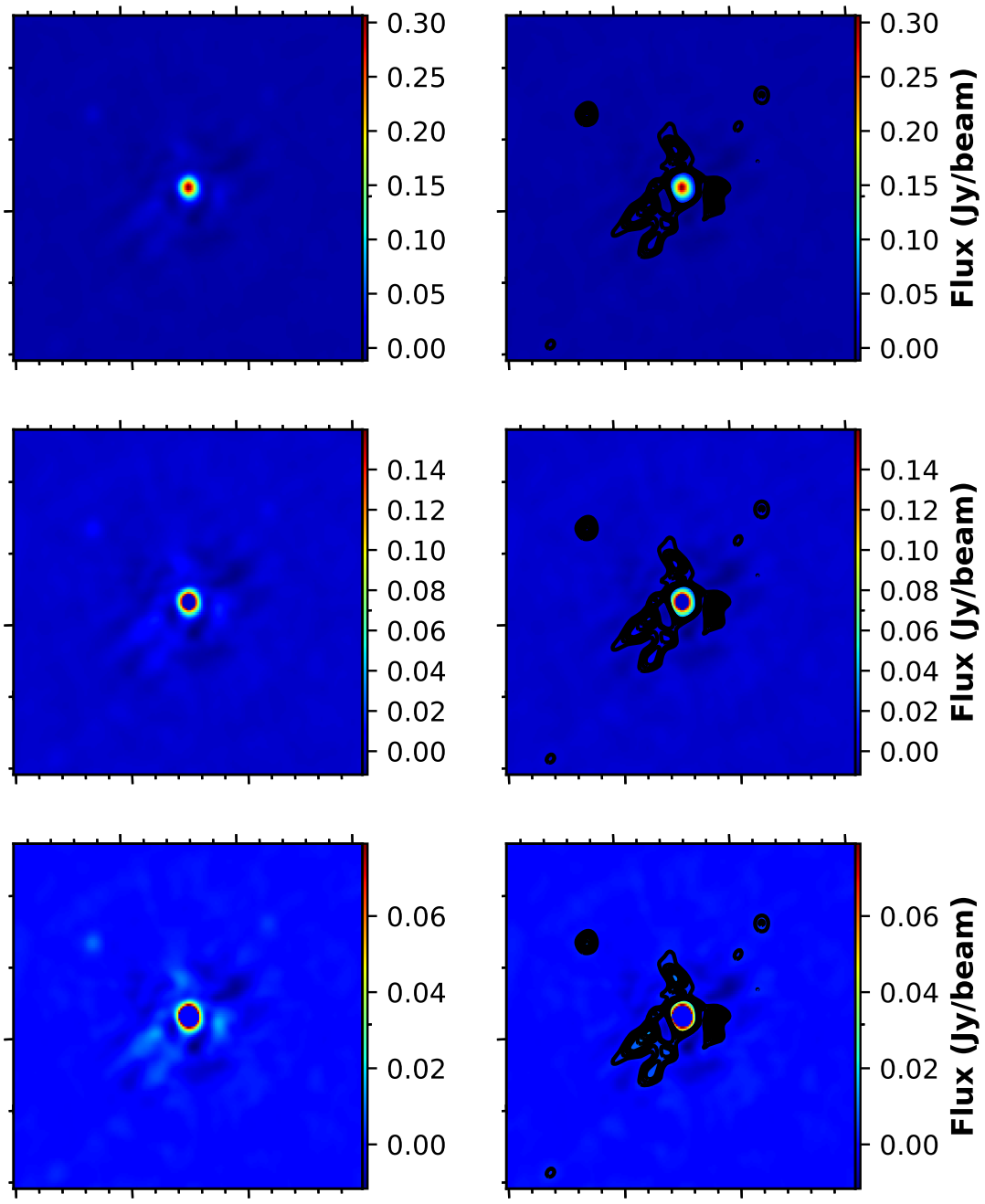


FIGURE 3.4: First row: The LoTSS 141 MHz continuum image of source 13, shown without contours on the left and overlaid with black LoTSS contours on the right, starting at 3σ ($\sigma = 0.81$ mJy/beam) with 2σ increments and ending at 15.39 mJy/beam. Second row: same images as the First row, with a mask applied to source 13 at the 160 mJy/pixel intensity threshold to remove "bright" radio point sources and highlight the obscured diffuse emission we analyse in this study. Third row: same images as the First row, with a mask applied to source 13 at the 80 mJy/pixel intensity threshold for the same purpose mentioned in the Second row.

3.3 Data analysis

The 17 identified extended radio sources that were selected using the data exploration procedure outlined earlier, are given in Tables 3.1, 3.2 and 3.3 (for the sake of comparison these tables are presented at the end of this section). Table 3.1 shows the integrated flux density values (of these extended radio sources) at the position of the core (as seen by LoTSS) for the different surveys, where we integrated over an area that is equal to the size of the LoTSS beam. To obtain these values, we used the regions option in CASA to make sure that the area we are integrating over is equal to the size of the LoTSS beam, see Fig. 3.5.

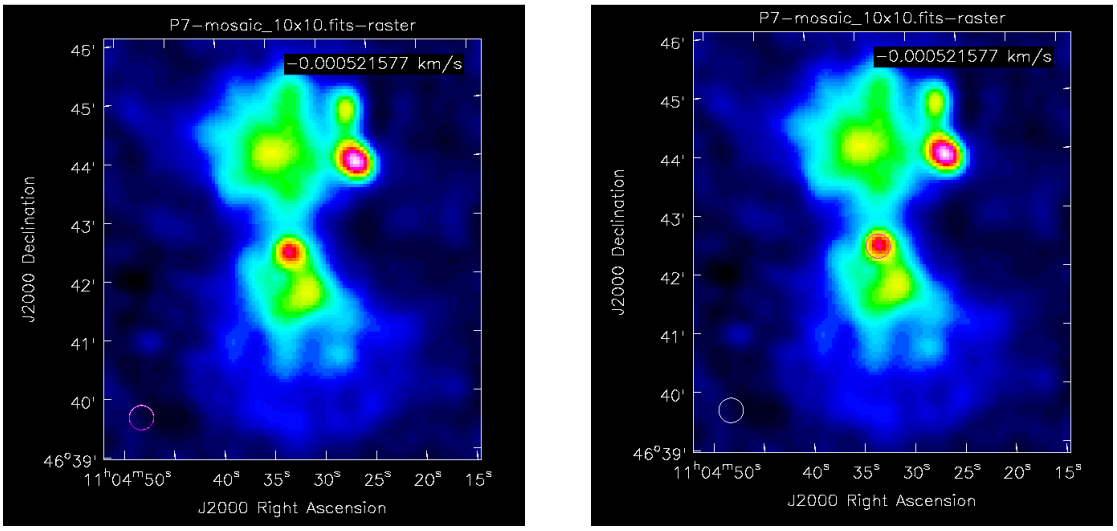


FIGURE 3.5: (Left) The LoTSS continuum image of PGC2285791 showing how the value we specified for the LoTSS beam (purple circle) in CASA matches with the default LoTSS beam (white circle). (Right) The same image with the LoTSS beam now placed over the area we integrated the flux density over (purple beam now centred at RA: 11h 04m 33.126s, DEC: 46°42′24.793″).

This step was repeated for all of the identified extended radio sources, using continuum images with a field-of-view of 10 arcminutes from the LoTSS, NVSS, TGSS and VLSSr imaging surveys. To ensure that we are integrating over the same area for all of these surveys (which have different pixel sizes), we used MIRIAD to regrid the continuum images from the NVSS, TGSS and VLSSr surveys to match the LoTSS survey image properties. The results obtained from this process are presented in Table 3.1 for the area equal to the size of the LoTSS beam, Table 3.2 for the area equal to the size of the NVSS beam and Table 3.3 for the area equal to the size of the VLSSr beam. The source names (in cases where the core of the source had no designated name, we named the source incrementally starting from Source 01) and positions of the extended radio sources along with the spectral indices calculated from the different surveys are also included in these tables.

To calculate the integrated flux density uncertainties we used the relation:

$$\sigma_{S_\nu} = \sqrt{(\sigma_{\rm cal} S_\nu)^2 + \left(\sigma_{\rm rms}\sqrt{N_{\rm beam}}\right)^2} \ ,$$

where $\sigma_{\rm cal}$ is the uncertainty in the calibration of the flux scale, S_ν is the integrated flux density at the observed frequency ν, $\sigma_{\rm rms}$ is the rms of the image and $N_{\rm beam}$ is the number of independent beams in the source [13]. Here, $\sigma_{\rm cal}$ is taken to be 10% for the LoTSS, NVSS and TGSS surveys [17, 34, 68] and 15% for the VLSSr survey [36].

The $\sigma_{\rm rms}$ was calculated for each source, using continuum images with a field-of-view of 10 arcmin for each survey. In cases where sources had weak detection signals, $\sigma_{\rm rms}$ was used to compute the 3σ upper limit for that respective survey (see Tables 3.1, 3.2, 3.3, and page 36 for comparisons of the 3σ upper limit values with the integrated flux density values).

Once we have obtained the integrated flux density of a radio source, we can calculate the radio source's spectral luminosity (provided we have the radio source's luminosity distance). For a cosmological model with $\Omega_{\rm k} = 0$, the luminosity distance, D_L, at redshift z is given by

$$D_L = \frac{c(1+z)}{H_0} \int \frac{dz}{\sqrt{(1+z)\zeta}}$$

with

$$\zeta = \sqrt{1 + \Omega_{\rm m} z + \Omega_\Lambda [1 - (1+z)^{-2}]} \ ,$$

where H_0 is the Hubble constant and $\Omega_{\rm m}$, Ω_Λ are the density parameters for matter and the cosmological constant, respectively [80].

In most cases where a source has an observed optical counterpart, we can obtain the source's spectroscopic information from a multi-spectral imaging and spectroscopic redshift survey such as the Sloan Digital Sky Survey (SDSS). We can then use the redshift from such surveys in the above equation to obtain D_L. Alternatively, we can query the NASA/IPAC Extragalactic Database (NED) and retrieve the luminosity distance from this database. This is the easier route to follow because one retrieves the D_L calculated value along with the parameters for distances and the adopted cosmology used, which are stated as $H_0 = 73.0$, $\Omega_{\rm m} = 0.27$, and $\Omega_\Lambda = 0.73$ with the derived quantities using a redshift corrected to a reference frame defined by the 3K CMB. This is the cosmology we adopt in this analysis.

The spectral luminosity L_ν of a source is defined as the total power per unit bandwidth radiated by the source at frequency ν, its mks units are W Hz^{-1}. The inverse-square law relation between spectral luminosity and flux density in free space is

$$L_\nu = 4\pi D_L^2 S_\nu \ ,$$

where the distance (luminosity distance) D_L between the source and the observer is much larger than the dimensions of the source itself [56].

From the mks units of the spectral luminosity (W Hz^{-1}), we can easily see that the spectral luminosity gives us a measurement of how much energy (transferred per unit time) is produced by the source at the observed frequency. We would, therefore, expect different spectral luminosities at different frequencies. This allows us to plot the spectral energy distribution (SED) of a source at different frequencies. SEDs are energy plotted against some measure of the photon – frequency or wavelength. In our case we are interested in plotting νS_ν against ν.

Now to carry out an example of how to implement the above procedure, we will use the extended radio galaxy PGC2285791 and present our calculations which were based on the integrated flux density that was integrated over beam sizes corresponding to the LoTSS, NVSS and VLSSr beams. We will use the core radio flux density spectrum of this extended radio galaxy which is shown in Figs. 3.6, 3.7, 3.8 for the LoTSS, NVSS and VLSSr beam sizes (these figures are presented together with Figs. 3.9, 3.10, 3.11 at the end of this section for inter-comparisons between the spectrum and the SED of the source).

Considering the case where we are integrating over the integrated area equal to the size of the LoTSS beam, we find that:

$$\begin{aligned} S_{\mathrm{int_core(141MHz)}} &= 7.34 \pm 0.73 \text{ mJy} \\ S_{\mathrm{int_core(1.4GHz)}} &= 1.04 \pm 0.10 \text{ mJy} \ , \end{aligned}$$

where we are not considering the calculated 3σ upper limit, for both the TGSS and VLSSr surveys.

PGC2285791 has an optical spectrum, found in the SDSS DR13, where it is classified as a star-forming galaxy at redshift $z = 0.14126 \pm 0.00001$. Using the source's luminosity distance of 645 Mpc in the adopted cosmology, the radio luminosity of the LoTSS and

NVSS surveys is given by

$$\begin{aligned} L_\nu &= 4\pi D_L^2 S_\nu \\ L_{141\mathrm{MHz}} &= 4\pi D_L^2 S_{\mathrm{int_core(141MHz)}} \\ L_{1.4\mathrm{GHz}} &= 4\pi D_L^2 S_{\mathrm{int_core(1.4GHz)}} \ . \end{aligned}$$

By definition, we know that the mks units of flux density, $\mathrm{Wm^{-2}Hz^{-1}}$, are much too big for practical astronomical use, so smaller values are then defined as

$$1\mathrm{Jansky} = 1\mathrm{Jy} \equiv 10^{-26}\mathrm{W\ m^{-2}Hz^{-1}} \equiv 10^{-23}\mathrm{erg\ s^{-1}\ cm^{-2}Hz^{-1}}$$

in terms of the mks and cgi units, respectively. We, therefore, have

$$\begin{aligned} S_{\mathrm{int_core(141MHz)}} = 7.34 \pm 0.73 \times 10^{-3}\mathrm{Jy} &\equiv 7.34 \pm 0.73 \times 10^{-29}\ \mathrm{Wm^{-2}Hz^{-1}} \\ &\equiv 7.34 \pm 0.73 \times 10^{-26}\ \mathrm{erg\ s^{-1}cm^{-2}Hz^{-1}} \end{aligned}$$

$$\begin{aligned} S_{\mathrm{int_core(1.4GHz)}} = 1.04 \pm 0.10 \times 10^{-3}\mathrm{Jy} &\equiv 1.04 \pm 0.10 \times 10^{-29}\ \mathrm{Wm^{-2}Hz^{-1}} \\ &\equiv 1.04 \pm 0.10 \times 10^{-26}\ \mathrm{erg\ s^{-1}cm^{-2}Hz^{-1}}. \end{aligned}$$

Thus, the radio luminosity of the LoTSS and NVSS survey is

$$\begin{aligned} L_{141\mathrm{MHz}} &= 3.65 \times 10^{23}\ \mathrm{W\ Hz^{-1}} \\ L_{1.4\mathrm{GHz}} &= 0.52 \times 10^{23}\ \mathrm{W\ Hz^{-1}}\ . \end{aligned}$$

We then use $\nu \times S_\nu$ to obtain the SED of the source at the different frequencies and plot νS_ν against ν. The overall multi-ν SED of the radio galaxy core, derived from the combination of archival data and of the radio data obtained from this analysis, is shown in Fig. 3.9.

If we follow the same line of reasoning, it is easy to show that for the case where we are integrating over the integrated area equal to the size of the NVSS beam, we find that

$$\begin{aligned} L_{141\mathrm{MHz}} &= 8.64 \times 10^{23}\ \mathrm{W\ Hz^{-1}} \\ L_{1.4\mathrm{GHz}} &= 1.44 \times 10^{23}\ \mathrm{W\ Hz^{-1}} \end{aligned}$$

with the overall multi-ν SED shown in Fig. 3.10.

In the case where we are integrating over the integrated area equal to the size of the VLSSr beam, we find that

$$L_{141\mathrm{MHz}} = 18.23 \times 10^{23}\ \mathrm{W\ Hz^{-1}}$$
$$L_{1.4\mathrm{GHz}} = 3.25 \times 10^{23}\ \mathrm{W\ Hz^{-1}}$$

with the overall multi-ν SED presented in Fig. 3.11.

Source Name	R.A. (J2000)	Dec (J2000)	Integrated flux density (mJy) LoTSS 141 MHz	NVSS 1400 MHz	TGSS 150 MHz	VLLSR 73.8 MHz	Spectral index [a] α_{141}^{1400}	$\alpha_{73.8}^{141}$
(1)	(2)	(3)	(4)	(5)	(6)	(7)	(8)	(9)
Source 01	10 51 33	+50 12 49	23.71 ± 2.37	3.42 ± 0.34	16.22 ± 1.62	17.92[b] ± 2.69	-0.84 ± 0.06	0.43 ± 0.28
Source 02	11 00 41	+45 51 00	17.56 ± 1.76	0.88 ± 0.09	8.26 ± 0.83	23.82[b] ± 3.58	-1.31 ± 0.06	-0.47 ± 0.28
Source 03	11 03 39	+45 50 07	25.46 ± 2.55	1.97 ± 0.20	17.84 ± 1.79	29.96[b] ± 4.50	-1.12 ± 0.06	-0.25 ± 0.28
PGC2285791[c]	11 04 33	+46 42 24	7.34 ± 0.73	1.04 ± 0.10	7.47 [b] ± 0.75	19.76[b] ± 2.97	-0.85 ± 0.06	-1.52 ± 0.28
Source 05	11 08 05	+51 20 53	28.01 ± 2.80	0.36 [b] ± 0.04	23.10 ± 2.31	20.65[b] ± 3.10	-1.90 ± 0.06	0.47 ± 0.28
Source 06	11 08 15	+51 29 53	26.70 ± 2.67	1.10 ± 0.11	23.61 ± 2.36	21.07[b] ± 3.16	-1.39 ± 0.06	0.36 ± 0.28
Source 07	11 09 41	+44 58 28	14.69 ± 1.47	2.28 ± 0.23	9.35 [b] ± 0.94	20.31[b] ± 3.05	-0.81 ± 0.06	-0.50 ± 0.28
PGC2396883[d]	11 11 57	+51 36 22	16.80 ± 1.68	3.05 ± 0.31	11.47 [b] ± 1.15	21.45[b] ± 3.22	-0.74 ± 0.06	-0.38 ± 0.28
Source 09	11 27 10	+51 12 25	10.29 ± 1.03	1.22 ± 0.12	9.07 [b] ± 0.91	21.50[b] ± 3.23	-0.93 ± 0.06	-1.13 ± 0.28
Source 10	11 32 50	+50 57 05	12.52 ± 1.25	1.62 ± 0.16	11.27 ± 1.13	25.81[b] ± 3.88	-0.89 ± 0.06	-1.11 ± 0.28
Source 11[e]	11 32 47	+51 01 19	3.26 ± 0.33	0.41 ± 0.04	5.20 [b] ± 0.52	21.29[b] ± 3.20	-0.90 ± 0.06	-2.88 ± 0.28
Source 12	11 33 04	+51 04 26	8.79 ± 0.88	2.03 ± 0.20	4.50 [b] ± 0.45	21.05[b] ± 3.16	-0.64 ± 0.06	-1.34 ± 0.28
Source 13	11 01 29	+46 00 26	151.06 ± 15.11	1.03 ± 0.10	132.26 ± 13.23	53.65 ± 8.05	-2.18 ± 0.06	1.59 ± 0.28
B31059+460	11 02 49	+45 44 43	106.78 ± 10.68	9.30 ± 0.93	103.53 ± 10.35	48.16 ± 7.23	-1.06 ± 0.06	1.22 ± 0.28
PSZ2 G133.60+69.04[f]	12 28 53	+47 36 49	19.32 ± 1.93	0.34 [b] ± 0.03	15.40 ± 1.54	26.70 ± 4.01	-1.67 ± 0.06	-0.61 ± 0.34
A1304+4649A[g]	13 06 45	+46 33 33	446.02 ± 44.60	33.22 ± 3.32	470.90 ± 47.09	192.52 ± 28.88	-1.08 ± 0.06	1.59 ± 0.34
IC 711	11 34 46	+48 57 24	49.87 ± 4.99	10.63 ± 1.06	43.35 ± 4.34	29.42[b] ± 4.42	-0.67 ± 0.06	0.81 ± 0.28

TABLE 3.1: Data on the studied extended sources detected by *LoTSS*. Column (1): Radio source names; Column (2)-(3): Right Ascension (J2000) and Declination (J2000); Column (4)-(7): Integrated flux density at the position of the core (as seen by LoTSS) for the different surveys, integrated over an area equal to the size of the LoTSS beam; Column (8)-(9): Two-frequency radio spectral indices derived from the frequency of the survey bands given in Column (4)-(7).

[a]The convention, $S \propto \nu^{\alpha}$, was used to calculate the spectral index, where S is the radio flux density, ν is the frequency, and α is the spectral index.
[b]The calculated 3σ upper limit, from the respective survey, was used for instances where the radio survey provided a weak detection.
[c]Originally identified as Source 04 (see Chapter 4.2).
[d]Originally identified as Source 08 (see Chapter 4.2).
[e]Optical source with some extended emission features.
[f]Extended radio source in the galaxy cluster A1550 imaged at 125.31 MHz for the LoTSS survey.
[g]Extended radio source in the galaxy cluster A1682 imaged at 125.31 MHz for the LoTSS survey.

Source Name	R.A. (J2000)	Dec (J2000)	Integrated flux density (mJy) LoTSS 141 MHz	NVSS 1400 MHz	TGSS 150 MHz	VLLSR 73.8 MHz	Spectral index [a] α_{141}^{1400}	$\alpha_{73.8}^{141}$
(1)	(2)	(3)	(4)	(5)	(6)	(7)	(8)	(9)
Source 01	10 51 33	+50 12 49	59.95 ± 6.00	9.51 ± 0.95	39.09 ± 3.91	54.17[b] ± 8.13	-0.80 ± 0.06	0.16 ± 0.28
Source 02	11 00 41	+45 51 00	42.15 ± 4.22	2.46 ± 0.25	21.53 [b] ± 2.15	72.00[b] ± 10.80	-1.24 ± 0.06	-0.82 ± 0.28
Source 03	11 03 39	+45 50 07	59.68 ± 5.97	5.32 ± 0.53	42.22 ± 4.22	90.55[b] ± 13.59	-1.05 ± 0.06	-0.64 ± 0.28
PGC2285791[c]	11 04 33	+46 42 24	17.35 ± 1.73	2.90 ± 0.29	22.59 [b] ± 2.26	59.72[b] ± 8.96	-0.78 ± 0.06	-1.90 ± 0.28
Source 05	11 08 05	+51 20 53	67.53 ± 6.75	1.17 [b] ± 0.12	54.92 ± 5.49	62.43[b] ± 9.37	-1.77 ± 0.06	0.12 ± 0.28
Source 06	11 08 15	+51 29 53	59.59 ± 5.96	2.91 ± 0.29	51.43 ± 5.14	63.69[b] ± 9.55	-1.32 ± 0.06	-0.10 ± 0.28
Source 07	11 09 41	+44 58 28	38.19 ± 3.82	6.85 ± 0.69	28.25 [b] ± 2.83	61.39[b] ± 9.21	-0.75 ± 0.06	-0.73 ± 0.28
PGC2396883[d]	11 11 57	+51 36 22	43.42 ± 4.34	8.68 ± 0.87	34.68 [b] ± 3.47	64.85[b] ± 9.73	-0.70 ± 0.06	-0.62 ± 0.28
Source 09	11 27 10	+51 12 25	25.56 ± 2.56	3.30 ± 0.33	27.42 [b] ± 2.74	64.99[b] ± 9.75	-0.89 ± 0.06	-1.43 ± 0.28
Source 10	11 32 50	+50 57 05	31.09 ± 3.11	4.73 ± 0.47	25.72 ± 2.57	78.03[b] ± 11.71	-0.82 ± 0.06	-1.41 ± 0.28
Source 11[e]	11 32 47	+51 01 19	8.99 [b] ± 0.90	3.33 ± 0.33	15.71 [b] ± 1.57	64.36[b] ± 9.65	-0.43 ± 0.06	-3.02 ± 0.28
Source 12	11 33 04	+51 04 26	17.41 ± 1.74	5.48 ± 0.55	13.60 [b] ± 1.36	63.64[b] ± 9.55	-0.50 ± 0.06	-1.99 ± 0.28
Source 13	11 01 29	+46 00 26	290.43 ± 29.04	2.82 ± 0.28	250.84 ± 25.08	168.19 ± 25.23	-2.02 ± 0.06	0.84 ± 0.28
B31059+460	11 02 49	+45 44 43	234.04 ± 23.40	26.34 ± 2.63	222.46 ± 22.25	147.86 ± 22.18	-0.95 ± 0.06	0.71 ± 0.28
PSZ2 G133.60+69.04[f]	12 28 53	+47 36 49	62.55 ± 6.26	1.03 [b] ± 0.10	51.55 ± 5.16	83.27 ± 12.49	-1.70 ± 0.06	-0.54 ± 0.34
A1304+4649A[g]	13 06 45	+46 33 33	960.69 ± 96.07	88.79 ± 8.88	987.81 ± 98.78	594.57 ± 89.19	-0.99 ± 0.06	0.91 ± 0.34
IC 711	11 34 46	+48 57 24	108.38 ± 10.84	29.48 ± 2.95	89.28 ± 8.93	88.92[b] ± 13.34	-0.57 ± 0.06	0.30 ± 0.28

TABLE 3.2: Data on the studied extended sources detected by *LoTSS*. Column (1): Radio source names; Column (2)-(3): Right Ascension (J2000) and Declination (J2000); Column (4)-(7): Integrated flux density at the position of the core (as seen by LoTSS) for the different surveys, integrated over an area equal to the size of the NVSS beam; Column (8)-(9): Two-frequency radio spectral indices derived from the frequency of the survey bands given in Column (4)-(7).

[a]The convention, $S \propto \nu^{\alpha}$, was used to calculate the spectral index, where S is the radio flux density, ν is the frequency, and α is the spectral index.
[b]The calculated 3σ upper limit, from the respective survey, was used for instances where the radio survey provided a weak detection.
[c]Originally identified as Source 04 (see Chapter 4.2).
[d]Originally identified as Source 08 (see Chapter 4.2).
[e]Optical source with some extended emission features.
[f]Extended radio source in the galaxy cluster A1550 imaged at 125.31 MHz for the LoTSS survey.
[g]Extended radio source in the galaxy cluster A1682 imaged at 125.31 MHz for the LoTSS survey.

Source Name	R.A. (J2000)	Dec (J2000)	Integrated flux density (mJy) LoTSS 141 MHz	NVSS 1400 MHz	TGSS 150 MHz	VLLSR 73.8 MHz	Spectral index [a] α_{141}^{1400}	$\alpha_{73.8}^{141}$
(1)	(2)	(3)	(4)	(5)	(6)	(7)	(8)	(9)
Source 01	10 51 33	+50 12 49	112.66 ± 11.27	20.15 ± 2.01	67.21 ± 6.72	150.69[b] ± 22.60	-0.75 ± 0.06	-0.45 ± 0.28
Source 02	11 00 41	+45 51 00	67.40 ± 6.74	5.15 ± 0.51	59.90 [b] ± 5.99	200.31[b] ± 30.05	-1.12 ± 0.06	-1.67 ± 0.28
Source 03	11 03 39	+45 50 07	95.22 ± 9.52	9.93 ± 0.99	96.47 [b] ± 9.65	251.92[b] ± 37.79	-0.99 ± 0.06	-1.50 ± 0.28
PGC2285791[c]	11 04 33	+46 42 24	36.63 ± 3.66	6.54 ± 0.65	62.84 [b] ± 6.28	166.15[b] ± 24.92	-0.75 ± 0.06	-2.32 ± 0.28
Source 05	11 08 05	+51 20 53	107.98 ± 10.80	3.24 [b] ± 0.32	82.65 ± 8.26	173.67[b] ± 26.05	-1.53 ± 0.06	-0.73 ± 0.28
Source 06	11 08 15	+51 29 53	92.93 ± 9.29	5.75 ± 0.57	80.21 ± 8.02	177.17[b] ± 26.58	-1.21 ± 0.06	-0.99 ± 0.28
Source 07	11 09 41	+44 58 28	79.10 ± 7.91	15.03 ± 1.50	78.60 [b] ± 7.86	170.77[b] ± 25.62	-0.72 ± 0.06	-1.18 ± 0.28
PGC2396883[d]	11 11 57	+51 36 22	94.44 ± 9.44	19.34 ± 1.93	96.47 [b] ± 9.65	180.41[b] ± 27.06	-0.69 ± 0.06	-0.99 ± 0.28
Source 09	11 27 10	+51 12 25	43.35 ± 4.33	6.26 ± 0.63	76.29 [b] ± 7.63	180.81[b] ± 27.12	-0.84 ± 0.06	-2.19 ± 0.28
Source 10	11 32 50	+50 57 05	60.86 ± 6.09	9.43 ± 0.94	42.45 [b] ± 4.25	217.08[b] ± 32.56	-0.81 ± 0.06	-1.95 ± 0.28
Source 11[e]	11 32 47	+51 01 19	25.01 [b] ± 2.50	26.03 ± 2.60	43.71 [b] ± 4.37	179.04[b] ± 26.86	0.02 ± 0.06	-3.02 ± 0.28
Source 12	11 33 04	+51 04 26	23.70 ± 2.37	10.09 ± 1.01	37.83 [b] ± 3.78	177.05[b] ± 26.56	-0.37 ± 0.06	-3.09 ± 0.28
Source 13	11 01 29	+46 00 26	331.9 ± 33.19	4.84 ± 0.48	278.39 ± 27.84	393.60 ± 59.04	-1.84 ± 0.06	-0.26 ± 0.28
B31059+460	11 02 49	+45 44 43	341.64 ± 34.16	50.17 ± 5.02	321.64 ± 32.16	335.48 ± 50.32	-0.84 ± 0.06	0.03 ± 0.28
PSZ2 G133.60+69.04[f]	12 28 53	+47 36 49	154.61 ± 15.46	2.85 [b] ± 0.29	132.36 ± 13.24	219.88 [b] ± 32.98	-1.65 ± 0.06	-0.66 ± 0.34
A1304+4649A[g]	13 06 45	+46 33 33	1415.04 ± 141.5	157.63 ± 15.76	1393.49 ± 139.35	1421.41 ± 213.21	-0.91 ± 0.06	-0.01 ± 0.34
IC 711	11 34 46	+48 57 24	169.44 ± 16.94	60.82 ± 6.08	136.21 ± 13.62	247.36[b] ± 37.11	-0.45 ± 0.06	-0.58 ± 0.28

TABLE 3.3: Data on the studied extended sources detected by *LoTSS*. Column (1): Radio source names; Column (2)-(3): Right Ascension (J2000) and Declination (J2000); Column (4)-(7): Integrated flux density at the position of the core (as seen by LoTSS) for the different surveys, integrated over an area equal to the size of the VLSSr beam; Column (8)-(9): Two-frequency radio spectral indices derived from the frequency of the survey bands given in Column (4)-(7).

[a]The convention, $S \propto \nu^{\alpha}$, was used to calculate the spectral index, where S is the radio flux density, ν is the frequency, and α is the spectral index.
[b]The calculated 3σ upper limit, from the respective survey, was used for instances where the radio survey provided a weak detection.
[c]Originally identified as Source 04 (see Chapter 4.2).
[d]Originally identified as Source 08 (see Chapter 4.2).
[e]Optical source with some extended emission features.
[f]Extended radio source in the galaxy cluster A1550 imaged at 125.31 MHz for the LoTSS survey.
[g]Extended radio source in the galaxy cluster A1682 imaged at 125.31 MHz for the LoTSS survey.

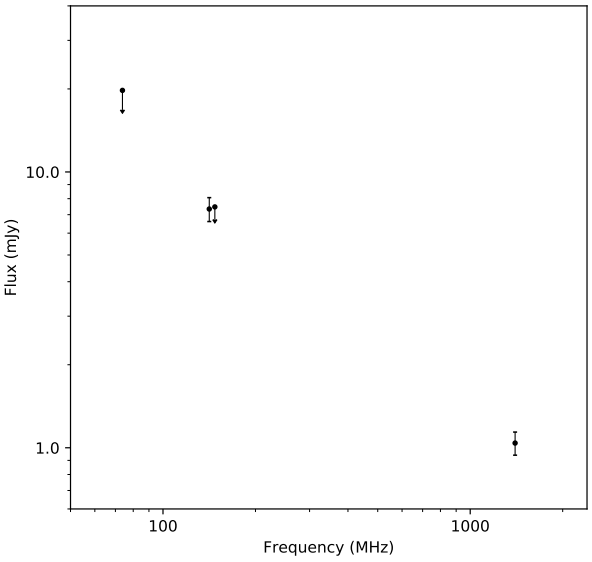


FIGURE 3.6:

The spectrum of the core of the radio galaxy PGC2285791 is shown for different frequencies, with the frequency-flux (MHz, mJy) pairs of: (73.79, 19.76)[a], (141.45, 7.34), (147.50, 7.47)[b]and (1400.00, 1.04), integrated over the LoTSS beam size.

[a]Calculated 3σ upper limit, for the VLSSr survey.

[b]Calculated 3σ upper limit, for the TGSS survey.

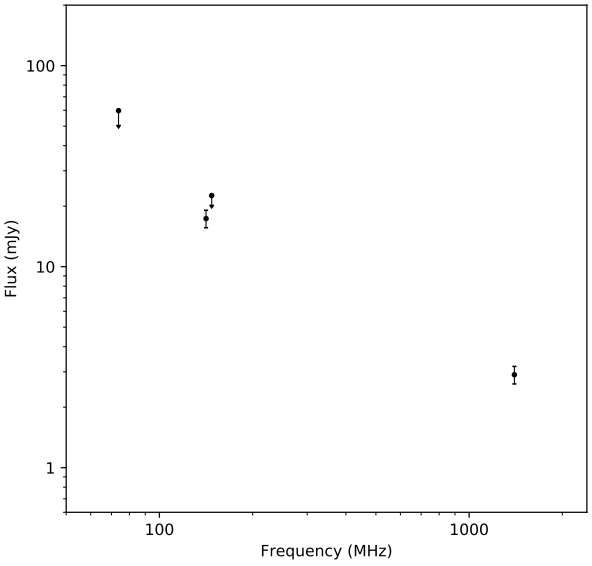


FIGURE 3.7:

The spectrum of the core of the radio galaxy PGC2285791 is shown for different frequencies, with the frequency-flux (MHz, mJy) pairs of: (73.79, 59.72)[a], (141.45, 17.35), (147.50, 22.59)[b]and (1400.00, 2.90), integrated over the NVSS beam size.

[a]Calculated 3σ upper limit, for the VLSSr survey.

[b]Calculated 3σ upper limit, for the TGSS survey.

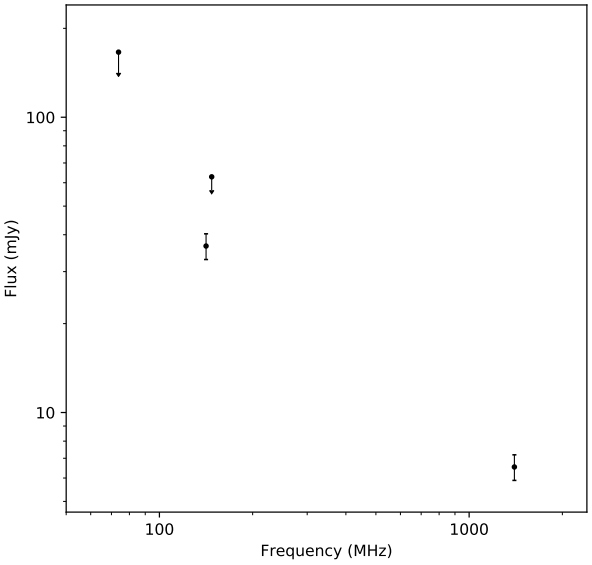


FIGURE 3.8:

The spectrum of the core of the radio galaxy PGC2285791 is shown for different frequencies, with the frequency-flux (MHz, mJy) pairs of: (73.79, 166.15)[a], (141.45, 36.63), (147.50, 62.84)[b]and (1400.00, 6.54), integrated over the VLSSr beam size.

[a]Calculated 3σ upper limit, for the VLSSr survey.

[b]Calculated 3σ upper limit, for the TGSS survey.

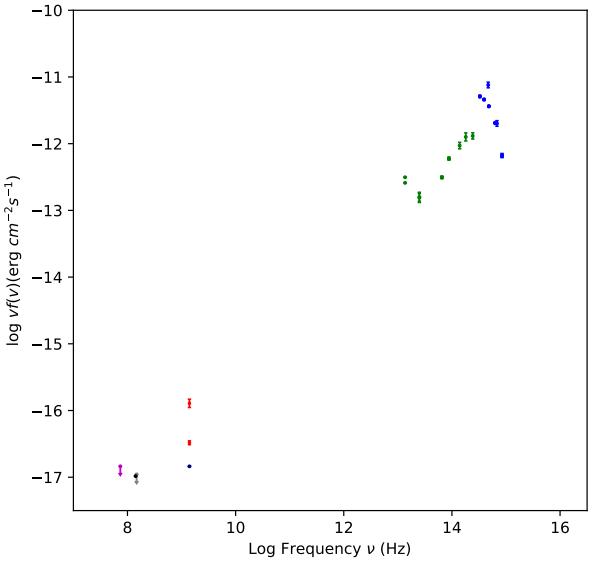


FIGURE 3.9: The SED of the core of the radio galaxy PGC2285791 with previously known optical (blue), infrared (green) and radio (red) data points plotted with the addition of the VLSSr (magenta), LoTSS (black), TGSS (grey overlaps with black) and NVSS (navy) data points, integrated over the LoTSS beam size.

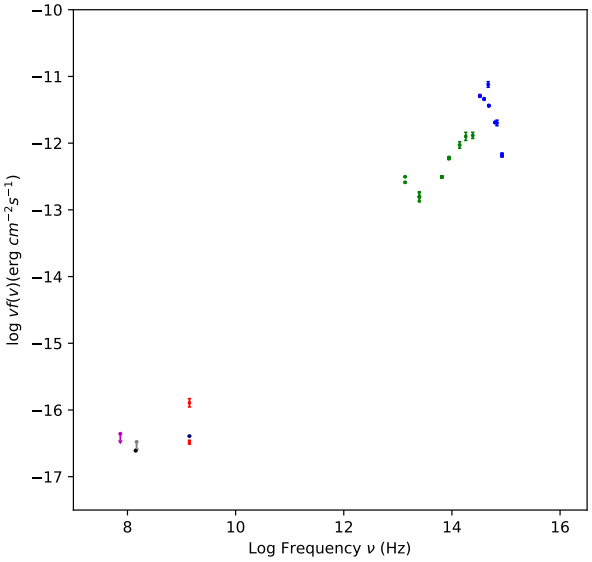


FIGURE 3.10: The SED of the core of the radio galaxy PGC2285791 with previously known optical (blue), infrared (green) and radio (red) data points plotted with the addition of the VLSSr (magenta), LoTSS (black), TGSS (grey) and NVSS (navy) data points, integrated over the TGSS beam size.

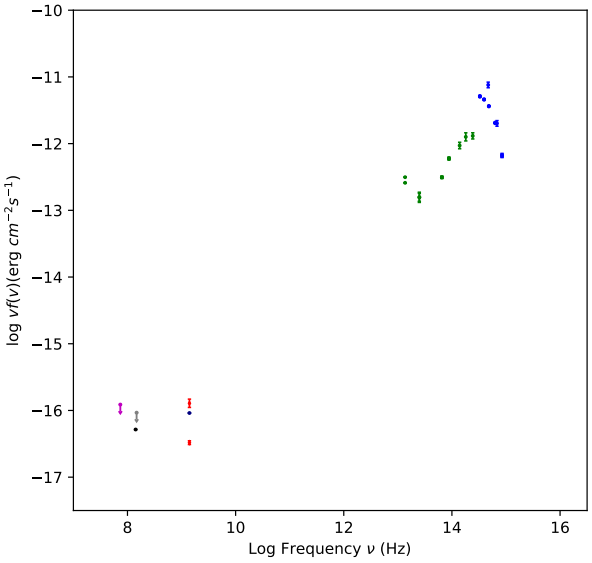


FIGURE 3.11: The SED of the core of the radio galaxy PGC2285791 with previously known optical (blue), infrared (green) and radio (red) data points plotted with the addition of the VLSSr (magenta), LoTSS (black), TGSS (grey) and NVSS (navy) data points, integrated over the VLSSr beam size.

```
# Using the LoTSS beam size
NVSS 25 beam    : source 05         The 3 sigma upper limit value is used : 0.359390814815 mJy compared to 0.2672587 mJy
                : source ABELL 1550 The 3 sigma upper limit value is used : 0.339405179259 mJy compared to 0.2812888 mJy

TGSS 25 beam    : source 04         The 3 sigma upper limit value is used : 7.4727763968   mJy compared to 6.939259 mJy
                : source 07         The 3 sigma upper limit value is used : 9.3472186368   mJy compared to 7.688507 mJy
                : source 08         The 3 sigma upper limit value is used : 11.4715865088  mJy compared to 7.694072 mJy
                : source 09         The 3 sigma upper limit value is used : 9.0723004416   mJy compared to 5.390177 mJy
                : source 11         The 3 sigma upper limit value is used : 5.1984531456   mJy compared to 2.041788 mJy
                : source 12         The 3 sigma upper limit value is used : 4.498661376    mJy compared to 2.929426 mJy

VLSSr 25 beam   : source 01         The 3 sigma upper limit value is used : 17.9196678144  mJy compared to 17.77602 mJy
                : source 02         The 3 sigma upper limit value is used : 23.8206896811  mJy compared to -0.173574 mJy
                : source 03         The 3 sigma upper limit value is used : 29.9577524224  mJy compared to 13.42863 mJy
                : source 04         The 3 sigma upper limit value is used : 19.7580096853  mJy compared to 4.451879 mJy
                : source 05         The 3 sigma upper limit value is used : 20.6521880576  mJy compared to 19.45251 mJy
                : source 06         The 3 sigma upper limit value is used : 21.0687307776  mJy compared to 14.8449 mJy
                : source 07         The 3 sigma upper limit value is used : 20.3078460757  mJy compared to 1.563598 mJy
                : source 08         The 3 sigma upper limit value is used : 21.4547270315  mJy compared to 8.386644 mJy
                : source 09         The 3 sigma upper limit value is used : 21.5019352064  mJy compared to 7.208908 mJy
                : source 10         The 3 sigma upper limit value is used : 25.8145408341  mJy compared to 13.98591 mJy
                : source 11         The 3 sigma upper limit value is used : 21.2908868949  mJy compared to -12.85668 mJy
                : source 12         The 3 sigma upper limit value is used : 21.0548460203  mJy compared to 4.150627 mJy
                : source IC 711     The 3 sigma upper limit value is used : 29.4162468864  mJy compared to 22.57044 mJy

# Using the NVSS beam size :
LoTSS 45 beam   : source 11         The 3 sigma upper limit value is used : 8.9899385856   mJy compared to 6.200045 mJy

NVSS 45 beam    : source 05         The 3 sigma upper limit value is used : 1.16582874074  mJy compared to 0.7799895 mJy
                : source ABELL 1550 The 3 sigma upper limit value is used : 1.02592929185  mJy compared to 0.9022911 mJy

TGSS 45 beam    : source 02         The 3 sigma upper limit value is used : 21.530525184   mJy compared to 18.91082 mJy
                : source 04         The 3 sigma upper limit value is used : 22.5881650176  mJy compared to 16.27081 mJy
                : source 07         The 3 sigma upper limit value is used : 28.2540926976  mJy compared to 19.16481 mJy
                : source 08         The 3 sigma upper limit value is used : 34.6754774016  mJy compared to 18.15242 mJy
                : source 09         The 3 sigma upper limit value is used : 27.4230899712  mJy compared to 13.28301 mJy
                : source 11         The 3 sigma upper limit value is used : 15.7135060992  mJy compared to 5.247612 mJy
                : source 12         The 3 sigma upper limit value is used : 13.598226432   mJy compared to 6.292932 mJy

VLSSr 45 beam   : source 01         The 3 sigma upper limit value is used : 54.1662686208  mJy compared to 52.51603 mJy
                : source 02         The 3 sigma upper limit value is used : 72.0034483541  mJy compared to -2.735449 mJy
                : source 03         The 3 sigma upper limit value is used : 90.5541152768  mJy compared to 40.08272 mJy
                : source 04         The 3 sigma upper limit value is used : 59.7230747307  mJy compared to 12.12616 mJy
                : source 05         The 3 sigma upper limit value is used : 62.4259320832  mJy compared to 57.74135 mJy
                : source 06         The 3 sigma upper limit value is used : 63.6850271232  mJy compared to 43.77179 mJy
                : source 07         The 3 sigma upper limit value is used : 61.3850801835  mJy compared to 6.432035 mJy
                : source 08         The 3 sigma upper limit value is used : 64.8517885269  mJy compared to 26.3809 mJy
                : source 09         The 3 sigma upper limit value is used : 64.9944859648  mJy compared to 21.24962 mJy
                : source 10         The 3 sigma upper limit value is used : 78.0303166123  mJy compared to 44.63104 mJy
                : source 11         The 3 sigma upper limit value is used : 64.3565444779  mJy compared to -36.6447 mJy
                : source 12         The 3 sigma upper limit value is used : 63.6430572885  mJy compared to 11.49342 mJy
                : source IC 711     The 3 sigma upper limit value is used : 88.9172917248  mJy compared to 66.49808 mJy

# Using the VLSSr beam size :
LoTSS 75 beam   : source 11         The 3 sigma upper limit value is used : 25.009603584   mJy compared to 6.419303 mJy

NVSS 75 beam    : source 05         The 3 sigma upper limit value is used : 3.24328296296  mJy compared to 1.929581 mJy
                : source ABELL 1550 The 3 sigma upper limit value is used : 2.85408900741  mJy compared to 2.515082 mJy

TGSS 75 beam    : source 02         The 3 sigma upper limit value is used : 59.89694976    mJy compared to 26.12127 mJy
                : source 03         The 3 sigma upper limit value is used : 96.465613824   mJy compared to 72.25071 mJy
                : source 04         The 3 sigma upper limit value is used : 62.839256064   mJy compared to 32.46627 mJy
                : source 07         The 3 sigma upper limit value is used : 78.601611264   mJy compared to 35.44944 mJy
                : source 08         The 3 sigma upper limit value is used : 96.465613824   mJy compared to 38.21864 mJy
                : source 09         The 3 sigma upper limit value is used : 76.289799168   mJy compared to 19.38914 mJy
                : source 10         The 3 sigma upper limit value is used : 42.453276672   mJy compared to 38.32039 mJy
                : source 11         The 3 sigma upper limit value is used : 43.714265088   mJy compared to 8.346909 mJy
                : source 12         The 3 sigma upper limit value is used : 37.82965248    mJy compared to 6.800277 mJy

VLSSr 75 beam   : source 01         The 3 sigma upper limit value is used : 150.688115712  mJy compared to 126.9163 mJy
                : source 02         The 3 sigma upper limit value is used : 200.310345045  mJy compared to -16.55883 mJy
                : source 03         The 3 sigma upper limit value is used : 251.917463552  mJy compared to 90.64441 mJy
                : source 04         The 3 sigma upper limit value is used : 166.146899627  mJy compared to 24.74092 mJy
                : source 05         The 3 sigma upper limit value is used : 173.666126848  mJy compared to 138.5325 mJy
                : source 06         The 3 sigma upper limit value is used : 177.168872448  mJy compared to 106.0182 mJy
                : source 07         The 3 sigma upper limit value is used : 170.770523819  mJy compared to 24.69697 mJy
                : source 08         The 3 sigma upper limit value is used : 180.414750037  mJy compared to 77.22302 mJy
                : source 09         The 3 sigma upper limit value is used : 180.811727872  mJy compared to 48.52715 mJy
                : source 10         The 3 sigma upper limit value is used : 217.076820651  mJy compared to 106.7563 mJy
                : source 11         The 3 sigma upper limit value is used : 179.037003435  mJy compared to -77.46403 mJy
                : source 12         The 3 sigma upper limit value is used : 177.052114261  mJy compared to 21.3191 mJy
                : source ABELL 1550 The 3 sigma upper limit value is used : 219.879017131  mJy compared to 208.3048 mJy
                : source IC 711     The 3 sigma upper limit value is used : 247.363894272  mJy compared to 151.8734 mJy
```

Chapter 4

Extended sources

Our strategy for the deep search was to look for faint extended sources, since they would have not been picked up by previous studies. Hence, in our initial search we ignored sources that had LoTSS integrated flux density levels above 160 mJy per beam area, when integrated over an area the size of the LoTSS beam, and we considered sources that exhibit diffuse emission features. The sources found in our search are listed in Table 3.1 and the known information about them is presented in Section 4.2 along with the derived images.

We now discuss the nature of the specific source PGC2285791 which is an extended radio galaxy that is poorly known. We will present our analysis of the remaining radio sources in a forthcoming study.

4.1 Source PGC2285791

The source PGC2285791 (RA: $11^{\mathrm{h}}04^{\mathrm{m}}32^{\mathrm{s}}.99$; DEC: $+46°42'24.83''$) is seen as an extended radio source in the LoTSS (see Fig. 4.1). This source is, however, poorly characterised in the literature and it is listed as a radio galaxy source in [7, 52]. It is also identified as a low-redshift source with ultra-steep spectrum in [9]. This is the only available information for this source in the literature.

It is justified, therefore, to perform an extensive analysis of this extended radio source based on the LoTSS data.

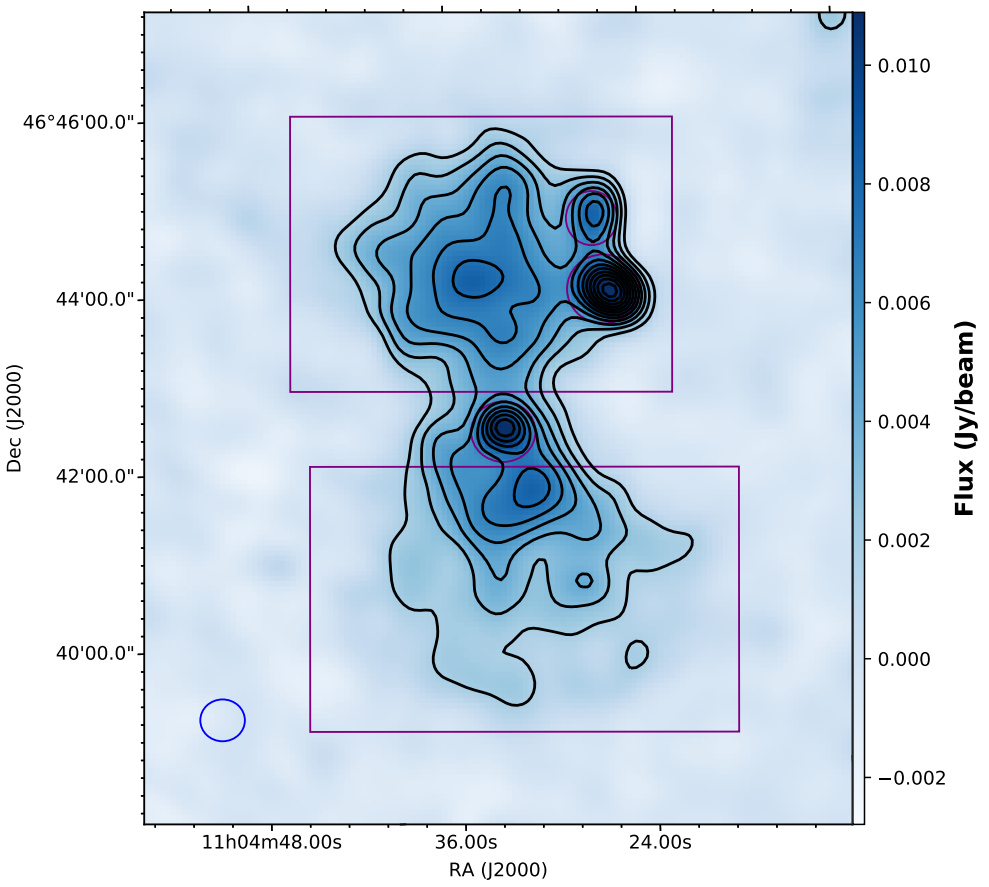


FIGURE 4.1: The LoTSS 141 MHz continuum image of PGC2285791 overlaid with black LoTSS contours starting at 3σ (σ = 0.58 mJy/beam) with 2σ increments. The purple regions highlight the different regions used in calculating the integrated spectra, for the northern and southern lobes and the two hotspots in the northern lobe. The beam size of the LoTSS is shown in the lower left corner.

4.1.1 Morphology

The radio image of PGC2285791 derived from the LoTSS at 141 MHz is shown in Fig. 4.1, and the NVSS image of the same source is shown in Fig. 4.2.

This radio galaxy has two diffuse bright lobes forming a double structure with average flux density of 52.58 μJy and 30.82 μJy for the northern and southern lobes, respectively. These lobes are quite irregular, at variance with typical lobes of powerful radiogalaxies connected by collimated jets. The source is also seen to have similar morphology at 1.4 GHz, as shown in Fig. 4.2. However, we notice that in the LoTSS image the core of the source is brighter and two additional compact sources (or knots) appear in the northern lobe. These two knots have LoTSS brightness levels of 136.83 $\pm$ 17.55 μJy and 254.94 $\pm$ 27.76 μJy for the top and bottom knots, respectively. The region of the northern lobe containing these radio knots has quite steep spectral index (see Fig. 4.7 and discussion in Section 4.1.4 below).

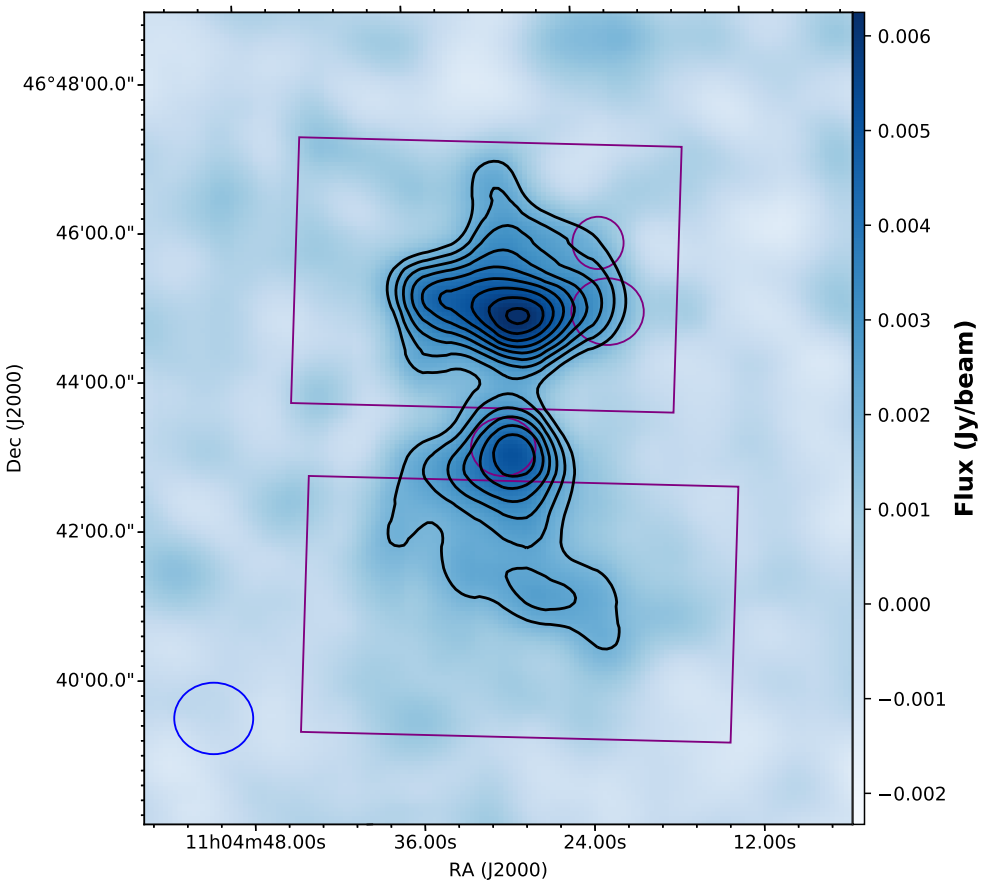


FIGURE 4.2: The NVSS continuum image of PGC2285791 overlaid with black NVSS contours starting at 3σ ($\sigma = 0.57$ mJy/beam) with 2σ increments. The purple regions highlight the different regions used in calculating the integrated spectra, for the northern and southern lobes and the two hotspots in the northern lobe. The beam size of the NVSS is shown in the lower left corner.

4.1.2 Integrated spectra

The integrated flux emitted by the core of PGC2285791 is $S_{\text{int_core(141MHz)}} = 7.34 \pm 0.73$ mJy and $S_{\text{int_core(1.4GHz)}} = 1.04 \pm 0.10$ mJy. Its radio luminosity is, therefore, $\text{L}_{141\text{MHz}} \sim 3.65 \times 10^{23}$ W Hz^{-1} and $\text{L}_{1.4\text{GHz}} \sim 0.52 \times 10^{23}$ W Hz^{-1}, derived using the source's luminosity distance of 645 Mpc in the adopted cosmology. The core radio flux density spectrum of the galaxy is shown in Fig. 4.3. We notice, however, that the spatial resolution of the four radio surveys from which we derived the core flux are quite different, with the VLSSr having the lowest resolution 75″ (the beam size is three times larger than the LoTSS beam), and the NVSS having a moderate resolution at 45″ (the beam size is 1.8 times larger than the LoTSS beam).

The integrated spectra of the northern and southern lobes are also shown in Fig. 4.4.

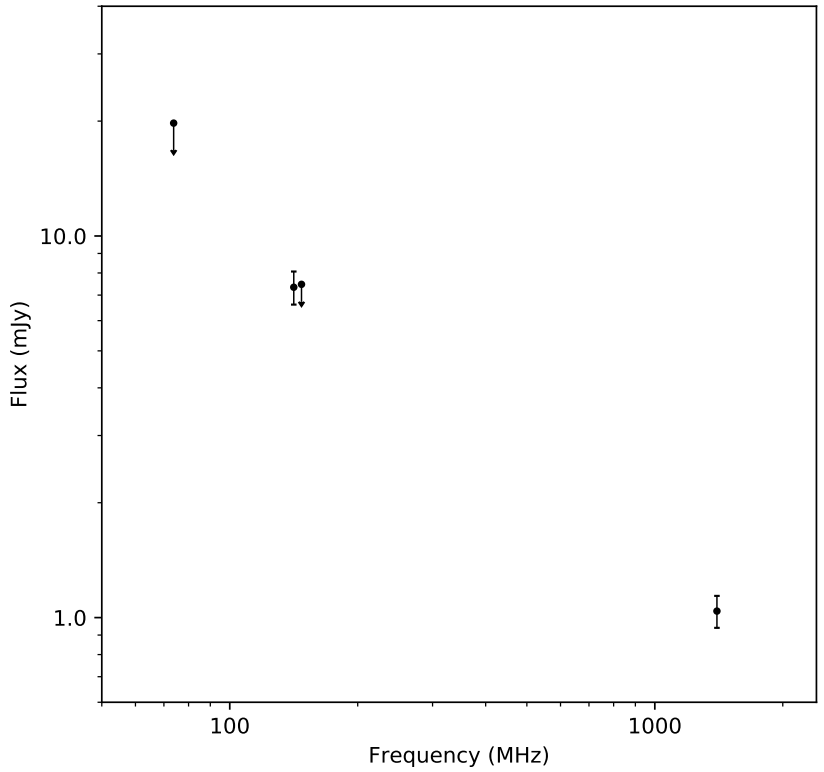


FIGURE 4.3:
The spectrum of the core of the radio galaxy PGC2285791 is shown for different frequencies, with the frequency-flux (MHz, mJy) pairs of: (73.79, 19.76)[a], (141.45, 7.34), (147.50, 7.47)[b]and (1400.00, 1.04), integrated over the LoTSS beam size.

[a]Calculated 3 σ upper limit, for the VLSSr survey.
[b]Calculated 3 σ upper limit, for the TGSS survey.

The two knots have an integrated flux of $S_{\text{int_nk(141MHz)}} = 6.33 \pm 0.63$ mJy and $S_{\text{int_nk(1.4GHz)}} = 0.54 \pm 0.05$[1] mJy for the northern knot, and $S_{\text{int_sk(141MHz)}} = 20.73 \pm 2.07$ mJy and $S_{\text{int_sk(1.4GHz)}} = 1.59 \pm 0.16$ mJy for the southern knot, integrated over the respective extracted areas shown in Fig. 4.1 and 4.2.

[1]Calculated 3 σ upper limit.

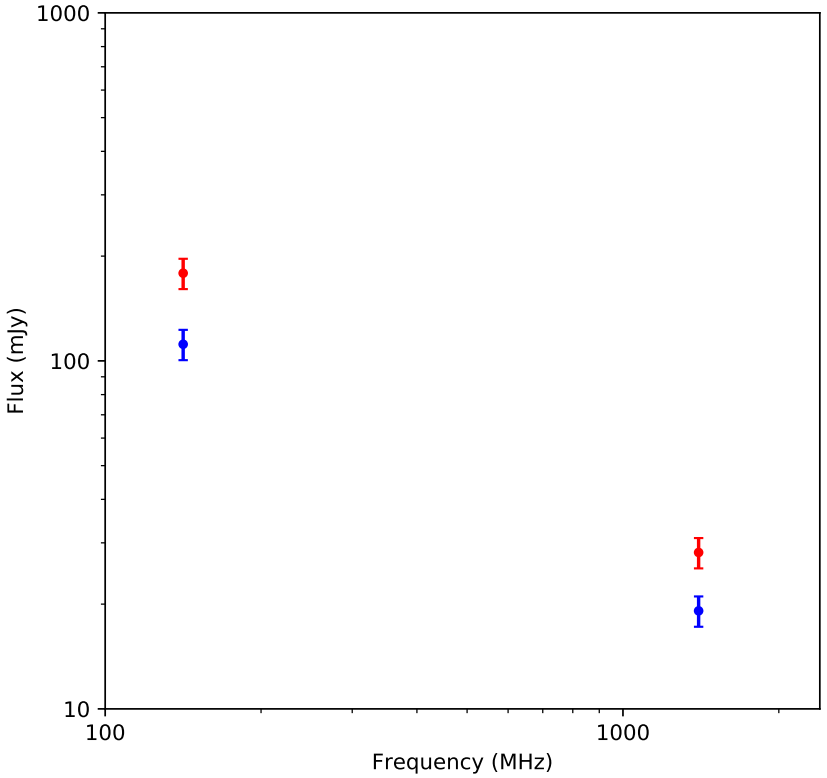


FIGURE 4.4: The integrated spectra of the northern and southern lobes at the LoTSS and NVSS frequencies for the radio galaxy PGC2285791: the red frequency-flux (MHz, mJy) pairs for the northern lobe are (141.45, 178.64) and (1400.00, 28.15); the blue frequency-flux pairs for the southern lobe are (141.45, 111.62) and (1400.00, 19.13).

4.1.3 Multi-ν analysis

The core of the radio source PGC2285791 is coincident with an optical and infrared source (IR) in the ESO-DSS-2-Red and WISE images, respectively (see Fig. 4.5). This optical source is extended and has the appearance of a galaxy. The galaxy nature of this source is confirmed by the image and the spectrum of the source as found in the SDSS DR13, where it is classified as a star-forming galaxy at redshift $z = 0.14126 \pm 0.00001$. The source is also associated with a QORG in the SSDC Sky Explorer tool [2] denoting its radio galaxy nature.

It is also interesting to notice the presence of two optical sources contained in the northern lobe (highlighted by blue squares in Fig. 4.5). They have confirmed spectra from SDSS DR13, with the top source being identified as a galaxy at $z = 0.11452 \pm 0.00003$ and the bottom source identified as PGC2286197, an AGN galaxy at $z = 0.11451 \pm 0.00003$ with a FIRST radio source in the SSDC Sky Explorer. Even though these two sources are at a comparable redshift to PGC2285791, they appear to be projections that are not

[2] `https://tools.asdc.asi.it/index.jsp`

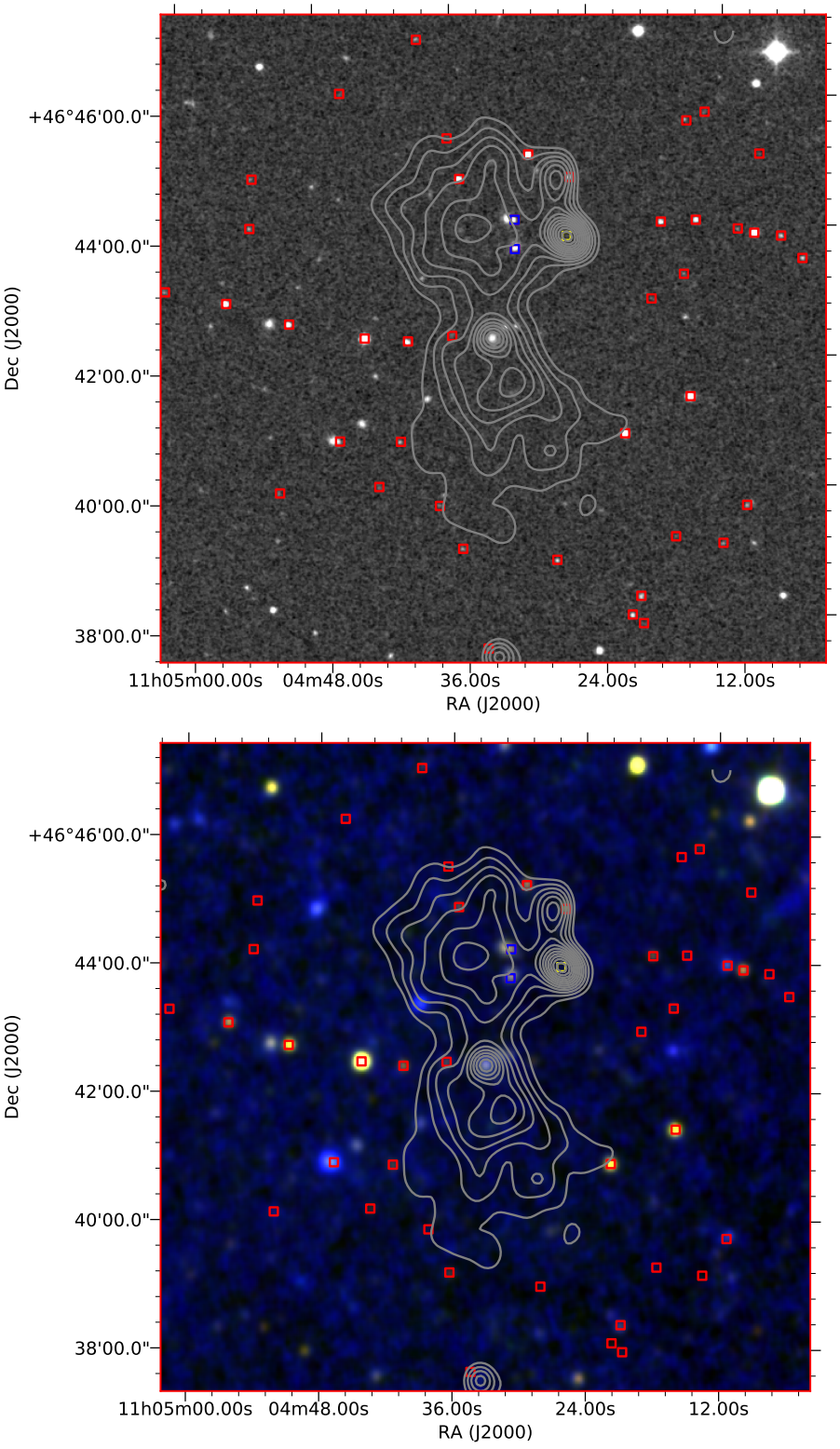


FIGURE 4.5: Top: background ESO-DSS-2-Red image of PGC2285791 overlaid with gray LoTSS contours at [1.74, 3.48, 5.22, 6.96, 8.7, 10.44, 12.18, 13.92, 15.66] mJy/beam. Bottom: background WISE image (rgb image from bands W1, W2 and W3) of PGC2285791 overlaid with gray LoTSS contours having the same contour properties as the top image. The red and blue overlaid squares are sources from the Gaia-DR1 pulled from the cross-correlation tool Aladin [8, 26]. The yellow square indicates the position of the hotspot and its possible optical counterpart.

interacting with PGC2285791.

The bottom knot is associated with a star in the SDSS DR13 (see yellow square in Fig. 4.5 with RA: 11h 04m 26.30s; DEC: $+46°43'57.72''$), and an IR counterpart is not visible from the WISE data. No optical or IR source is found at the position of the top radio knot; we will discuss the spectral behaviour of these two knots in Section 4.1.4 below.

The overall multi-ν spectral energy distribution (SED) of the radio galaxy core, obtained from the combination of archival data and of the radio data obtained from this study, is shown in Fig. 4.6.

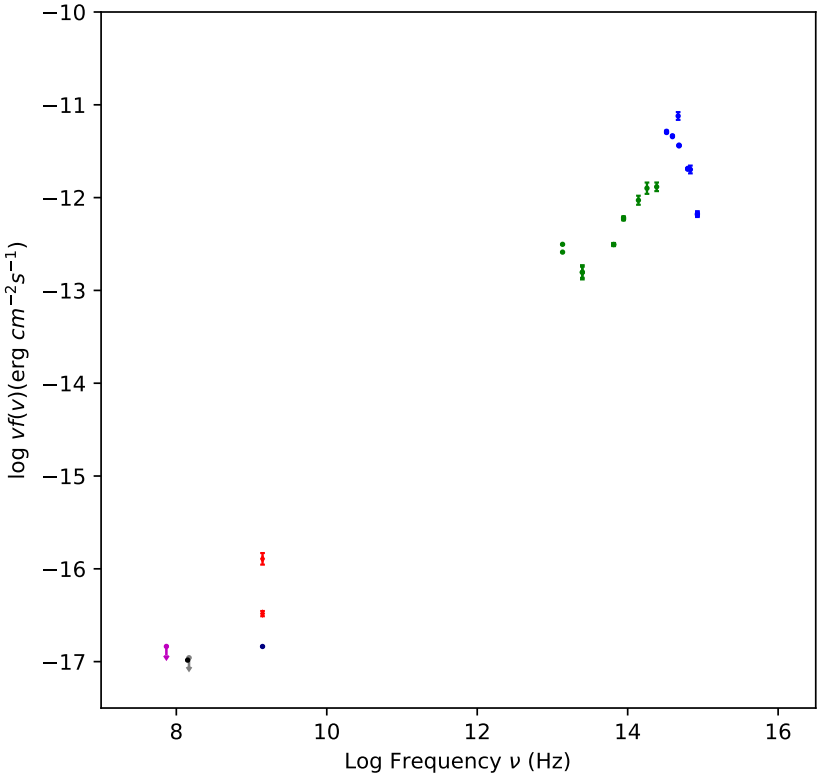


FIGURE 4.6: The SED of the core of the radio galaxy PGC2285791 with previously known optical (blue), infrared (green) and radio (red) data points plotted with the addition of the VLSSr (magenta), LoTSS (black), TGSS (grey overlaps with black) and NVSS (navy) data points.

The SED of this galaxy is clearly dominated by non-thermal emission at low frequencies while it is dominated by the integrated galaxy emission in the IR and Optical frequency range peaking at $\sim 5 \times 10^{14}$ Hz, which is quite typical of radio galaxy spectra. The lack of high frequency data in the soft and hard X-ray wavelength ranges do not allow yet to test the inverse Compton (on synchrotron) branch of the core emission. X-ray data would also identify possible inverse Compton scattering X-ray emission from the radio galaxy lobes.

4.1.4 Spectral index map

In order to produce spectral index maps, we aligned the images using the *regrid* task in MIRIAD [61]. The higher resolution LoTSS images were smoothed to the lower resolution NVSS images using a Gaussian beam with beam parameters (major="45 arcsec", minor="45 arcsec" and pa="0 deg") in MIRIAD.

We then derived the flux densities, from each matching pixel coordinate, obtained from the two images at different frequencies ($S_{141\mathrm{MHz}}$ and $S_{1.4\mathrm{GHz}}$) in order to calculate the spectral index at the corresponding point. The following power-law form of the spectral index formula was used: $S \propto \nu^{\alpha}$, where S is the radio flux density, ν is the frequency, and α is the spectral index.

The uncertainties were computed using the relation:

$$\sigma_{\alpha} = \frac{\sqrt{\left(\frac{\sigma_1}{S_1}\right)^2 + \left(\frac{\sigma_2}{S_2}\right)^2}}{\ln\left(\frac{\nu_1}{\nu_2}\right)} ,$$

where σ_1, σ_2 are the uncertainties of the LoTSS and NVSS flux densities, S_1, S_2 are the integrated flux densities at the LoTSS and NVSS frequency bands (ν_1, ν_2), respectively.

The resulting image array was then imaged in python using Matplotlib and APLpy, the derived maps are presented in Fig. 4.7. As we previously cautioned, the lack of access to raw data is a limiting factor and hence our resulting images have not been corrected for direction dependent effects, which we will leave to the LoTSS survey team to carry out as part of a future proposed data release.

A two-frequency radio spectral index image was computed from the maps at 141 MHz and 1.4 GHz. The distribution of the radio spectral index α is shown in Fig. 4.7 (a) and 4.7 (b), along with the spectral index error map in Fig. 4.7 (c). The spectral index of the extended radio source PGC2285791 varies from $\alpha = -1.1$ to $\alpha = -0.5$. While the southern radio lobe shows flat spectra with an average value of $\alpha = -0.7$, the emission of the northern lobe has an island of spectral index values that flattens up to $\alpha = -0.6 \pm 0.06$ surrounded by a steeper spectral region including the two radio knots $\alpha = -1.1 \pm 0.06$ towards the N-E boundary of the lobe. The derived spectral index values are $\alpha_{\mathrm{nk}} = -1.07 \pm 0.06$ and $\alpha_{\mathrm{sk}} = -1.12 \pm 0.06$ for the northern and southern knot, respectively. The spectral index map of the northern lobe indicates the presence of external regions with steep spectra ($\alpha \sim -1.1 \div -0.9$) which are encasing an inner region with much flatter spectra distribution ($\alpha \sim -0.8 \div -0.6$). The southern lobe seems to have a similar structure: the steep spectral index region ($\alpha \sim -1.0 \div -0.9$) is

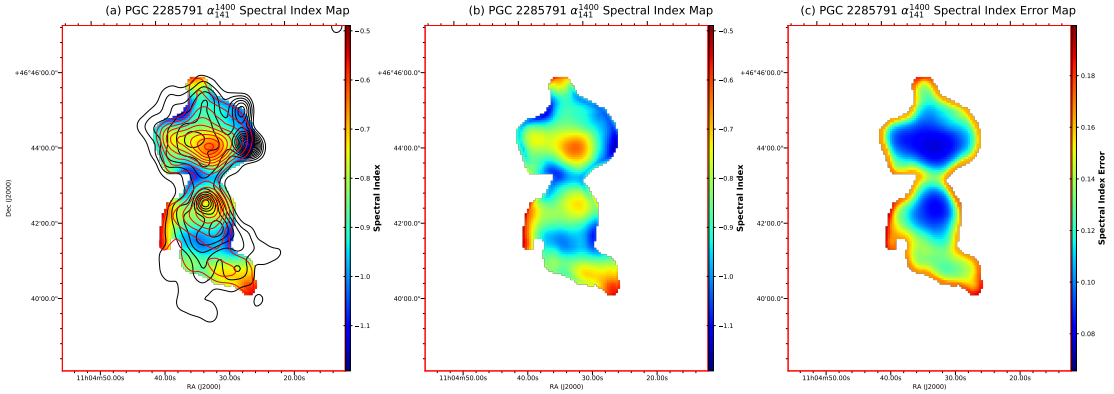


FIGURE 4.7: Spectral index maps of PGC2285791 computed from the LoTSS and NVSS maps at 141 MHz and 1.4 GHz, respectively. In the creation of the spectral index maps we clipped signals that were less than 3 times the respective rms noise. (a): spectral index map derived from the LoTSS beam smoothed to match the resolution of the NVSS beam and the NVSS beam overlaid with LoTSS contours (black) and NVSS contours (red) to show the source steepening. (b): The same spectral index map as (a). (c): spectral index error map of (a).

intermediate between the radio galaxy core and the flatter spectral indices ($\alpha \sim -0.8 \div -0.7$) region in the outer parts of the lobe. The spectral index distribution of the radio core is relatively steep ($\alpha \sim -0.8 \div -0.7$) justifying the decrease of its flux observed from 141 MHz to 1.4 GHz.

We note that there are uncertainties in the estimate of the spectral index due to differences in the (u, v) coverage between the two observations; the spectral index error map is shown in Fig. 4.7 (c), and the errors increase slightly towards the edges of the image but are still at a level $< 18\%$.

4.1.5 Discussion

The LoTSS observations combined with other low-frequency observations have raised a number of questions regarding the nature and origin of several sources in the HETDEX Spring Field. In this section we will discuss the result of PGC2285791 as the main interest of this dissertation.

Our analysis of the spectral index map, see Fig. 4.7 (b), shows a core surrounded by an older plasma which is enclosed by a younger plasma suggesting interaction and re-acceleration before reaching the termination point (in the northern flattest island). The youngest plasma is found near the outer lobe edges. The flattest island in the spectral index distribution of the northern lobe suggests the presence of a hotspot at the end of the lobe, while a similar feature is not visible in the southern lobe perhaps due to artefacts. The bilaterally symmetric bubble-like morphology, see Fig. 4.1, about an axis

through the core and spectral index distribution of the source suggest an outflow driven by a central engine.

The spectral-index variation in the northern blob, in fact, suggests a two-stage outflow scenario: initial outflow filling the blob with relativistic particles that is prominent at the time of the core's maximum activity, and a sign of later stage outflow possibly powered by collimated outflow. Possible interpretations of the spectral-index variation could be density and magnetic field enhancement due to shock compression by external plasma. Bubble-like radio structures have been observed in a few radio galaxies (e.g., Centaurus A [55]) and also in a number of Seyfert and starburst galaxies without obvious jets (e.g., NGC 6764 [20], Markarian [46], NGC 3079 [21, 65]). There is also a similarity in the radio structure of PGC2285791 with the LOFAR remnant radio galaxy B2 0924+30 [69] though the latter lacks a prominent radio core.

Several mechanisms have been suggested for the formation of bubble-like structures in these galaxies. A jet-driven outflow [cf. 55] and interaction of starburst wind with ISM are among them [e.g., 74]. In the case of PGC228579 the radio jet close to the nucleus possibly could give rise to the bubbles of non-thermal radio emission that would interact with the external environment (shock) in the host galaxy.

In the following section we present the known information and derived images of the remaining extended radio sources in our sample without detailed discussions and analysis as this is still an on going project.

4.2 Other sources

We notice that most of the extended sources (11 out of 17) were not previously studied in detail:

- Source 01 has been classified as a flat-spectrum source [41], while it also appears in the SPECFIND V2.0 catalogue tool [77] and the 5C2 survey [53].
- We found that the sources 02, 06 and 12 have no prior information available in the literature.
- Source 03 is associated with the studies [78, 79] from the SDSS spectroscopic catalog, which classify this source as an M-Dwarf star.
- Source 04 is associated with the radio source PGC2285791 [7, 52], and due to its interesting extended radio emission it is the main subject of our study.

- Source 05 and 10 have been identified as optical galaxy clusters using an adaptive matched filter technique described in [72].
- Source 07 is a $z = 2.22$ QSO that seems to be a well studied source.
- Source 08 is associated with the radio source PGC2396883, has been part of a few statistical studies [4, 38] and also appears in the following catalogs [6, 7, 24, 40, 52].
- Source 09 also appears in [72] as well as the Gaussian Mixture Brightest Cluster Galaxy catalog (GMBCG) described in [31].
- Source 13 only appears in [77], The SPECFIND V2.0 catalogue of radio cross-identifications and spectra. SPECFIND meets the Virtual Observatory.
- The remaining two sources, Source 11 and B31059+460, appear in numerous catalogs, with Source 11 being described in [39, 41, 50, 52, 72, 73, 77], and Source B31059+460 in [5, 16, 24, 25, 27–30, 42, 77].

There are in total six sources which have an identification in the literature, namely: PGC2285791, PGC2396883, B31059+460, PSZ2 G133.60+69.04 in A1550, A1304+4649A in A1682 and IC 711. While the galaxy cluster A1682 and the radio galaxy IC 711 are well known extended radio sources, the other sources PGC2285791, PGC2396883, B31059+460 and PSZ2 G133.60+69.04 have only little information available in the literature.

We now present the preliminary derived images of the remaining extended radio sources from our sample in Figs. 4.8 - 4.24. The discussion of these sources is deferred to a later, appropriate, time when the sources have been fully analysed.

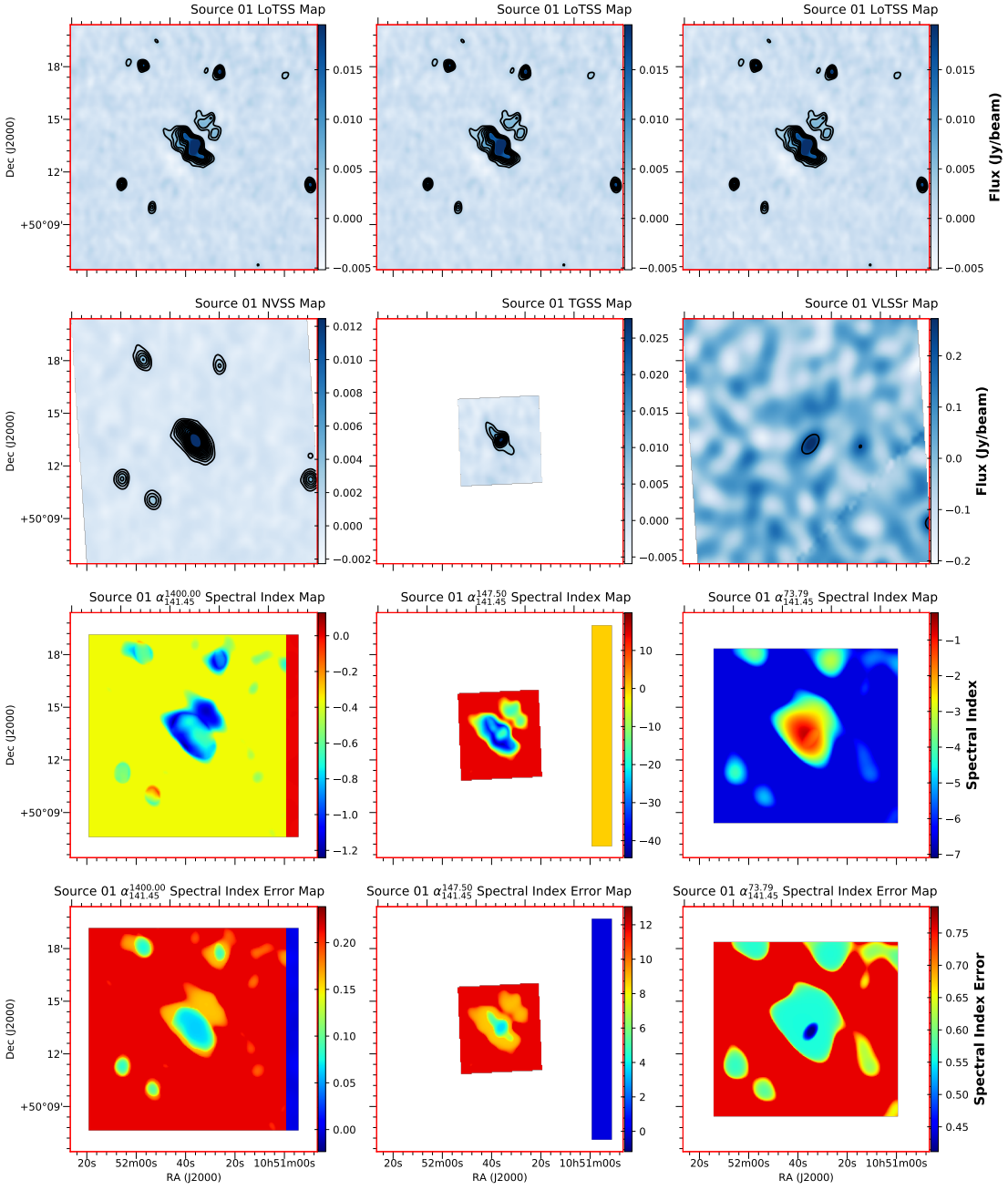


FIGURE 4.8: First row: the LoTSS 141.45 MHz continuum map of Source 01 overlaid with black LoTSS contours starting at 3σ ($\sigma = 0.91$ mJy/beam) with 2σ increments. Second row: continuum maps from the NVSS, TGSS and VLSSr surveys of Source 01 overlaid with black contours from each survey starting at 3σ ($\sigma_{\rm NVSS} = 0.40$ mJy/beam, $\sigma_{\rm TGSS} = 1.64$ mJy/beam, $\sigma_{\rm VLSSr} = 63.62$ mJy/beam) with 2σ increments. Third row: the two-frequency radio spectral index maps computed from the LoTSS map at 141.45 MHz in conjunction with the NVSS map at 1.4 GHz (left), TGSS map at 141.45 MHz (middle) and VLSSr map at 73.79 MHz (right). Last row: the two-frequency radio spectral index error maps computed from the LoTSS map at 141.45 MHz in conjunction with the NVSS map at 1.4 GHz (left), TGSS map at 141.45 MHz (middle) and VLSSr map at 73.79 MHz (right).

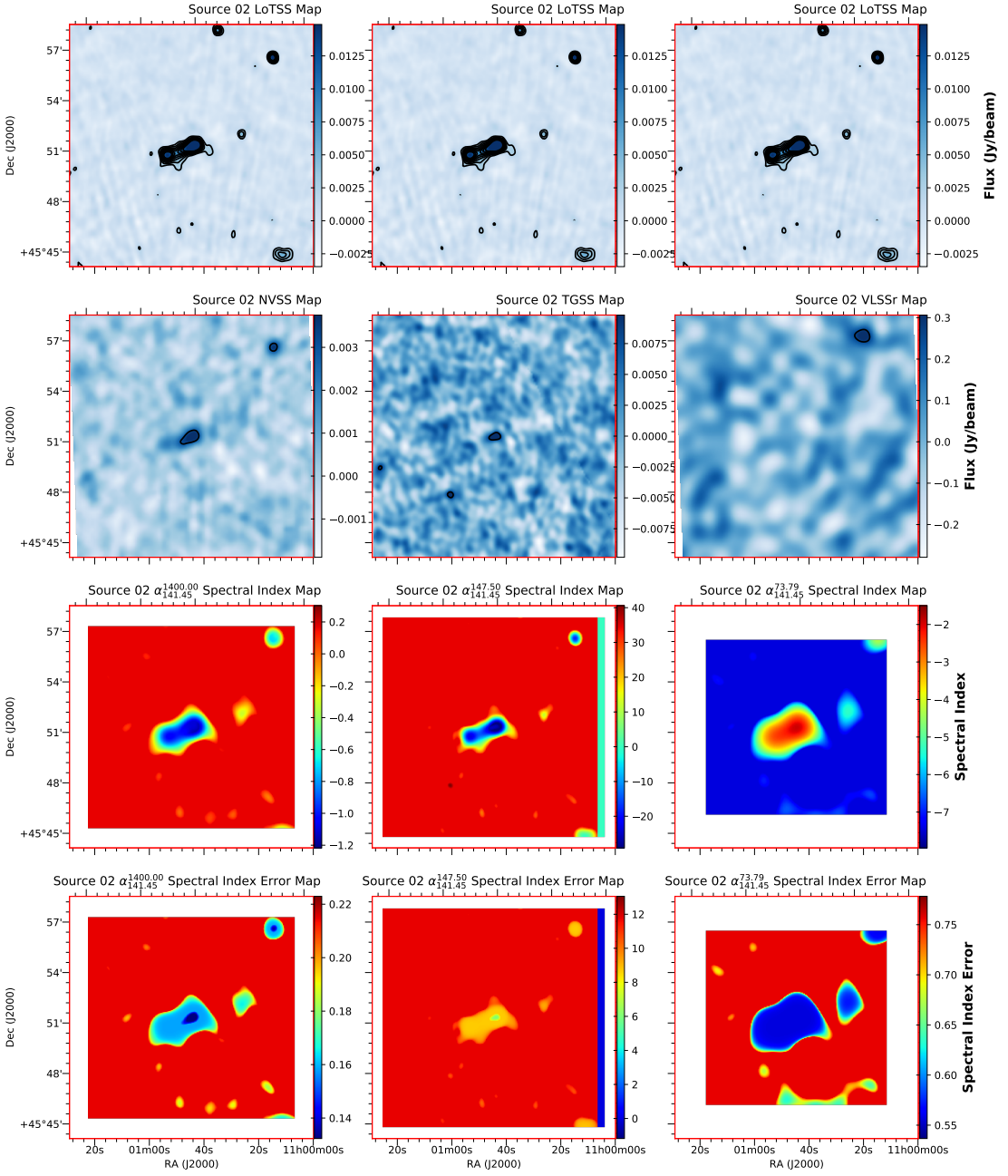


FIGURE 4.9: First row: the LoTSS 141.45 MHz continuum map of Source 02 overlaid with black LoTSS contours starting at 3σ ($\sigma = 0.68$ mJy/beam) with 2σ increments. Second row: continuum maps from the NVSS, TGSS and VLSSr surveys of Source 02 overlaid with black contours from each survey starting at 3σ ($\sigma_{\mathrm{NVSS}} = 0.99$ mJy/beam, $\sigma_{\mathrm{TGSS}} = 2.85$ mJy/beam, $\sigma_{\mathrm{VLSSr}} = 85.14$ mJy/beam) with 2σ increments. Third row: the two-frequency radio spectral index maps computed from the LoTSS map at 141.45 MHz in conjunction with the NVSS map at 1.4 GHz (left), TGSS map at 141.45 MHz (middle) and VLSSr map at 73.79 MHz (right). Last row: the two-frequency radio spectral index error maps computed from the LoTSS map at 141.45 MHz in conjunction with the NVSS map at 1.4 GHz (left), TGSS map at 141.45 MHz (middle) and VLSSr map at 73.79 MHz (right).

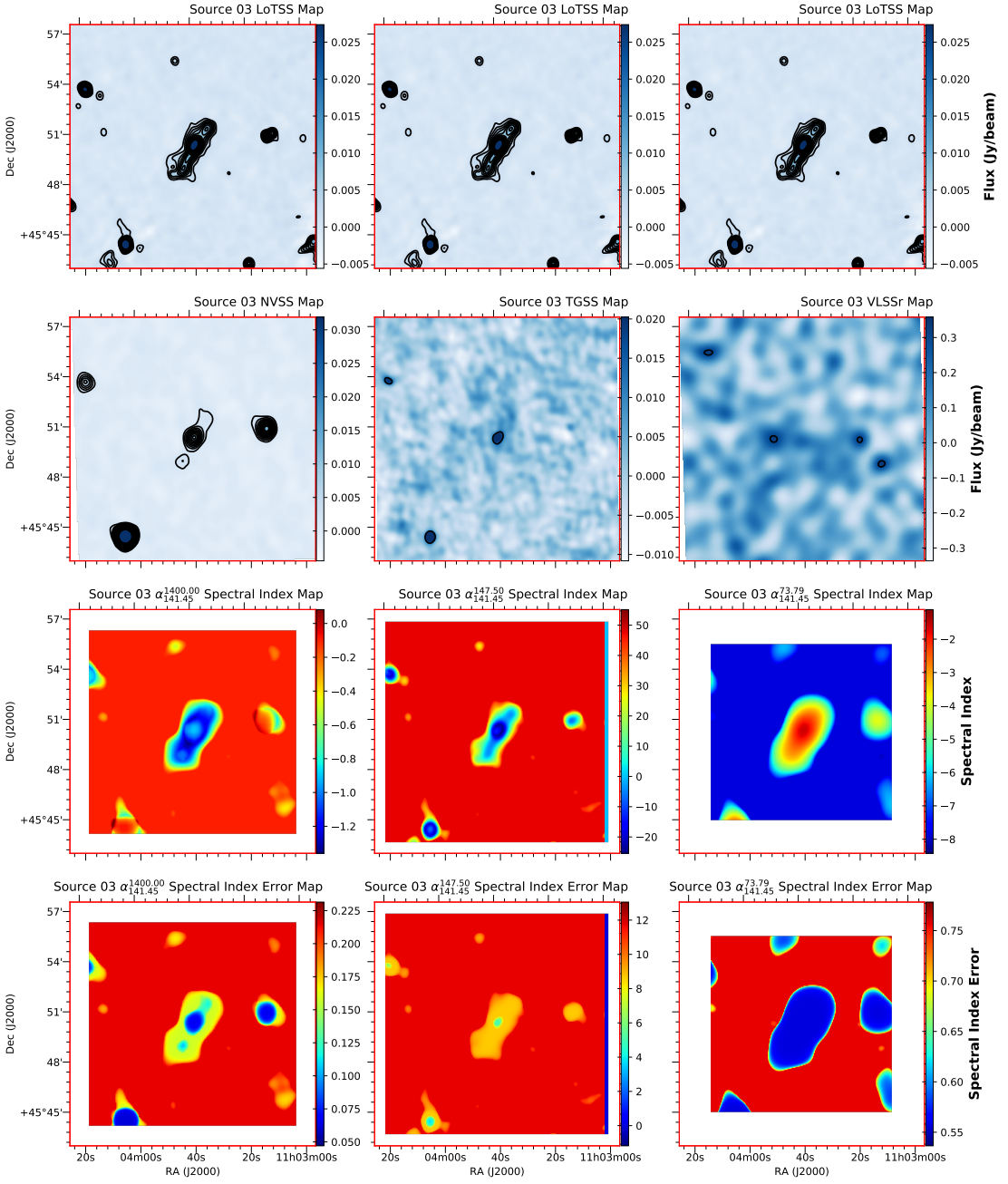


FIGURE 4.10: First row: the LoTSS 141.45 MHz continuum map of Source 03 overlaid with black LoTSS contours starting at 3σ ($\sigma = 0.62$ mJy/beam) with 2σ increments. Second row: continuum maps from the NVSS, TGSS and VLSSr surveys of Source 03 overlaid with black contours from each survey starting at 3σ ($\sigma_{\rm NVSS} = 0.50$ mJy/beam, $\sigma_{\rm TGSS} = 4.59$ mJy/beam, $\sigma_{\rm VLSSr} = 99.84$ mJy/beam) with 2σ increments. Third row: the two-frequency radio spectral index maps computed from the LoTSS map at 141.45 MHz in conjunction with the NVSS map at 1.4 GHz (left), TGSS map at 141.45 MHz (middle) and VLSSr map at 73.79 MHz (right). Last row: the two-frequency radio spectral index error maps computed from the LoTSS map at 141.45 MHz in conjunction with the NVSS map at 1.4 GHz (left), TGSS map at 141.45 MHz (middle) and VLSSr map at 73.79 MHz (right).

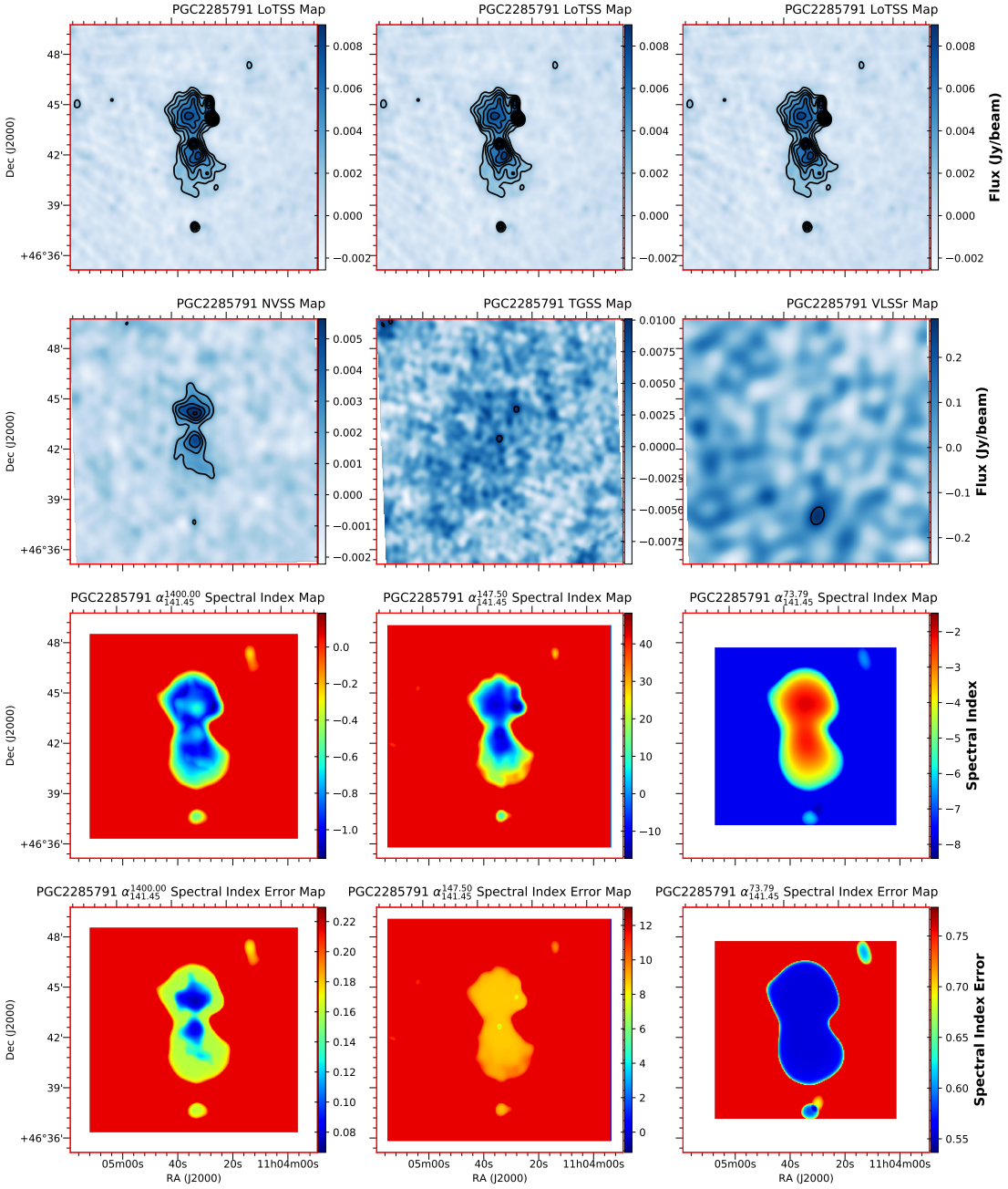


FIGURE 4.11: First row: the LoTSS 141.45 MHz continuum map of PGC2285791 overlaid with black LoTSS contours starting at 3σ (σ = 0.58 mJy/beam) with 2σ increments. Second row: continuum maps from the NVSS, TGSS and VLSSr surveys of PGC2285791 overlaid with black contours from each survey starting at 3σ ($\sigma_{\rm NVSS}$ = 0.57 mJy/beam, $\sigma_{\rm TGSS}$ = 2.99 mJy/beam, $\sigma_{\rm VLSSr}$ = 76.02 mJy/beam) with 2σ increments. Third row: the two-frequency radio spectral index maps computed from the LoTSS map at 141.45 MHz in conjunction with the NVSS map at 1.4 GHz (left), TGSS map at 141.45 MHz (middle) and VLSSr map at 73.79 MHz (right). Last row: the two-frequency radio spectral index error maps computed from the LoTSS map at 141.45 MHz in conjunction with the NVSS map at 1.4 GHz (left), TGSS map at 141.45 MHz (middle) and VLSSr map at 73.79 MHz (right).

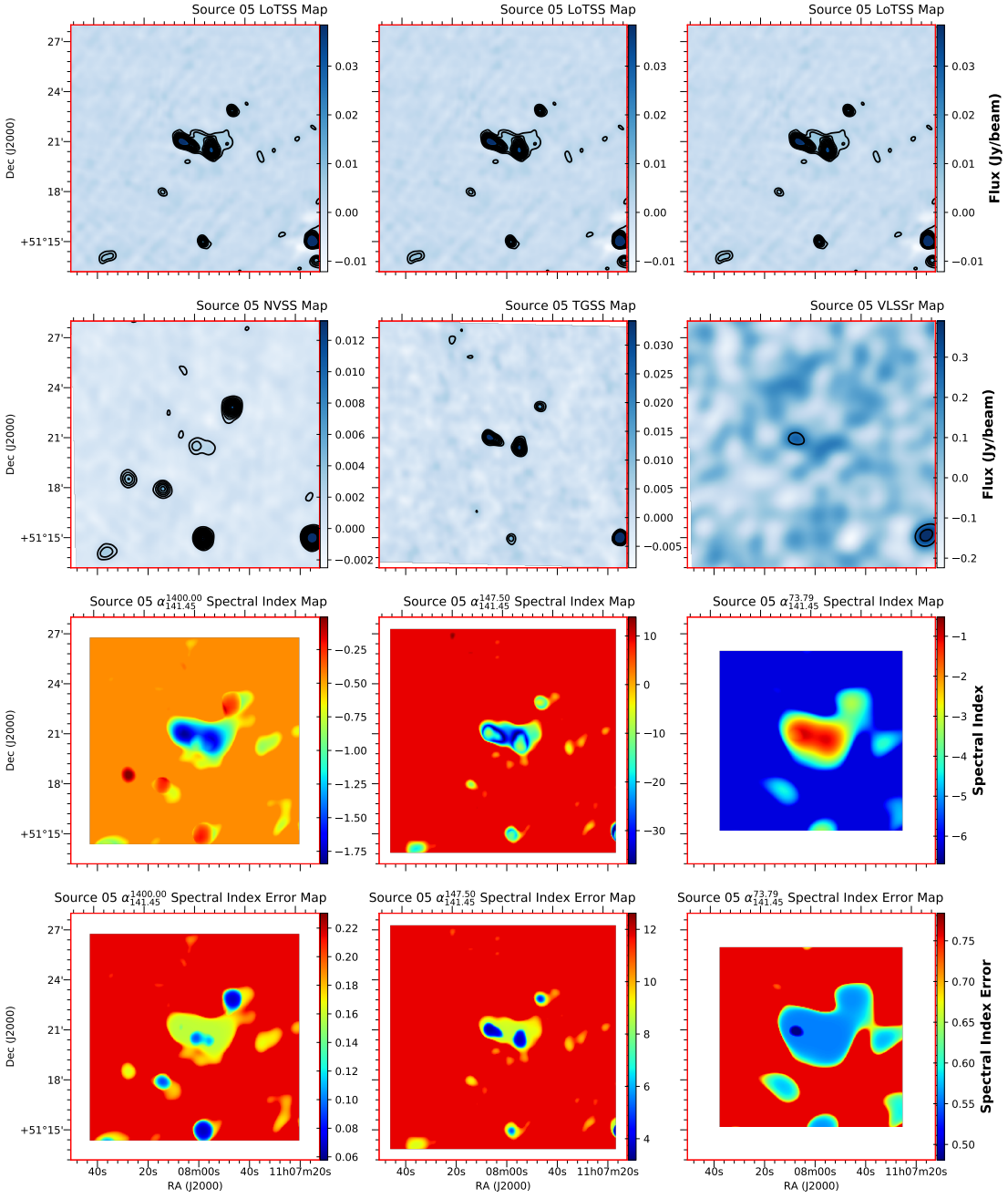


FIGURE 4.12: First row: the LoTSS 141.45 MHz continuum map of Source 05 overlaid with black LoTSS contours starting at 3σ (σ = 1.29 mJy/beam) with 2σ increments. Second row: continuum maps from the NVSS, TGSS and VLSSr surveys of Source 05 overlaid with black contours from each survey starting at 3σ ($\sigma_{\rm NVSS}$ = 0.46 mJy/beam, $\sigma_{\rm TGSS}$ = 1.90 mJy/beam, $\sigma_{\rm VLSSr}$ = 72.07 mJy/beam) with 2σ increments. Third row: the two-frequency radio spectral index maps computed from the LoTSS map at 141.45 MHz in conjunction with the NVSS map at 1.4 GHz (left), TGSS map at 141.45 MHz (middle) and VLSSr map at 73.79 MHz (right). Last row: the two-frequency radio spectral index error maps computed from the LoTSS map at 141.45 MHz in conjunction with the NVSS map at 1.4 GHz (left), TGSS map at 141.45 MHz (middle) and VLSSr map at 73.79 MHz (right).

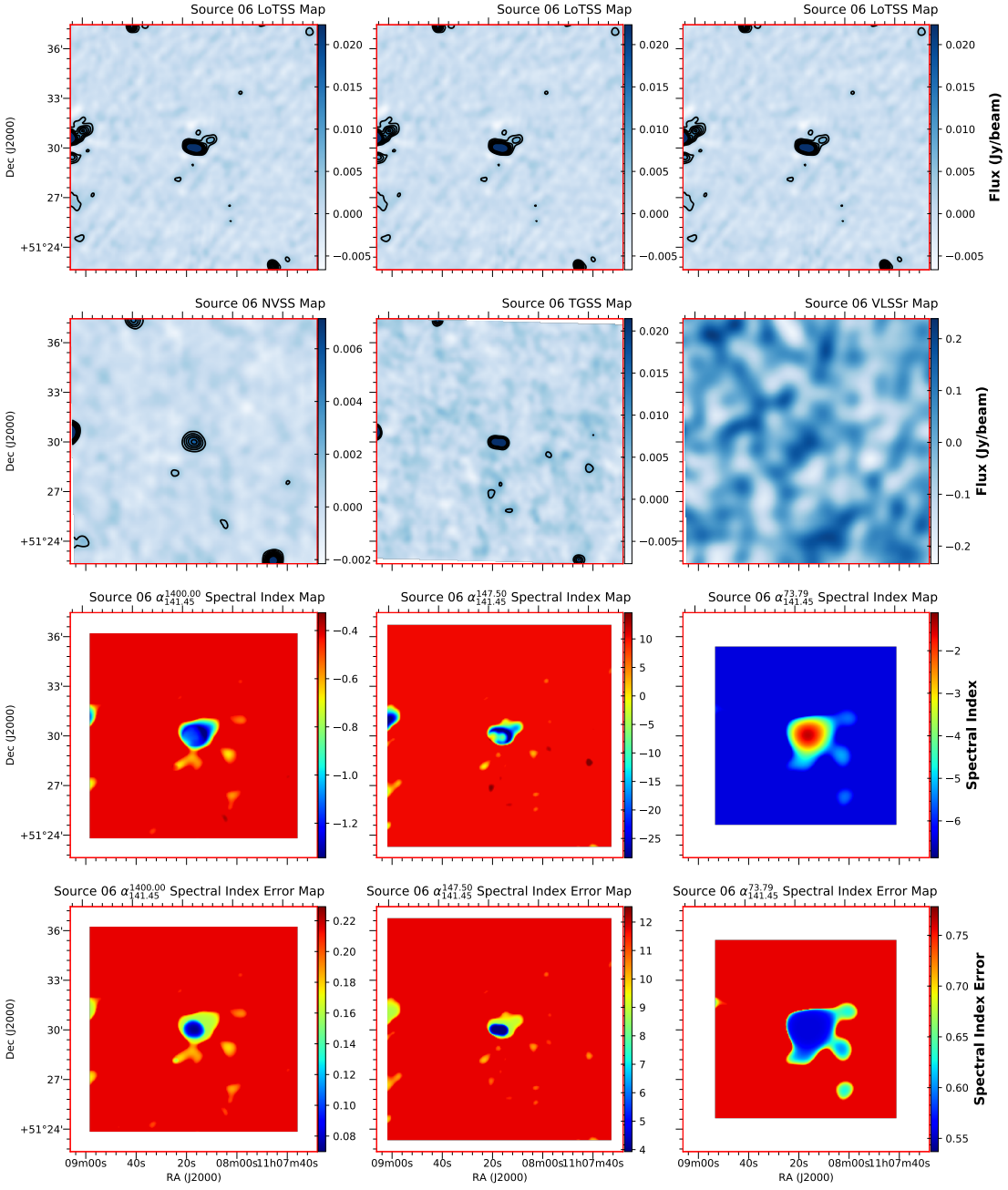


FIGURE 4.13: First row: the LoTSS 141.45 MHz continuum map of Source 06 overlaid with black LoTSS contours starting at 3σ ($\sigma = 1.20$ mJy/beam) with 2σ increments. Second row: continuum maps from the NVSS, TGSS and VLSSr surveys of Source 06 overlaid with black contours from each survey starting at 3σ ($\sigma_{\rm NVSS} = 0.46$ mJy/beam, $\sigma_{\rm TGSS} = 1.85$ mJy/beam, $\sigma_{\rm VLSSr} = 76.68$ mJy/beam) with 2σ increments. Third row: the two-frequency radio spectral index maps computed from the LoTSS map at 141.45 MHz in conjunction with the NVSS map at 1.4 GHz (left), TGSS map at 141.45 MHz (middle) and VLSSr map at 73.79 MHz (right). Last row: the two-frequency radio spectral index error maps computed from the LoTSS map at 141.45 MHz in conjunction with the NVSS map at 1.4 GHz (left), TGSS map at 141.45 MHz (middle) and VLSSr map at 73.79 MHz (right).

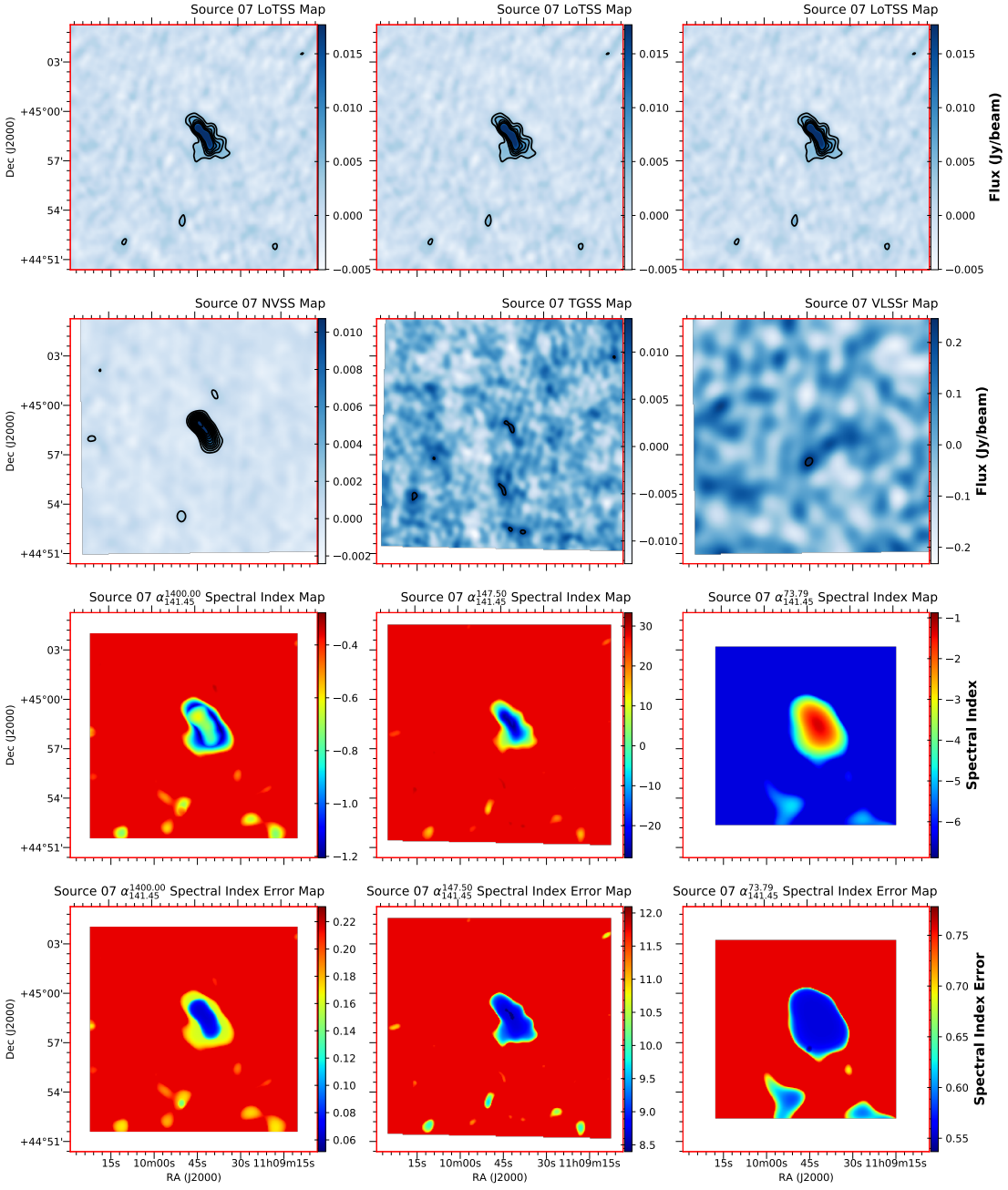


FIGURE 4.14: First row: the LoTSS 141.45 MHz continuum map of Source 07 overlaid with black LoTSS contours starting at 3σ ($\sigma = 1.17$ mJy/beam) with 2σ increments. Second row: continuum maps from the NVSS, TGSS and VLSSr surveys of Source 07 overlaid with black contours from each survey starting at 3σ ($\sigma_{\rm NVSS} = 0.51$ mJy/beam, $\sigma_{\rm TGSS} = 3.74$ mJy/beam, $\sigma_{\rm VLSSr} = 74.61$ mJy/beam) with 2σ increments. Third row: the two-frequency radio spectral index maps computed from the LoTSS map at 141.45 MHz in conjunction with the NVSS map at 1.4 GHz (left), TGSS map at 141.45 MHz (middle) and VLSSr map at 73.79 MHz (right). Last row: the two-frequency radio spectral index error maps computed from the LoTSS map at 141.45 MHz in conjunction with the NVSS map at 1.4 GHz (left), TGSS map at 141.45 MHz (middle) and VLSSr map at 73.79 MHz (right).

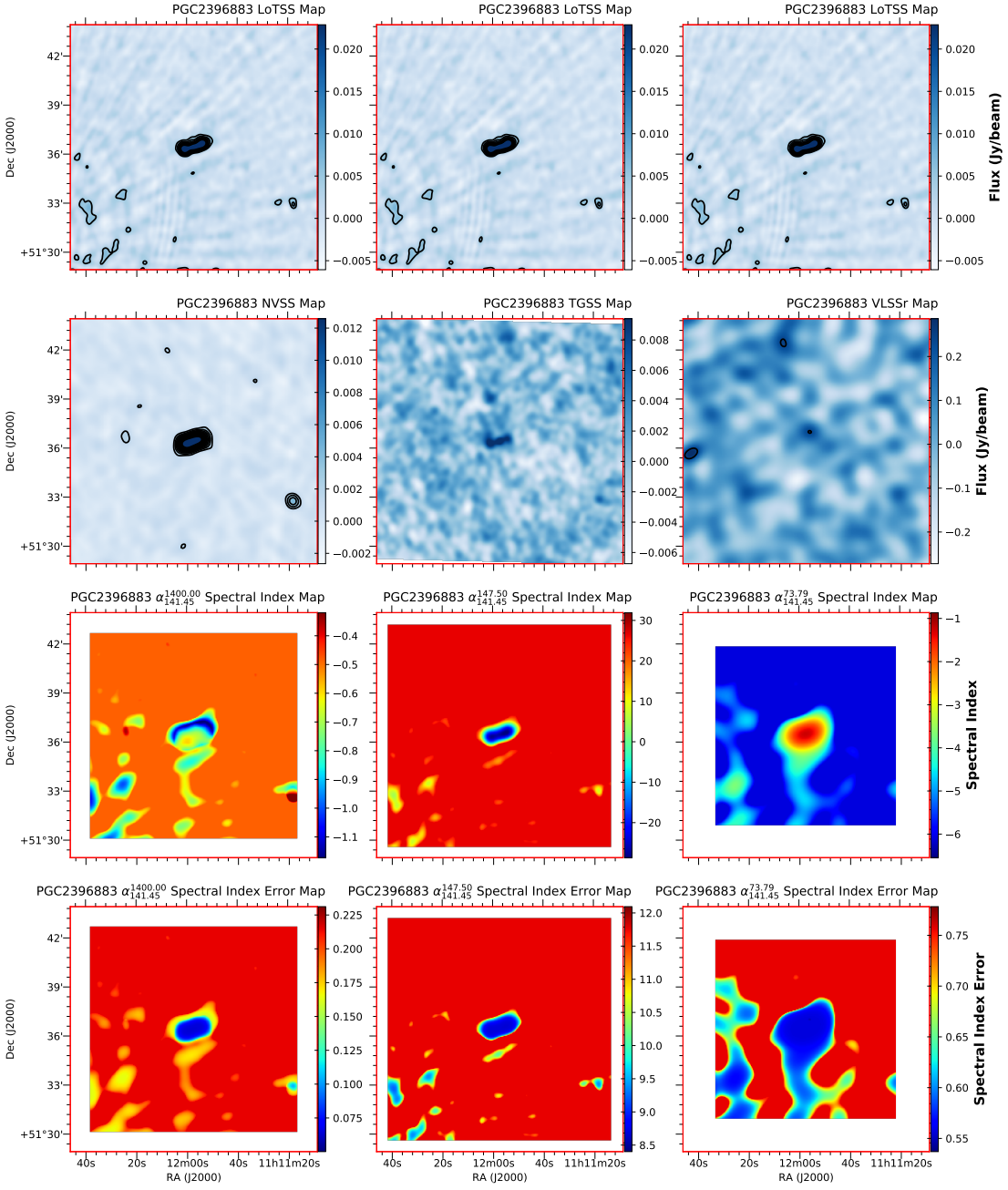


FIGURE 4.15: First row: the LoTSS 141.45 MHz continuum map of PGC2396883 overlaid with black LoTSS contours starting at 3σ (σ = 1.52 mJy/beam) with 2σ increments. Second row: continuum maps from the NVSS, TGSS and VLSSr surveys of PGC2396883 overlaid with black contours from each survey starting at 3σ ($\sigma_{\rm NVSS}$ = 0.50 mJy/beam, $\sigma_{\rm TGSS}$ = 4.59 mJy/beam, $\sigma_{\rm VLSSr}$ = 79.30 mJy/beam) with 2σ increments. Third row: the two-frequency radio spectral index maps computed from the LoTSS map at 141.45 MHz in conjunction with the NVSS map at 1.4 GHz (left), TGSS map at 141.45 MHz (middle) and VLSSr map at 73.79 MHz (right). Last row: the two-frequency radio spectral index error maps computed from the LoTSS map at 141.45 MHz in conjunction with the NVSS map at 1.4 GHz (left), TGSS map at 141.45 MHz (middle) and VLSSr map at 73.79 MHz (right).

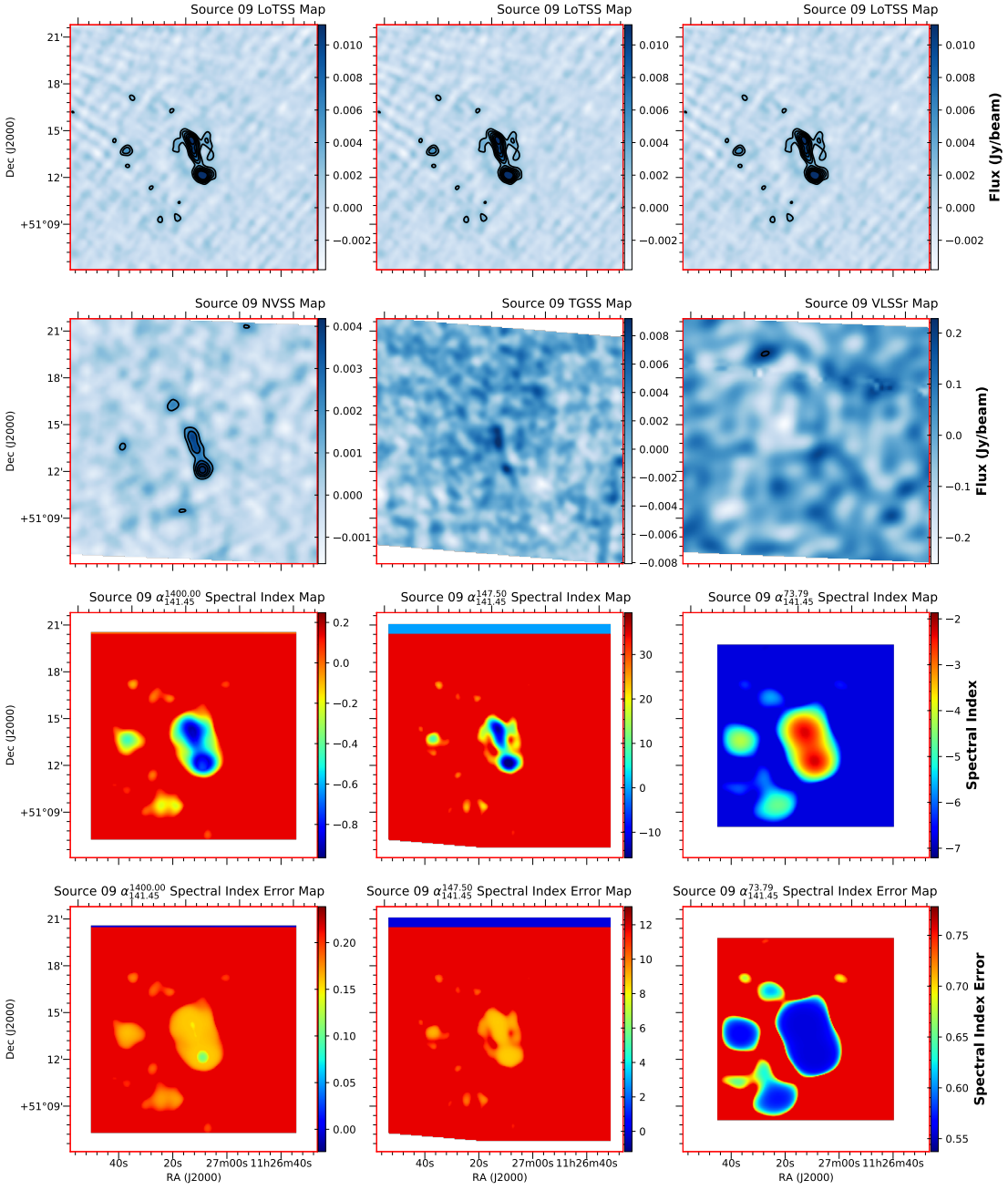


FIGURE 4.16: First row: the LoTSS 141.45 MHz continuum map of Source 09 overlaid with black LoTSS contours starting at 3σ (σ = 0.86 mJy/beam) with 2σ increments. Second row: continuum maps from the NVSS, TGSS and VLSSr surveys of Source 09 overlaid with black contours from each survey starting at 3σ ($\sigma_{\rm NVSS}$ = 0.59 mJy/beam, $\sigma_{\rm TGSS}$ = 3.63 mJy/beam, $\sigma_{\rm VLSSr}$ = 70.16 mJy/beam) with 2σ increments. Third row: the two-frequency radio spectral index maps computed from the LoTSS map at 141.45 MHz in conjunction with the NVSS map at 1.4 GHz (left), TGSS map at 141.45 MHz (middle) and VLSSr map at 73.79 MHz (right). Last row: the two-frequency radio spectral index error maps computed from the LoTSS map at 141.45 MHz in conjunction with the NVSS map at 1.4 GHz (left), TGSS map at 141.45 MHz (middle) and VLSSr map at 73.79 MHz (right).

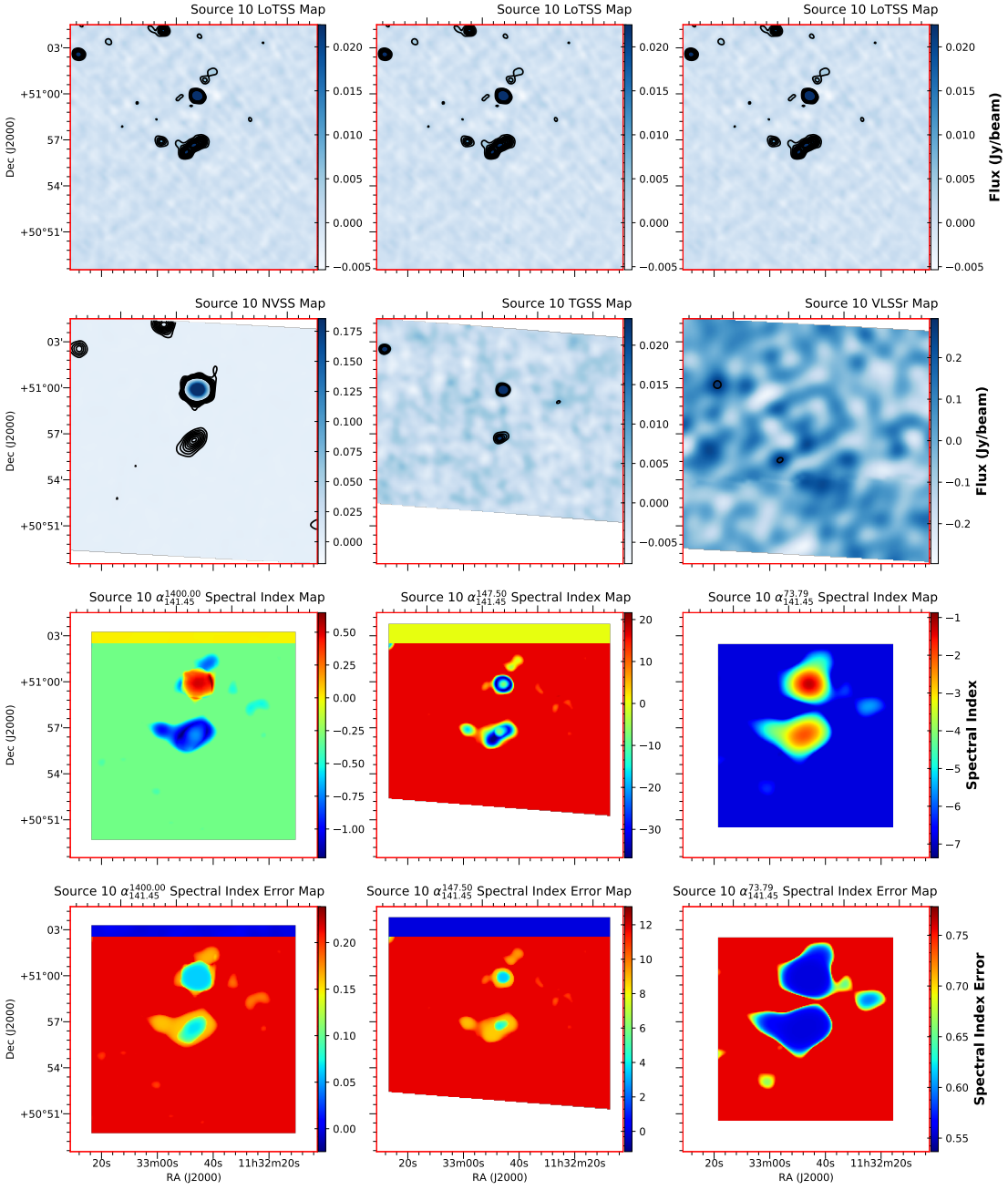


FIGURE 4.17: First row: the LoTSS 141.45 MHz continuum map of Source 10 overlaid with black LoTSS contours starting at 3σ (σ = 1.02 mJy/beam) with 2σ increments. Second row: continuum maps from the NVSS, TGSS and VLSSr surveys of Source 10 overlaid with black contours from each survey starting at 3σ ($\sigma_{\rm NVSS}$ = 0.50 mJy/beam, $\sigma_{\rm TGSS}$ = 2.02 mJy/beam, $\sigma_{\rm VLSSr}$ = 86.59 mJy/beam) with 2σ increments. Third row: the two-frequency radio spectral index maps computed from the LoTSS map at 141.45 MHz in conjunction with the NVSS map at 1.4 GHz (left), TGSS map at 141.45 MHz (middle) and VLSSr map at 73.79 MHz (right). Last row: the two-frequency radio spectral index error maps computed from the LoTSS map at 141.45 MHz in conjunction with the NVSS map at 1.4 GHz (left), TGSS map at 141.45 MHz (middle) and VLSSr map at 73.79 MHz (right).

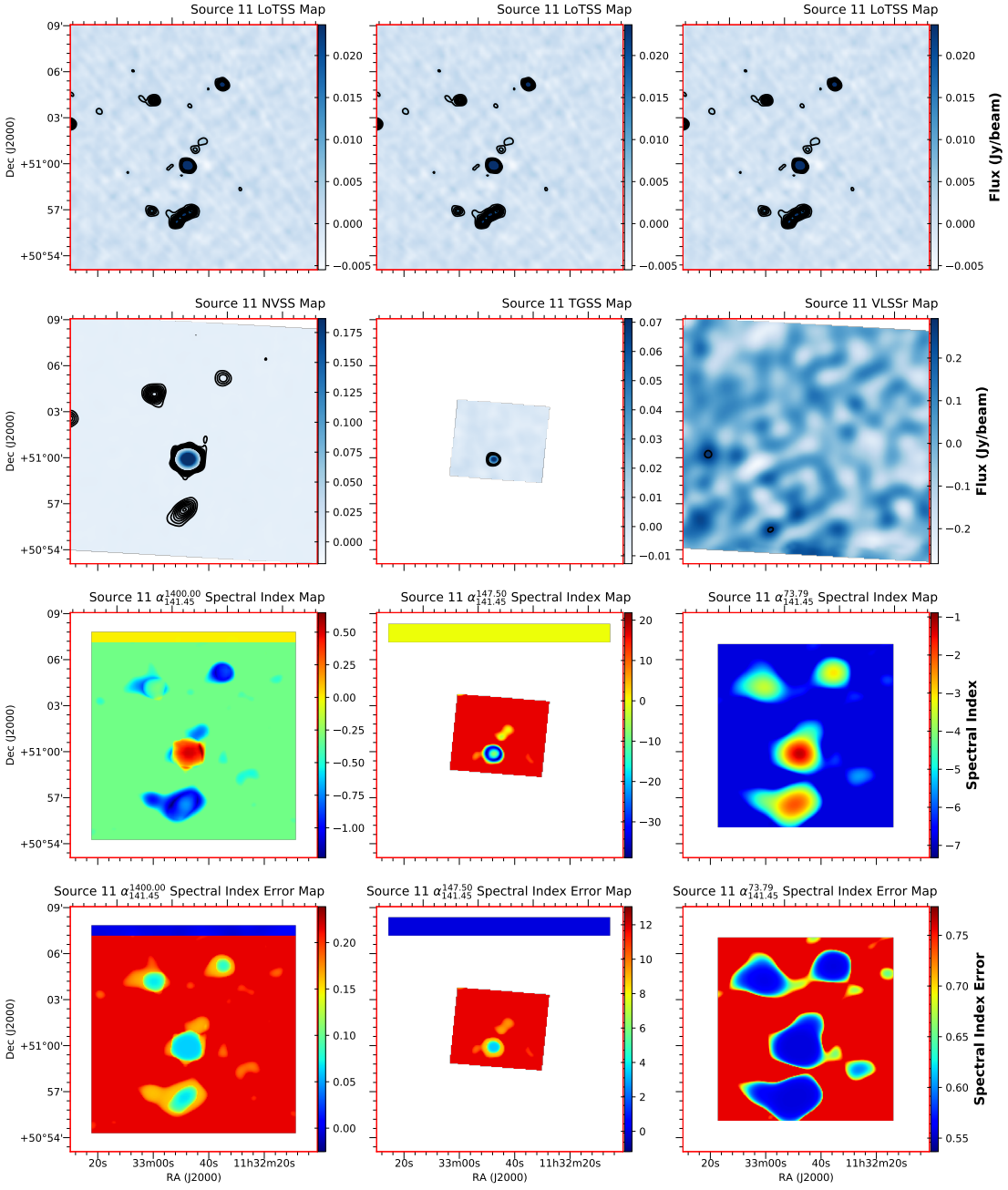


FIGURE 4.18: First row: the LoTSS 141.45 MHz continuum map of Source 11 overlaid with black LoTSS contours starting at 3σ (σ = 1.05 mJy/beam) with 2σ increments. Second row: continuum maps from the NVSS, TGSS and VLSSr surveys of Source 11 overlaid with black contours from each survey starting at 3σ ($\sigma_{\rm NVSS}$ = 0.51 mJy/beam, $\sigma_{\rm TGSS}$ = 2.08 mJy/beam, $\sigma_{\rm VLSSr}$ = 87.18 mJy/beam) with 2σ increments. Third row: the two-frequency radio spectral index maps computed from the LoTSS map at 141.45 MHz in conjunction with the NVSS map at 1.4 GHz (left), TGSS map at 141.45 MHz (middle) and VLSSr map at 73.79 MHz (right). Last row: the two-frequency radio spectral index error maps computed from the LoTSS map at 141.45 MHz in conjunction with the NVSS map at 1.4 GHz (left), TGSS map at 141.45 MHz (middle) and VLSSr map at 73.79 MHz (right).

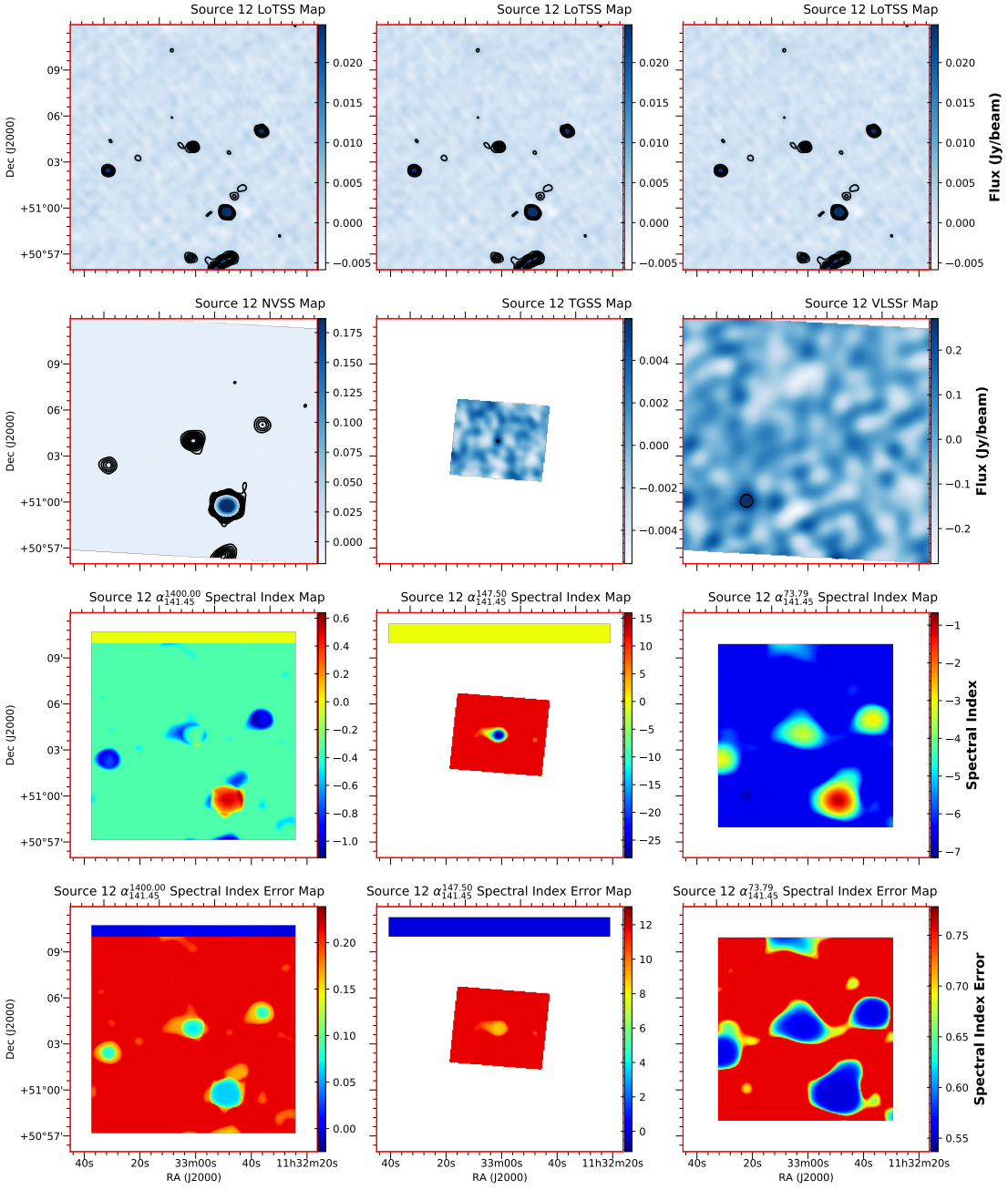


FIGURE 4.19: First row: the LoTSS 141.45 MHz continuum map of Source 12 overlaid with black LoTSS contours starting at 3σ ($\sigma = 1.09$ mJy/beam) with 2σ increments. Second row: continuum maps from the NVSS, TGSS and VLSSr surveys of Source 12 overlaid with black contours from each survey starting at 3σ ($\sigma_{\rm NVSS} = 0.50$ mJy/beam, $\sigma_{\rm TGSS} = 1.80$ mJy/beam, $\sigma_{\rm VLSSr} = 75.89$ mJy/beam) with 2σ increments. Third row: the two-frequency radio spectral index maps computed from the LoTSS map at 141.45 MHz in conjunction with the NVSS map at 1.4 GHz (left), TGSS map at 141.45 MHz (middle) and VLSSr map at 73.79 MHz (right). Last row: the two-frequency radio spectral index error maps computed from the LoTSS map at 141.45 MHz in conjunction with the NVSS map at 1.4 GHz (left), TGSS map at 141.45 MHz (middle) and VLSSr map at 73.79 MHz (right).

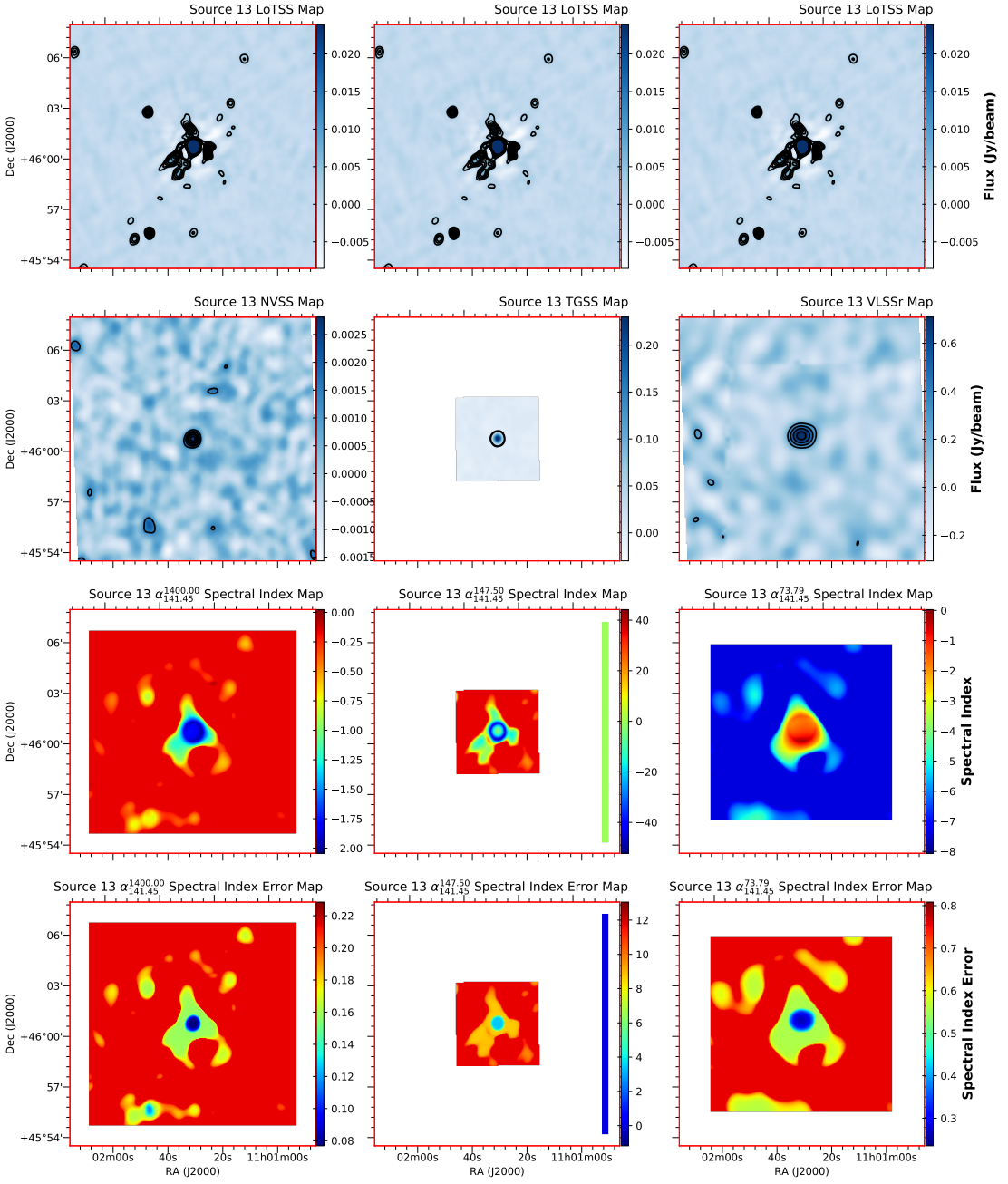


FIGURE 4.20: First row: the LoTSS 141.45 MHz continuum map of Source 13 overlaid with black LoTSS contours starting at 3σ (σ = 0.67 mJy/beam) with 2σ increments. Second row: continuum maps from the NVSS, TGSS and VLSSr surveys of Source 13 overlaid with black contours from each survey starting at 3σ ($\sigma_{\rm NVSS}$ = 0.46 mJy/beam, $\sigma_{\rm TGSS}$ = 2.95 mJy/beam, $\sigma_{\rm VLSSr}$ = 82.32 mJy/beam) with 2σ increments. Third row: the two-frequency radio spectral index maps computed from the LoTSS map at 141.45 MHz in conjunction with the NVSS map at 1.4 GHz (left), TGSS map at 141.45 MHz (middle) and VLSSr map at 73.79 MHz (right). Last row: the two-frequency radio spectral index error maps computed from the LoTSS map at 141.45 MHz in conjunction with the NVSS map at 1.4 GHz (left), TGSS map at 141.45 MHz (middle) and VLSSr map at 73.79 MHz (right).

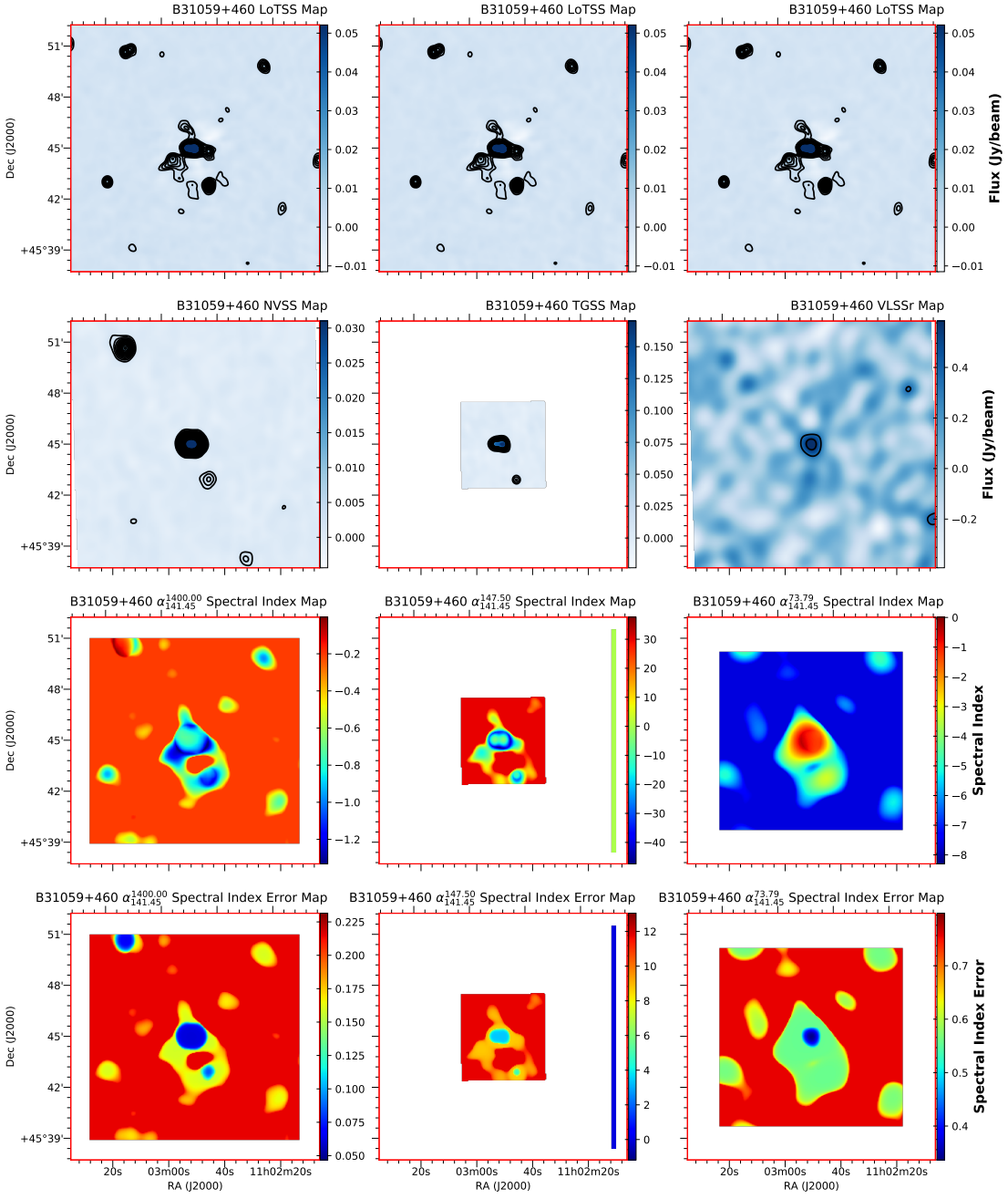


FIGURE 4.21: First row: the LoTSS 141.45 MHz continuum map of B31059+460 overlaid with black LoTSS contours starting at 3σ (σ = 0.79 mJy/beam) with 2σ increments. Second row: continuum maps from the NVSS, TGSS and VLSSr surveys of B31059+460 overlaid with black contours from each survey starting at 3σ ($\sigma_{\rm NVSS}$ = 0.49 mJy/beam, $\sigma_{\rm TGSS}$ = 2.76 mJy/beam, $\sigma_{\rm VLSSr}$ = 112.18 mJy/beam) with 2σ increments. Third row: the two-frequency radio spectral index maps computed from the LoTSS map at 141.45 MHz in conjunction with the NVSS map at 1.4 GHz (left), TGSS map at 141.45 MHz (middle) and VLSSr map at 73.79 MHz (right). Last row: the two-frequency radio spectral index error maps computed from the LoTSS map at 141.45 MHz in conjunction with the NVSS map at 1.4 GHz (left), TGSS map at 141.45 MHz (middle) and VLSSr map at 73.79 MHz (right).

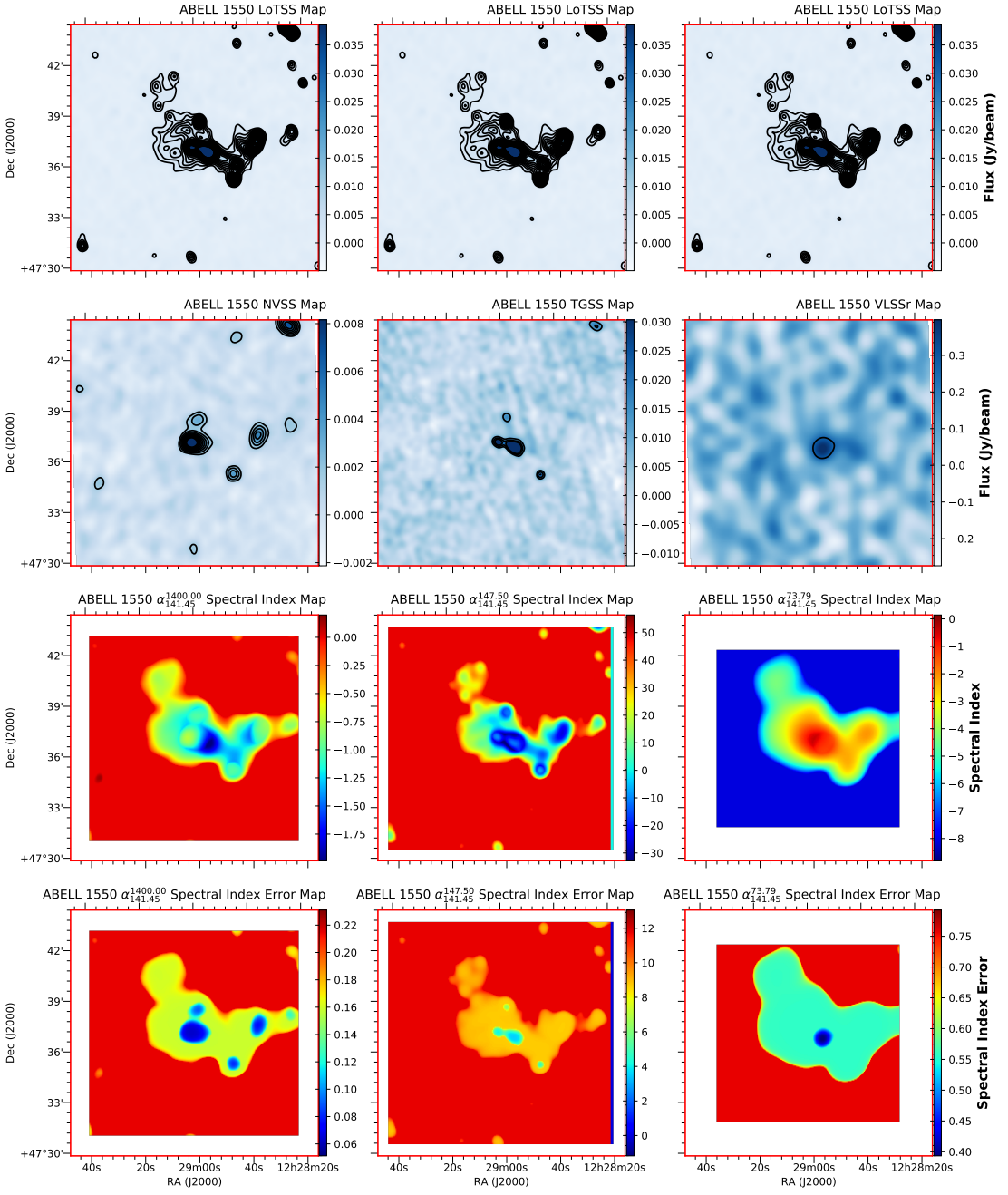


FIGURE 4.22: First row: the LoTSS 141.45 MHz continuum map of ABELL 1550 overlaid with black LoTSS contours starting at 3σ (σ = 0.46 mJy/beam) with 2σ increments. Second row: continuum maps from the NVSS, TGSS and VLSSr surveys of ABELL 1550 overlaid with black contours from each survey starting at 3σ ($\sigma_{\rm NVSS}$ = 0.46 mJy/beam, $\sigma_{\rm TGSS}$ = 3.47 mJy/beam, $\sigma_{\rm VLSSr}$ = 87.97 mJy/beam) with 2σ increments. Third row: the two-frequency radio spectral index maps computed from the LoTSS map at 141.45 MHz in conjunction with the NVSS map at 1.4 GHz (left), TGSS map at 141.45 MHz (middle) and VLSSr map at 73.79 MHz (right). Last row: the two-frequency radio spectral index error maps computed from the LoTSS map at 141.45 MHz in conjunction with the NVSS map at 1.4 GHz (left), TGSS map at 141.45 MHz (middle) and VLSSr map at 73.79 MHz (right).

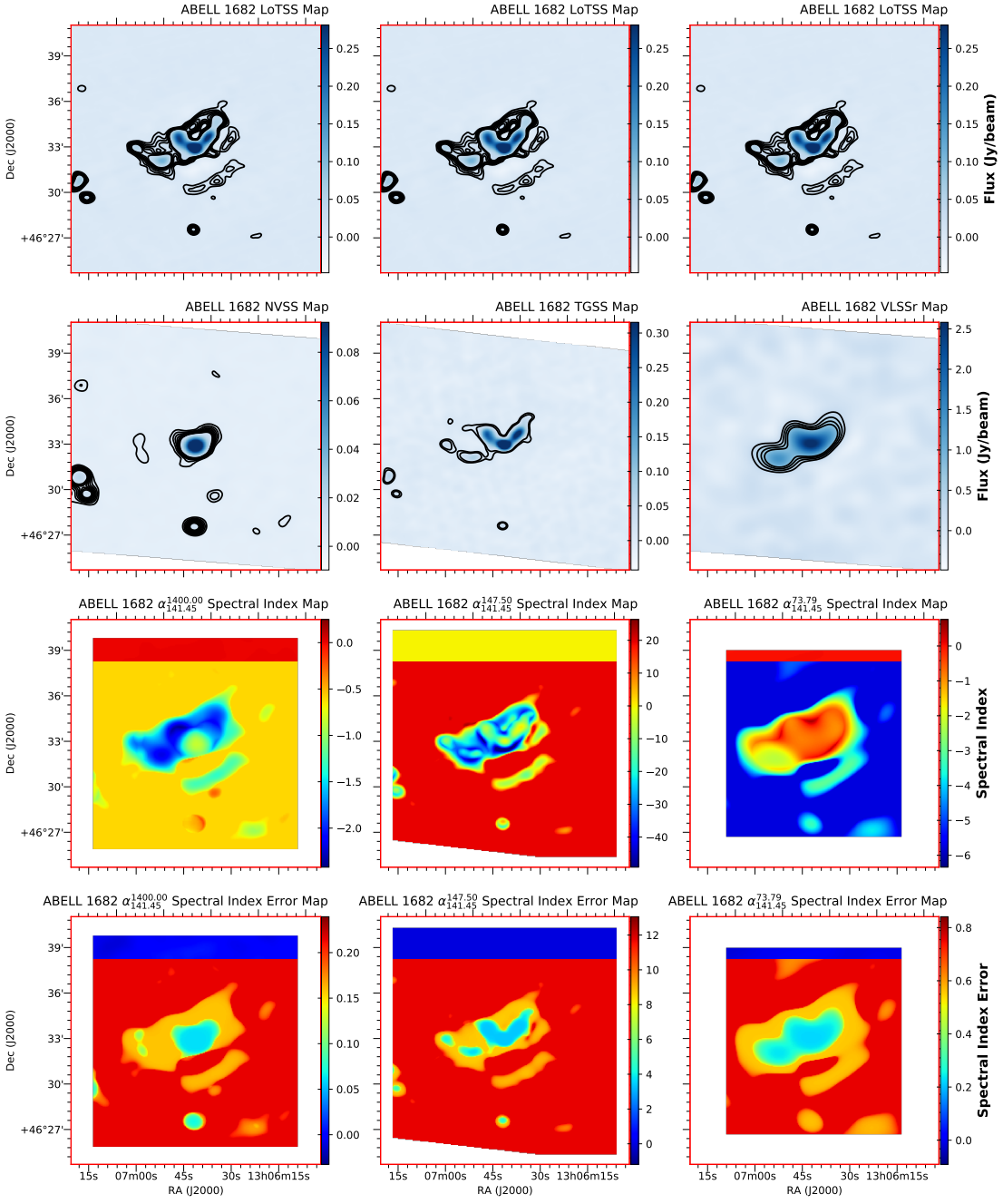


FIGURE 4.23: First row: the LoTSS 141.45 MHz continuum map of ABELL 1682 overlaid with black LoTSS contours starting at 3σ (σ = 2.08 mJy/beam) with 2σ increments. Second row: continuum maps from the NVSS, TGSS and VLSSr surveys of ABELL 1682 overlaid with black contours from each survey starting at 3σ ($\sigma_{\rm NVSS}$ = 0.53 mJy/beam, $\sigma_{\rm TGSS}$ = 4.70 mJy/beam, $\sigma_{\rm VLSSr}$ = 87.97 mJy/beam) with 2σ increments. Third row: the two-frequency radio spectral index maps computed from the LoTSS map at 141.45 MHz in conjunction with the NVSS map at 1.4 GHz (left), TGSS map at 141.45 MHz (middle) and VLSSr map at 73.79 MHz (right). Last row: the two-frequency radio spectral index error maps computed from the LoTSS map at 141.45 MHz in conjunction with the NVSS map at 1.4 GHz (left), TGSS map at 141.45 MHz (middle) and VLSSr map at 73.79 MHz (right).

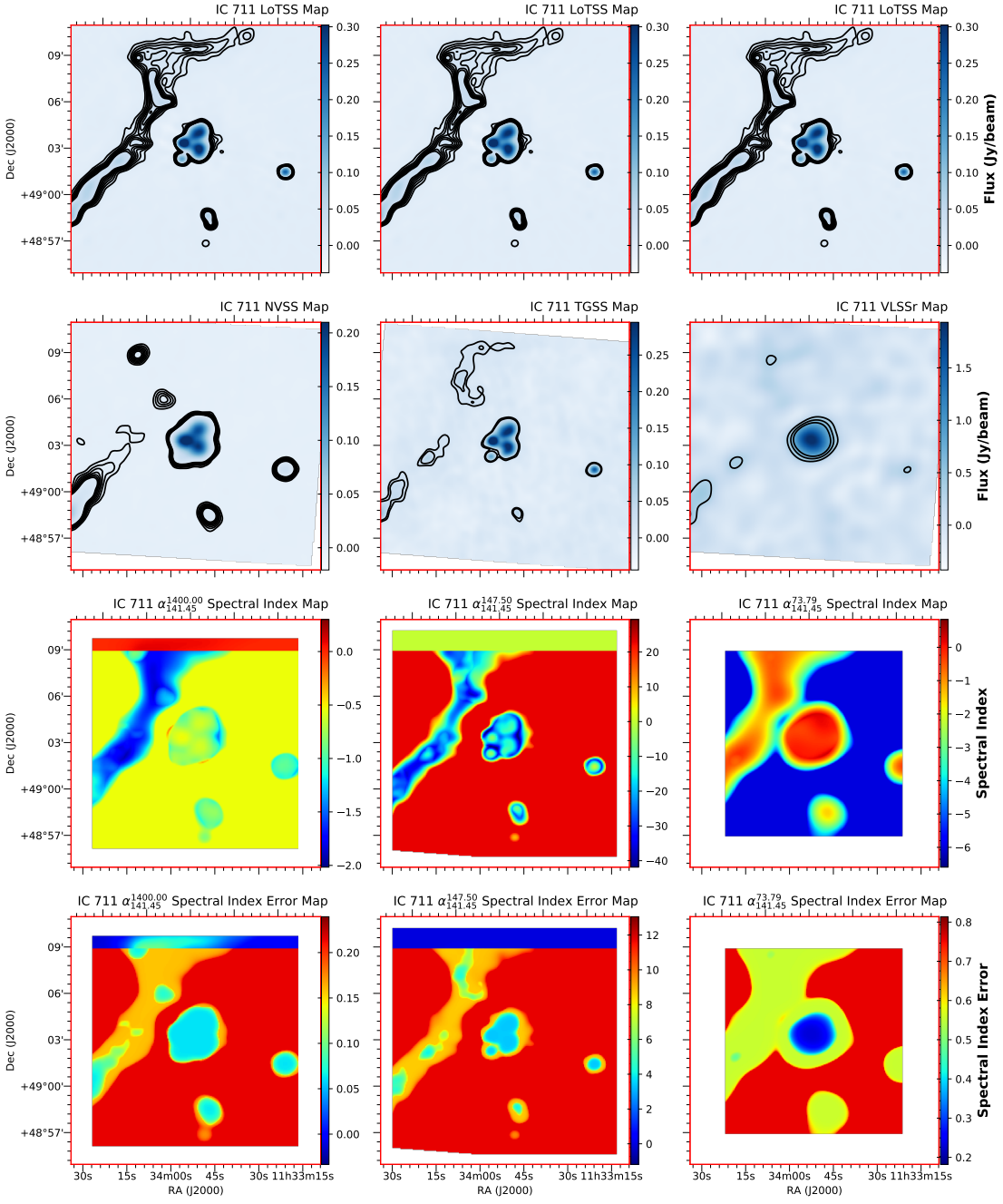


FIGURE 4.24: First row: the LoTSS 141.45 MHz continuum map of IC 711 overlaid with black LoTSS contours starting at 3σ ($\sigma = 2.13$ mJy/beam) with 2σ increments. Second row: continuum maps from the NVSS, TGSS and VLSSr surveys of IC 711 overlaid with black contours from each survey starting at 3σ ($\sigma_{\rm NVSS} = 0.62$ mJy/beam, $\sigma_{\rm TGSS} = 5.55$ mJy/beam, $\sigma_{\rm VLSSr} = 104.4$ mJy/beam) with 2σ increments. Third row: the two-frequency radio spectral index maps computed from the LoTSS map at 141.45 MHz in conjunction with the NVSS map at 1.4 GHz (left), TGSS map at 141.45 MHz (middle) and VLSSr map at 73.79 MHz (right). Last row: the two-frequency radio spectral index error maps computed from the LoTSS map at 141.45 MHz in conjunction with the NVSS map at 1.4 GHz (left), TGSS map at 141.45 MHz (middle) and VLSSr map at 73.79 MHz (right).

Chapter 5

Conclusions

We used high resolution LoTSS images to search for low-surface brightness extended sources at low frequencies. This has enabled us to uncover several either previously unknown or poorly studied low-surface brightness extended radio sources. In this section we conclude on the results of PGC2285791, described in Chapter 4.1, as the main interest of this dissertation.

Our search has revealed a very interesting radio morphology and spectral distribution of PGC228579, enabling us to better characterise the source. We produced spectral index distribution maps by combining the LoTSS image at 141 MHz and NVSS image at 1.4 GHz. The spectral index of the extended radio source PGC2285791 varies from $\alpha = -1.1$ to $\alpha = -0.5$. An island of a flat spectral region ($\alpha = -0.6$) and hot spots ($\alpha = -1.0$) are observed.

The morphology and spectral index distribution of the source suggest a scenario in which the lobe is filled with relativistic electrons from a two-stage outflow: a first stage in which these particles have been injected at early times and are now suffering energy losses and ageing effects, and a more recent stage during which a further outflow of particles has been generated by the galaxy or a collimated outflow.

However, wide frequency observations are necessary for detailed spectral index maps and to gain further insight into the physical environment of PGC2285791. Regardless, the study presented here shows the value of the high resolution and high sensitivity of LOFAR maps for studies of low surface brightness sources.

Bibliography

[1] Allen J. T. et al., 2011, MNRAS, 410, 860-884

[2] Andrei A. H. et al., 2009, AAP, 505, 385-404

[3] ASTRON Team, online page titled "LOFAR STATIONS: DESCRIPTION AND LAYOUT". (accessed 06 January, 2018)
`https://www.astron.nl/radio-observatory/astronomers/users/technical-information/lofar-stations/lofar-stations-description-`

[4] Barber T., Meiksin A., Murphy T., 2007, MNRAS, 377, 787-805

[5] Becker R. H., White R. L., Edwards A. L., 1991, APJS, 75, 1-229

[6] Best P. N., Kauffmann G., Heckman T. M., Ivezić Ž., 2005, MNRAS, 362, 9-24

[7] Best P. N., Heckman T. M., 2012, MNRAS, 421, 1569-1582

[8] Bonnarel F. et al., 2000, AAPS, 143, 33-40

[9] Bornancini C. G., O'Mill A. L., Gurovich S., Lambas D. G., 2010, MNRAS, 406, 197-207

[10] Bradt H., 2010, "Astrophysics Processes", Cambridge University Press, First edition, 290

[11] Brau J., online image titled "Galaxies", 3 April 2010. (accessed December 22, 2017)
`http://pages.uoregon.edu/jimbrau/BrauImNew/Chap24/6th/24_35Figurea-F.jpg`

[12] Brienza M. et al., 2016, AAP, 585, A29

[13] Cantwell T. M. et al., 2016, MNRAS, 458, 1803-1814

[14] Chen Z.-F. et al., 2014, APJS, 210, 7

[15] Chen Z.-F., Gu Q.-S., Chen Y.-M., 2015, APJS, 221, 32

[16] Cohen A. S et al., 2007, AJ, 134, 1245-1262

[17] Condon J. J. et al., 1998, AJ, 115, 1693-1716

[18] Condon J. J., 1992, ARAA, 30, 575-611

[19] Cooksey K. L. et al., 2013, APJ, 763, 37

[20] Croston J. H. et al., 2008, APJ, 688, 190-197

[21] Duric N., Seaquist E. R., 1988, APJ, 326, 574

[22] Egger J. M., 2006, ArXiv Mathematics e-prints

[23] Fanaroff B. L., Riley J. M., 1974, MNRAS, 167, 31-36

[24] Farnes J. S., Gaensler B. M., Carretti E., 2014, APJS, 212, 15

[25] Ficarra A., Grueff G., Tomassetti G., 1985, AAPS, 59, 255-347

[26] Gaia Collaboration et al., 2016, AAP, 595, A2

[27] Green D. A., Riley J. M., 1995, MNRAS, 274, 324-336

[28] Gregory P. C., Condon J. J., 1991, APJS, 75, 1011-1291

[29] Gregory P. C., Scott W. K., Douglas K., Condon J. J., 1996, APJS, 103, 427

[30] Hales S. E. G., Baldwin J. E., Warner P. J., 1988, MNRAS, 234, 919-936

[31] Hao J. et al., 2010, APJS, 191, 254-274

[32] Hunter J. D., 2007, Computing In Science & Engineering, 9, 90-95

[33] Inductiveload, NASA, online image titled "A diagram of the electromagnetic spectrum", 26 October 2007. (accessed December 22, 2017) `https://en.wikipedia.org/wiki/Electromagnetic_spectrum#/media/File:EM_Spectrum_Properties_edit.svg`

[34] Intema H. T., Jagannathan P., Mooley K. P., Frail D. A., 2017, AAP, 598, A78

[35] Krawczyk C. M. et al., 2013, APJS, 206, 4

[36] Lane W. M. et al., 2014, MNRAS, 440, 327-338

[37] LibreTexts, Physics, online image titled "The Electromagnetic Spectrum", 17 December 2016. (accessed December 22, 2017) `https://phys.libretexts.org/TextMaps/Astronomy_and_Cosmology_TextMaps/Map%3A_Astronomy_(OpenStax)/5%3A_Radiation_and_Spectra/5.2%3A_The_Electromagnetic_Spectrum`

[38] Lin Y.-T. et al., 2010, APJ, 723, 1119-1138

[39] Maslowski J., 1972, ACTAA, 22, 227

[40] Maslowski J., Pauliny-Toth I. I. K., Witzel A., Kuehr H., 1984, AAP, 139, 85-92

[41] Massaro F. et al., 2014, APJS, 213, 3

[42] McMahon R. G., White R. L., 2002, APJS, 143, 1-23

[43] McMullin J. P. et al., 2007, Astronomical Data Analysis Software and Systems XVI, 376, 127

[44] Mhardcastle, online image titled "Radio galaxy 3C31", 5 February 2006. (accessed January 19, 2018)
`https://commons.wikimedia.org/wiki/File:Radio_galaxy_3C31Fr.png#/media/File:Radio_galaxy_3C31.png`

[45] Mhardcastle, online image titled "Radio galaxy 3C98", 5 February 2006. (accessed January 19, 2018)
`https://upload.wikimedia.org/wikipedia/commons/a/aa/Radio_galaxy_3C98.png`

[46] Mingo B. et al., 2011, APJ, 731, 21

[47] Mohan N., Rafferty D., 2015, Astrophysics Source Code Library, 1502.007

[48] Mulcahy D. D. et al., 2014, AAP, 568, A74

[49] Padovani P., 2016, AAPR, 24, 13

[50] Panadzhyan V. G., 1998, Astrophysics, 41, 246-253

[51] Pâris I. et al., 2014, AAP, 563, A54

[52] Paturel G. et al., 2003, AAP, 412, 45-55

[53] Pooley G. G., Kenderdine S., 1968, MNRAS, 139, 529

[54] Prochaska J. X., Hennawi J. F., Herbert-Fort S., 2008, APJ, 675, 1002-1013

[55] Quillen A. C., Bland-Hawthorn J., Brookes M. H., et al., 2006, APJL, 641, L29

[56] Ransom S., online page titled "Brightness and Flux Density", 06 December 2010. (accessed January 25, 2018)
`http://www.cv.nrao.edu/course/astr534/Brightness.html`

[57] Ransom S., online page titled "Radiation Fundamentals", 23 September 2016. (accessed December 22, 2017)
`http://www.cv.nrao.edu/~sransom/web/Ch2.html`

[58] Ransom S., online page titled "FreeFree Radiation", 23 September 2016. (accessed December 22, 2017)
`http://www.cv.nrao.edu/~sransom/web/Ch4.html`

[59] Ransom S., online page titled "Synchrotron Radiation", 25 October 2016. (accessed December 22, 2017)
`http://www.cv.nrao.edu/~sransom/web/Ch5.html`

[60] Ransom S., online page titled "Spectral Lines", 29 November 2016. (accessed December 22, 2017)
`https://www.cv.nrao.edu/~sransom/web/Ch7.html`

[61] Sault R. J., Teuben P. J., Wright M. C. H., 1995, Astronomical Data Analysis Software and Systems IV, 77, 433

[62] Schneider D. P. et al., 2007, AJ, 134, 102-117

[63] Schneider D. P. et al., 2010, AJ, 139, 2360

[64] Seyffert E. N. et al., 2013, APJ, 779, 161

[65] Shafi N. et al., 2015, MNRAS, 454, 1404

[66] Shen Y. et al., 2008, APJ, 680, 169-190

[67] Shen Y. et al., 2011, APJS, 194, 45

[68] Shimwell T. W. et al., 2017, A&A, 598, A104

[69] Shulevski A. et al., 2017, AAP, 600, A65

[70] Suchkov A. A., Hanisch R. J., Voges W., Heckman T. M., 2006, AJ, 132, 1475-1484

[71] Swinburne University of Technology, online pdf titled "Mechanisms of Radio Emission: Thermal and Non-Thermal Radio Emission", 2010. (accessed December 22, 2017)
`http://astronomy.swinburne.edu.au/sao/downloads/HET608-M03A02.pdf`

[72] Szabo T. et al., 2011, APJ, 736, 21

[73] Vallee J. P., Roger R. S., 1989, AAPS, 77, 31-38

[74] Veilleux S., Cecil G., Bland-Hawthorn J., 2005, ARAA, 43, 769

[75] Véron-Cetty M.-P., Véron P., 2006, AAP, 455, 773-777

[76] Véron-Cetty M.-P., Véron P., 2010, AAP, 518, A10

[77] Vollmer B. et al., 2010, AAP, 511, A53

[78] West A. A. et al., 2008, AJ, 135, 785-795

[79] West A. A. et al., 2011, AJ, 141, 97

[80] Zhou W., 2002, Chinese Journal of Astronomy and Astrophysics, 2, 106